ACTA MATERIALIA TRANSYLVANICA

Anyagtudományi Közlemények

2. évfolyam, 2019. 1. szám

ERDÉLYI MÚZEUM-EGYESÜLET
Kolozsvár
2019

A folyóirat megjelenését támogatta a Magyar Tudományos Akadémia, a Bethlen Gábor Alapkezelő Zrt. és az EME Műszaki Tudományok Szakosztálya / The publication of this magazine was supported by the Hungarian Academy of Sciences, by the Bethlen Gábor Fund and by the TMS – Department of Engineering Sciences

Kiadó / Publisher: Erdélyi Múzeum-Egyesület
Felelős kiadó / Responsible publisher: Biró Annamária
Olvasószerkesztő / Proofreader: Szenkovics Enikő (magyar), David Speight (English)
Szerkesztőségi titkár / Editorial secretary: Kisfaludi-Bak Zsombor
Borítóterv / Cover: Könczey Elemér
Nyomdai munkálatok / Printed at: F&F International kft., Gyergyószentmiklós

ISSN 2601-1883, ISSN-L 2601-1883
DOI: 10.2478/amt-2019-01
Online elérhető / online available at: https://eda.eme.ro/handle/10598/30356
A folyóirat honlapja: https://www.eme.ro/publication-hu/acta-mat/mat-main.htm
The journal website: https://www.eme.ro/publication/acta-mat/mat-main.htm

Az *Acta Materialia Transylvanica. Anyagtudományi Közlemények* az Erdélyi Múzeum-Egyesület (EME) Műszaki Tudományok Szakosztályának folyóirata, amely az anyagtudományok területéről közöl tudományos közleményeket: szakcikkeket, összefoglalókat (szemléket), tanulmányokat. A folyóirat célja összképet adni kiemelten a Kárpát-medencei kutatási irányokról, tudományos eredményeiről, s ezt széles körben terjeszteni is. A folyóirat az EME felvállalt céljaihoz híven a magyar szaknyelv ápolását is támogatja, így a nyomtatott folyóirat magyar nyelven jelenik meg, mely az Erdélyi digitális adattárban elérhető (https://eda.eme.ro/handle/10598/30356). A széles körű nemzetközi terjesztés érdekében a folyóirat teljes angol nyelvű változatát is közzétesszük.

Acta Materiala Transylvanica – Material Sciences Publications – is a journal of the Technical Sciences Department of the Transylvanian Museum Society, publishing scientific papers, issues, reviews and studies in the field of material sciences. Its mission is to provide and disseminate a comprehensive picture focusing on research trends and scientific results in the Carpathian basin. In accordance with the general mission of the Transylvanian Museum Society it aims to support specialized literature in Hungarian. The printed version of the journal is published in Hungarian and is available in the Transylvanian Digital Database (https://eda.eme.ro/handle/ 10598/30356). However, we would like to spread it internationally, therefore the full content of the journal will also be available in English.

Tartalom / Content

sciendo

Acta Materialia Transylvanica 2/1. (2019) 1–6.
https://doi.org/10.33924/amt-2019-01-01
Hungarian: https://doi.org/10.33923/amt-2019-01-01
https://eda.eme.ro/handle/10598/31419

ACTA MATERIALIA TRANSYLVANICA

The Relationship between Materials Science and the Fourth Industrial Revolution

Zoltán KOLOZSVÁRY

SC Plasmaterm SA; Sapientia "Sapientia" Hungarian University of Transylvania, Târgu-Mureș, Romania.
zoltan.kolozsvary@plasmaterm.ro

Abstract

There has been a spectacular and extremely fast development in all areas of materials science. This development is driven by science and technology, yet a time gap may be observed between the progress of technology that drives the fourth industrial revolu-tion, and its acceptance in society. Our task is to learn how a balance may be achieved between rapid technological development and societal acceptance.

Keywords*: materials science, fourth industrial revolution, technology, society, time gap, additive manufacturing, surface treatment, conflict risk materials.*

1. Introduction

Throughout the history of mankind, there has been a characteristically strong interdependence between the development of technology, and the development of society. The time gap between these two depends on communication and primarily on its speed.

The easier and faster the communication, the faster and stronger is the social reaction to it. After centuries of „accumulation", the 20 century has accelerated this spiral, generating even more impetus in the first decades of the 21st. century.

The last two decades of the twentieth century and the first two of the twenty first have remodelled the concept of science and technology. A pronounced time gap has appeared between changes in industry and their social interpretation.

The beginning of the 21st century „attacked" human society with unprecedented speed. The potential of data processing and data transmission increased spectacularly and- as a consequence- the borders in almost every area of daily life expanded significantly, even if not always to the benefit of the society.

Today it seems to be a common place saying that „the twentieth century was the century of physics", and this cannot be denied; its effects are sensed (or sometimes suffered) even today. No doubt, this is a very sophisticated question as the interdependence between technology and society has always been critical, and determining this interdependence has become even more relevant with the increasing data processing and data transmission as **Figure 1.** demonstrates.

„... the part and the whole..." as Werner Heisenberg formulated was never more actual than it is today!

The unprecedented rate of development of science and technology is digging deeper and deeper into materials and brings to the surface their ever-smaller details.

... however all these are only „details" which may bring a significant development for human being and society, if we do not forget the „whole". The goal of this paper is to outline a short, synthetic summary on „the whole" ... approaching it from the point of view of materials science.

2. The social responsibility of material scientists regarding material use

The **Figure 1.** schematically outlines the interdependencies of science and technology and the society, emphasizing the today dominant triangle which – in fact – is propelled by materials science.

If we try to briefly outline the main directions, these should be summarized as:

– Ever increasing expectations on performance, with a simultaneous reduction of the production costs and energy needs, whilst not neglecting the reduced environmental hazard.

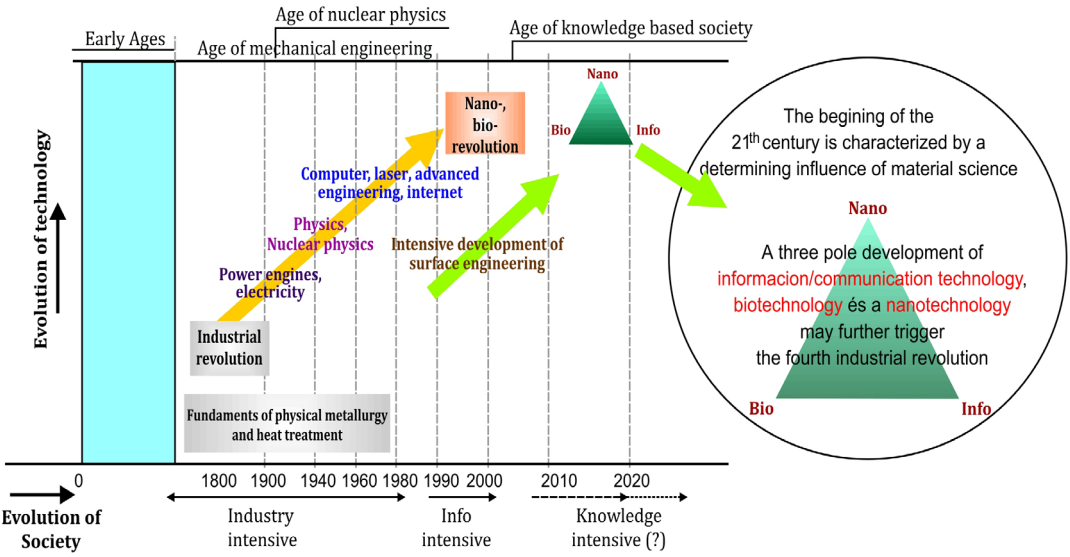

Figure 1. *Interdependence between science, technology and society*

– The spectacular development of investigating methods and instrumentation has opened new possibilities to learn, experiment and develop new materials, often with almost surprising properties. (Just one example: new gold-platinum alloy with unprecedented wear resistance and a hardness comparable with that of the diamond) [1].

Though new materials appear almost at a daily rate, development is also very significant in the field of those materials considered „classic".

The specific material consumption is decreasing in almost any industrial field but the global material need is spectacularly increasing. The world is slowly beginning to suffer a material crisis. Technical materials are becoming more and more diverse, there are always new expectations as functions of new technologies, a good example for this is 3D printing **[2]**. On approaching the topic of critical materials it's enough to look at the Periodic Table of Elements

A critically important field of the global economy is energy production, and even more, energy storage. The efficiency of the systems and mechanisms largely depends on the properties of the used materials. Solar panels, wind turbines and hydrogen fuel cells all generate extreme expectations from materials. Although it can seem like the „usual" materials that have been subjected to special surface improving treatments still form the majority, there are more and more fields where less conventional materials, alloys or even non-metals are used. Going back to the field of our research let's consider a few principles that are important for those involved in scientific research, development and innovation, regarding the economic use of materials.

– The rational use of materials has to start from the design.
– The total life-cycle of materials has to increase, and recycling has to be considered, whenever possible.
– Technologies with minimum waste have to be developed.
– In order to increase the useful lifecycle of products, efficient heat treating and surface engineering technologies have to be developed.
– For reducing the waste resulting from design or technology, computer modelling and simulation have to be applied on a large scale.
– It is also important to consider the problem of critical materials, the "conflict mineral risk" It is enough to claim just a few of these: cobalt, titanium, gold, platinum, tantalum, tungsten, vanadium, neodymium, lithium, rare earth metals etc. **[3]**. In the case of critical materials or endangered materials alternative solutions have to be developed by advanced research and development procedures.

3. A few important considerations on optimal use of materials

The principles of material use that consider the future too are increasingly present in the work-

ings of society, but there are more and more urgent signs of a need for a long term responsible thinking. That's why I think it's important to evidentiate some important principles regarding material use:

- On a short run the need for developing new materials will not effectively influence the interest for the materials in general use on a large scale.
- Iron alloys will, in future, also be the most important engineering materials, however their properties will undergo significant modifications.
- Aluminum and titanium alloys will increasingly become the focus of attention, especially for transport vehicles.
- There is an ever-increasing interest in composites but significant changes are to be expected concerning their properties.
- The increasing application of graphite in its different forms (graphen, aerografite, fulleren a.s.o) seems very interesting... It seems a rational question should be: after the Iron Age, is the „carbon age" coming ...?
- In order to reduce energy needs -primarily for transport vehicles- there is an increasing interest in developing light weight structures without reducing their efficiency. This should be a result first of all of a rational development but the use of lightweight materials becomes more and more the focus of attention. In this respect aluminum is the focus of attention, - even if the energy need for its metallurgy is considerable and difficulties appear also in recycling, which means the "total lifecycle" is more limited compared to the steel [4].
- The increasing interest in light alloys in the vehicle industry is also orienting interest towards new plastic deformation- and surface engineering technologies (this certainly is true also for titanium alloys).

Following this line of "philosophy" a brief look at Figure 2. should be of interest. It illustrates the changes in uses of materials for the carrosseries of transport vehicles. The interest in composites and light alloys versus that of steel seems evident.

The increasing interest in 3D printing in the most diverse application areas is also evident, including aerospace and medical instrumentation.

In additive manufacturing, the structure of materials may be well projected supporting specific properties which has a particular importance [5, 6].

4. Fields of key importance in industry

When additive manufacturing is considered, two industrial areas are of particular importance: the vehicle industry and energy generation/storage. In this respect development is really spectacular, with a special emphasis on metal additive manufacturing.

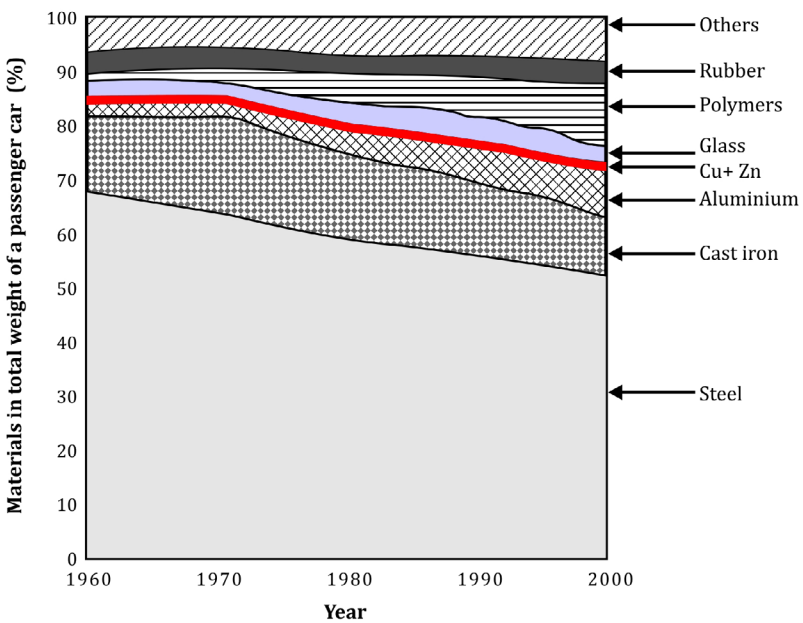

Figure 2. *Changes in material use in the automotive industry*

For the moment the problems connected to metallurgy of material structure, like surface modification technologies, are very little known. Significant differences appear in the metallurgy function of applied procedures. Fast solidification, oriented cooling and changes in the structure due to repeated heating and cooling, all strongly influence the microstructure of the material. All these processes are very little known at present, as these are radically different from those associated with conventional processes [7].

The procedures for modifications in the structure of bulk material and those of the surface are very poorly known and form a totally new area which -until now- has been very little studied and investigated (that is to say that surface treatments i.e. **Figure 3.**) form a fundamentqally new domain, little known or studied presently. [8].

It would be a mistake not to consider the preoccupation concerning the study of materials produced by nature, and we have to learn from the „mother nature"... According to T. S. Sudarshan: nature is „a warehouse of futuristic materials where the impossible becomes possible" [9].

– Nature offers simple solutions with degradable materials and using available resources (Water, air, minerals, organics-proteins, sunlight).
– Uses only the energy needed and disposes of the rest making it a model of sustainability.
– No pollution – filled with optimization!

A strong increase of interest in bio-inspired and nano technology-based surface modification may also be observed [10]. New surface treatment technologies appear constantly (**Figure 4.**) to which I give only two examples:

– In order to reduce the friction of contact surfaces their structure is modified, imitating the shark-skin structure.
– Developing different nano-surface structures (imitating the lotus leaf effect).

These are just a few examples but the possible applications are almost endless!

Concerning new developments we should never forget the danger of „collateral damage".

In case of materials science little attention is paid to the total lifecycle of materials, including recycling and annihilation.... In the 20th century the ever increasing application of polymers was characteristic and this trend is even more powerful at the beginning of this century. However, no attention has been given to the problem of „afterlife" of the materials.

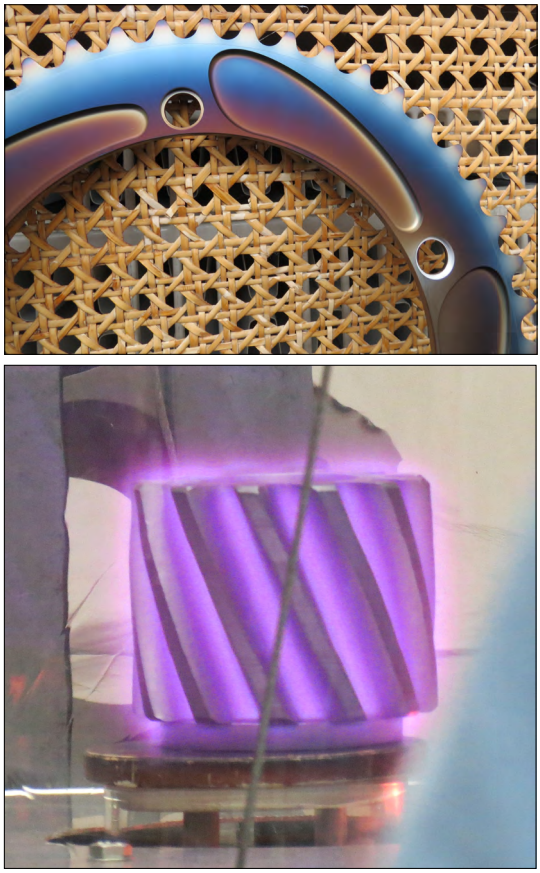

Figure 3. *Aluminium alloy gear with highly abrasion-resistant PVD coating for racing bicycles (top) and steel gear in the plasma nitriding process (bottom)*

5. Industrial development in the present and the societal challenges for material science

It is well known that the natural decomposition of synthetic materials is a slow process taking centuries, but – unfortunately – the tremendous damage they may cause in the natural environment and the deleterious consequences also on the food chain has only recently become obvious.

The increasing population of the Earth – that needs feeding – , the difficulties of providing drinking water show us that there's hardly any time left for us to continue our waste of materials.

It is increasingly evident that human society has arrived at a point where it is not satisfactory to talk about sustainable development only in terms of political slogans, but efficient actions have to be initiated. A self-evident question has to be put: what is the real driving force of industrial and so-

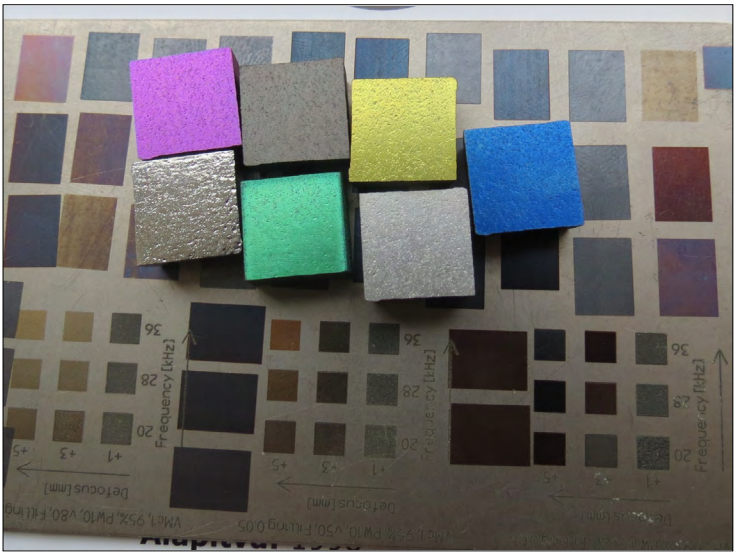

Figure 4. *Titanium implant material colored by anodizing on a titanium alloy plate colored by laser engraving*

cial development (?)... we like to say: the driving force of development is the concern for energy and environment.... but in fact, we do very little to prevent damage to the environment and to prevent the unlimited waste of materials....as a consequence it is self-evident what the real driver of industrial and economic development is: instant and limitless profit!

Materials science is one of the fundamental factors provoking the fourth industrial revolution. It has a complex and very pronounced influence on the society and on its future development, but development and environment are not separable challenges.

Considering development, we should never forget that there is a system of extremely complex and sophisticated interactions covering economic, technological, ecologic and societal aspects.

Materials science has to find scientific-technological solutions for preventing damage to the environment and to restore its healthy status. **[11]**. Materials science has to find scientific-technological solutions for preventing damage to the environment and to restore its healthy status.

We should no longer say: "this is not the task of materials science" ... and that what happens to the materials in their "afterlife" is not our concern!

It is important how we see the problem of energy and environment... each coin has two sides... The problem of energy is the focus of attention in:

– Global economy
– Research and development
– Industry

The environment is the concern of

– People in general
– Responsible (?) politicians
– Mass media

... but at the end of the day that is just the same coin!....**[12]**.

In this article I intended to present those most important realizations that I came to while working in the field of materials science and technology, regarding the parallel development of industry and society. As a final conclusion and in full agreement with it I quote a thought by professor Jianguo Liu from Michigan State University:

"....it is time to integrate all disciplines for fundamental discoveries and synergetic solutions because of increasingly connected world challenges.

Disciplinary approaches to crises like air pollution, biodiversity loss, climate change, food insecurity and energy and water shortages are not only ineffective but also making many of these crises worse because of counterproductive interactions and unintended consequences" **[13]**

References

[1] Curry J. F., Babuska T. F., Furnish T. A., Ping Lu, Adams D. P., Kustas A. B., Nation B. L., Dugger M. T., Chandross M., Clark B. G., Boyce B. L., Schuh C. A., Argibay N.: *Achieving ultralow wear with stable nanocrystalline metals*. Advanced Materials, 30/32. (2018) 1802026, 1–7. https://doi.org/10.1002/adma.201802026

[2] Ashby M.: *University of Cambridge and Granta Design*, Cambridge, 2014.

[3] *Dodd-Frank Wall Street Reform and Consumer Protection Act*. Public Law 111-203, July 21, 2010, 1375–2223. https://www.congress.gov/111/plaws/publ203/PLAW-111publ203.pdf

[4] Tisza M., Czinege I.: *Comparative study of the application of steels and aluminium in lightweight production of automotive parts*. International Journal of Lightweight Materials and Manufacture, 1/4. (2018) 229–238. https://doi.org/10.1016/j.ijlmm.2018.09.001

[5] Frazier W. E.: *Metal additive manufacturing: A review*. Journal of Materials Engineering and Performance, 23/6. (2014) 1917–1928. https://doi.org/10.1007/s11665-014-0958-z

[6] *Sandvik invests in metal powder plant*. Heat processing, 2. (2018) 14.

[7] Kolozsvary Z.: *Surface engineering: its limits for engineering applications*. IFHTSE 19th International Congress, Glasgow, 2011.

[8] Kolozsvary Z.: *Surface engineering: a bridge between 'avant-garde' and conventional materials and technologies*. 20. Congress of IFHTSE, Beijing, 2012.

[9] Sudarshan T. S.: *Emulate to innovate*. SMT 31 – The 31st Edition of the International Conference on Surface Modification Technologies, July 5–7, 2017, Mons, Belgium.

[10] Fan Xia, Lei Jiang: *Bio-inspired, smart, multiscale interfacial materials*. Advanced Materials, 20/15. (2008) 2842–2858. https://doi.org/10.1002/adma.200800836

[11] *Techniques could create better material, design in high consequence uses*. ScienceDaily, September 24, 2015. www.sciencedaily.com/releases/2015/09/150924084023.htm

[12] Cantonwine P. E.: *Educating materials engineers*. Advanced Materials and Processes, March 2006, 51–53.

[13] *World's challenges demand science changes*. ScienceDaily, February 26, 2015. https://www.sciencedaily.com/releases/2015/02/150226144903.htm

Acta Materialia Transylvanica 2/1. (2019) 7–12.
https://doi.org/10.33924/amt-2019-01-02
Hungarian: https://doi.org/10.33923/amt-2019-01-02
https://eda.eme.ro/handle/10598/31422

Research on Technical Ceramics and their Industrial Application: Preparation Techniques and Properties of Transparent AlON Ceramics

Csaba BALÁZSI, Mónika FURKÓ, Fruzsina SZIRA, Katalin BALÁZSI

Thin Film Physics Department, Institute forTechnical Physics and Materials Science, Research Centre for Natural Sciences, Hungarian Academy of Sciences, Budapest, Hungary, balazsi.csaba@energia.mta.hu

Abstract
Aluminium oxynitride (AlON) has a unique thermal and chemical stability that makes it the perfect candidate for a wide range of applications. This article provides a brief description and comparison of the most common AlON preparation methods along with their advantages and disadvantages. Although there has been extensive research on the material, especially more recently because of increased commercial interest, extensive systematic powder synthesis and processing studies have not been carried out to determine alternate, more cost efficient routes to fully dense transparent bodies. Further optimization of reaction sintering and transient liquid phase sintering could be important processing routes.

Keywords*: AlON, transparent ceramics, Hot Isostatic Pressing (HIP), Spark Plasma Sintering (SPS).*

1. Introduction

The discovery of aluminium oxynitride goes back to the 1970s, when researchers in Japan, the United States and France found that additions of nitrogen into aluminium oxide resulted in new spinel-like phases. This translucent aluminium oxynitride spinel ceramic was named AlON, a unique material exhibiting many important properties which make it useful in many applications and others yet to be determined. Currently commercially available AlON materials exhibit average grain sizes in the order of 150–200 μm; however, development of new methods to control the grain size, especially at the nano-scale could create materials with improved properties. Because of its high hardness, there are still significant cost issues associated with final machining and polishing, especially for large bodies [1].

The individual properties of the AlON material lie in its unique crystal structure. Generally, it can be said that substitution of nitrogen for oxygen in Al_2O_3 or, conversely, substitution of oxygen into AlN stabilizes new phases with significantly different crystal structures and symmetry (space group): α-Al_2O_3, AlON and AlN rhombohedral, cubic, and hexagonal, respectively. AlON, having the cubic spinel structure, can be thought of as nitrogen stabilized cubic aluminium oxide. It has many properties comparable to α-Al_2O_3, but because of its cubic crystal structure, fully dense, polycrystalline bodies can be completely transparent if processed properly [2]. Other properties, like dielectric loss tangent, can be extremely low because of the lack of thermal expansion-induced residual strain at grain boundaries. AlN is an intriguing material because its theoretical thermal conductivity at room temperature is extremely high for a dielectric material and comparable to, or higher than many metals [3].

2. Overview of preparation techniques

Over the years several different processing routes have been used to produce fully dense, transparent polycrystalline AlON ceramics [2–14]. Their main parameters are summarized in **Table 1.** McCauley [2] used reaction sintering of Al_2O_3–AlN mixtures. The reaction sintering technique has also been used by others [15,16].]. Generally, the pressureless sintering, hot pressing and hot isostatic pressing (HIP) techniques have used AlON

Table 1. *Summary and characteristics of AlON techniques*

Method		Advantages	Disadvantages	Ref.
Pressureless sintering	Sintering that is performed using only temperature.	– Production procedure is simple – Cost effective	– Higher temperature is needed than in hot pressing techniques	[4]
Hot pressing (HP)	Combination of uniaxial pressure and temperature.	– Production procedure is simple – Sintering density is high, – The quality of end products is good with high density	– Expensive (high pressure, high temperature) – Only simple shapes can be created	[5]
Hot isostatic pressing (HIP)	Simultaneous application of heat and hydrostatic pressure to compact and densify a powder.	– High density can be achieved – Densification can be com-pleted in shorter times and at lower temperatures than conventional sintering – Products with complex geometry can be produced – The quality of end prod-ucts is good	– Expensive (high pressure and high temperature, ex-pendable tools) – The processes are complex – Small production quantities	[6, 7]
Spark plasma sintering (SPS)	The process applies pressure and (pulsed) current flow through the sample at the same time in vacuum	– Fast heating, – Effective for densification of a wide variety of mate-rials – Densification occurs at lower temperature and is completed more rapidly than in other methods	– Complicated setup and limited sample shape – Hard to operate, – Expensive pulsed DC generator is required	[8–10]
Carbothermal synthesis (CT)	The technology uses graphite furnace at different temperatures (1700-1860 °C) and pressures (0.1-10 MPa) in N_2 atmosphere	– Simple – Cost effective – Possible to obtain very fine powder with a low metal impurity	– Higher tempera-tures and longer reaction times needed – Thermal decomposition process is too complex – Carbon impurities	[13]
Direct nitriding	Thermochemical surface treatment process, Al–Al_2O_3 starting mixtures	– Simple – Cost effective	– Lower transparen-cy – Lower quality of product	[14]

powders to produce pore free, fully dense AlON ceramics. AlON powders can be synthesized by simple reaction of Al_2O_3 and AlN, carbothermal reduction of Al_2O_3. Significant variations in hardness, flexure strength and fracture toughness were observed. The friction, wear resistance and other mechanical properties of the Al_2O_3–AlON family of materials has also been systematically studied [17, 18]. High sintering temperature and long sintering time are two major problems in the above methods. Therefore, it is critical to lower the sintering temperature and reduce the sintering time without reducing material performance.

3. State of the art in development of AlON

The most commonly used and promising techniques in industry are the HP, HIP and SPS. Shan et al. [9] used spark plasma sintering (SPS) in their research work with Al_2O_3 and AlN powder mixtures to produce AlON ceramics. The SPS was performed at temperatures between 1400 and 1650 °C for 15–45 min. at 40 MPa under N_2 gas flow. They found that AlON phase formation was initiated in the samples sintered above 1430 °C. The complete transformation of the initial phases (Al_2O_3 and AlN) into AlON was observed in the

samples that were spark plasma sintered at 1650 °C for 30 min at 40MPa. A high spark plasma sintering temperature together with a low heating rate yielded a greater amount of AlON formation at a constant process time.

Increasing the spark plasma sintering temperature from 1430 to 1650 °C significantly increased the degree of AlON phase formation. Although most of the studies on AlON formation by reaction sintering of Al_2O_3 and AlN powders have indicated that sintering temperatures above 1650 °C and a sintering duration longer than 2 h require volume diffusion to obtain pure, dense AlON ceramics, spark plasma sintering produced pure AlON ceramics above 98.5 % of the theoretical density by sintering at 1650 °C for 30 min with a 50 °C/min. heating rate [9]. The AlON ceramics can also be prepared by SPS at low temperature (<1650 °C) and short sintering time (5–15 min.), however, the hardness and the relative density became a little higher and a little grain growth was found with increasing soaking time. Although relative density increased and pores gradually disappeared, the grain size of AlON also grew with the holding time. Larger grains led to a decrease in the flexural strength and elasticity modulus. Fully dense AlON ceramics cannot be fabricated by SPS without sintering additives whether under nitrogen or vacuum. Moreover, AlON ceramics possessed better properties fabricated under vacuum than under N_2 atmosphere [10, 11]. By using different additives, the residual porosity of transparent AlON can be reduced to a minimum. Although sintering additives can reduce the sintering temperature and increase the density of AlON ceramics, it is important to avoid generating a second phase that would reduce the transparency of AlON ceramics [12].

Chen et al. [7]] prepared highly transparent AlON composite ceramics by hot isostatic pressing (HIP) of the sintered bodies composed of fine grains (~20 μm). They also found that sintering additives play a huge role in the porosity and pore positions of the sintered AlON bodies, which can determine the final pore elimination during HIP sintering. They claimed that compared to single Y_2O_3 or La_2O_3 additive, the co-doping of Y_2O_3/La_2O_3 additive is more effective in preparing a sintered AlON body with small intergranular pores and lower porosity. The developed transparent AlON ceramic had an in-line transmittance as high as 85.0 % at 1100 nm with low concentration of additives. The transmittance was sensitive to the microstructure of presintered AlON bodies. Except for the strong driving force enabled by HIP method, the small amount of Y_2O_3/La_2O_3 additives was effective in fabricating pre-sintered AlON bodies with small intergranular pores and lower porosity. Such AlON bodies were then easy to densify during HIP sintering and were significant to give high transparency. The necessary additives for the HIP-ed AlON ceramics (4.2 mm thick) to achieve full density were 0.08 % Y_2O_3 and 0.02 % La_2O_3, much lower than previously reported data in pressureless sintered samples (0.12 % Y_2O_3 and 0.09 % La_2O_3).

The densities and transparency characteristics of AlON prepared by different techniques are compared in Figure 1. It can be seen that the relative densities of AlON prepared by different methods are all close to 100 %, which demonstrates their effectiveness in obtaining pure and dense ceramics. According to the thorough literature survey, the transparency of AlON ceramics produced by different methods shows significant differences. The lowest transparency was measured in the case of the CT method (65 %), while in the other methods the transparency values of all samples were above 75 %. The highest transparency was measured in the case of SPS technology (79.2±2.4 %).

Nowadays, there are several companies that produce AlON ceramics for different use.

The pathway of incident and reflected light is illustrated schematically in Figure 2.

AThe interference between the incident light and the polycrystalline ceramics can be understood by further examination of the mechanism

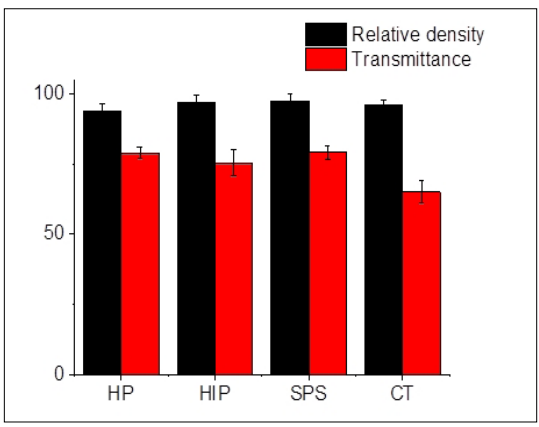

Figure 1. *Relative densities and transmittance percentages (in visible wavelenght range) of AlON samples prepared by different techniques. The relative density was calculated using a theoretical density of 3,71 g/cm³*

of refraction and reflection of light. In general, distortion often occurs close to the surface of a ceramic and at grain boundaries. Local distortion and strained layers resulting from surface processing give rise to localized changes of refractive index, causing light to be scattered and affecting the optical transmittance (**Figure 3**).

In **Figure 4** és **5** we demonstrate the applied characteristic temperature ranges of investigated preparation techniques as well as the hardness values of the yielded transparent ceramics. It can be seen that the hardest AlON ceramic can be achieved by SPS method at the lowest preparation temperature. AlON can serve as a model material for polycrystalline ceramics and, because of its transparency, real time diagnostic observations can be easily carried out in many mechanical tests. Other possible applications of AlON materials include transparent armour, EM domes and windows, military aircraft and missile domes, IR windows, hyper-hemispherical domes, laser windows, military aircraft lenses, semiconductor processing applications, and scanner windows (point of sale (POS) windows).

Figure 6 shows the flexural strength of different AlON samples. It is visible that the highest strength belongs to the AlON ceramic prepared by SPS method, while the differences in the values of flexural strength in the cases of ceramics prepared by HP and HIP methods are insignificant. The sample prepared by CT method has the lowest strength.

The other important mechanical property for possible industrial application is fracture toughness. The changes of this parameter in samples prepared with different methods are presented in **Figure 7.**

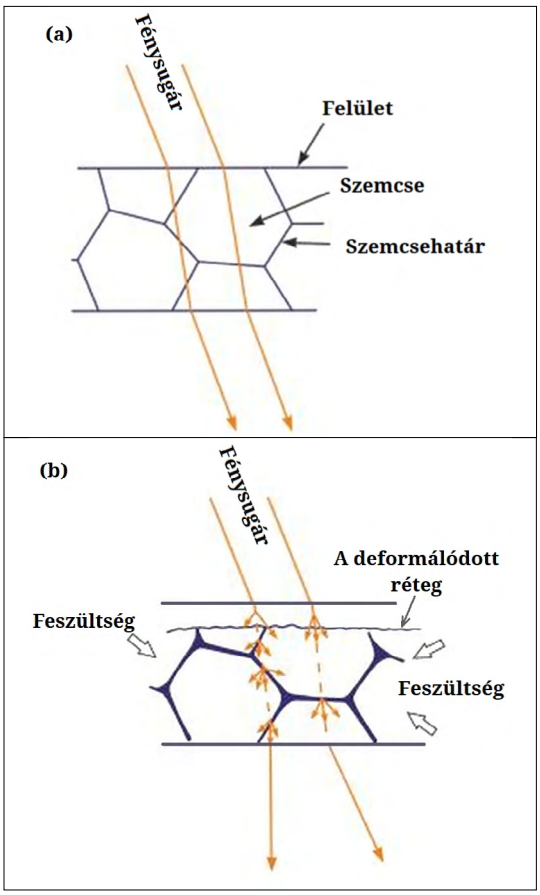

Figure 3. *Interaction scheme between the light and the isotropic polycrystalline ceramics. (a) Ideal homogenous polycrystal with theoretical density. Light is not scattered about grain boundaries. (b) Polycrystal with internal strain and external stress. Light is scattered in the inhomogenous region*

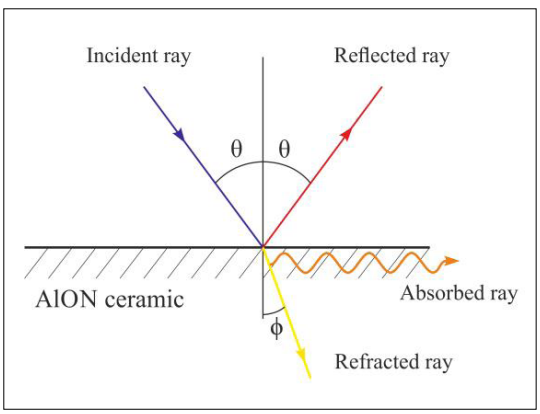

Figure 2. *Schematic illustration of the reflection and re-fraction mechanism of light*

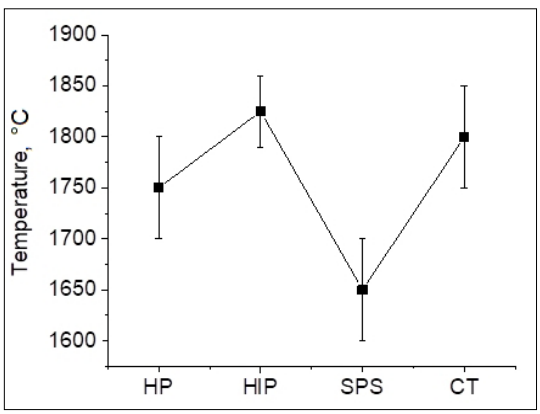

Figure 4. *The applied temperature ranges in different techniques*

In this case, similarly, the sample prepared by SPS has the highest fracture toughness, while the lowest toughness value belongs to samples prepared by CT method.

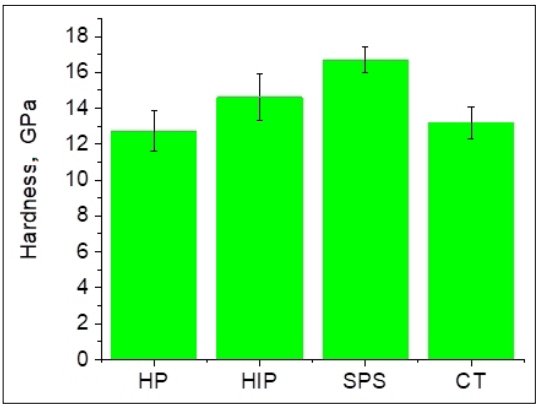

Figure 5. *The hardness values of AlON samples prepared by different techniques*

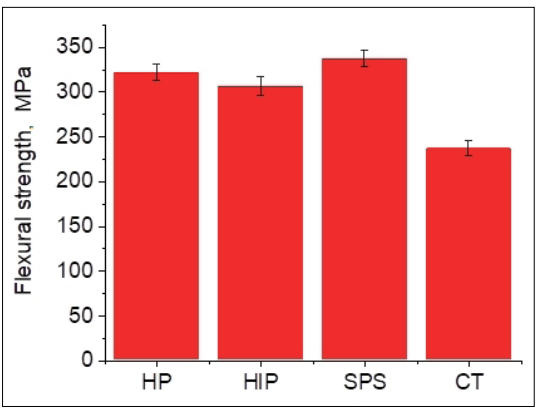

Figure 6. *Flexural strength values of AlON samples prepared by different techniques*

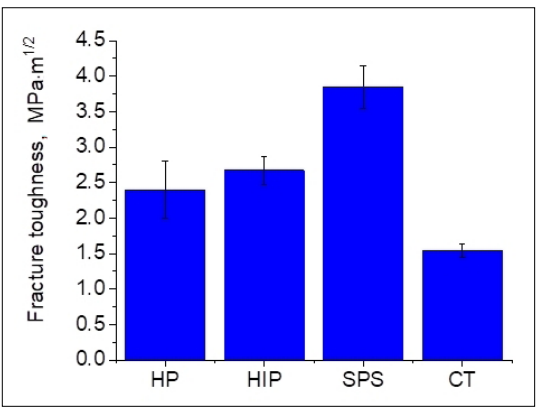

Figure 7. *Fracture toughness of AlON samples prepared by different techniques*

Zhao et al. [5] studied the effect of different additives, such as SiC and ZrN nano-particles on the mechanical properties of AlON ceramic. Their work revealed that the nano-sized additives positioned at grain boundaries of micro-sized AlON particles and the presence of SiC and ZrN nano-particles resulted in the reduction of both porosity and grain size, and a change of fracture mode from intergranular cracking in AlON to intragranular cracking in composites. With presence of small amount (5-8 %) of additive particles, the relative density, microhardness, flexural strength and fracture toughness increased owing to the hindered crack propagation processes. Li et al. [11] prepared transparent AlON ceramic by SPS method. Their results showed that fully dense AlON ceramics cannot be fabricated by SPS without sintering additives whether under nitrogen or vacuum. There was even a contradiction between transparency and mechanical properties of AlON ceramics with increased holding time, heating rate and sintering temperature. Although sintering additives can reduce spark plasma sintering temperature and increase the density of AlON ceramics, generation of a second phase that would reduce the transparency of AlON ceramics should be avoided.

4. Conclusions

According to the thoroughly studied literature data and the state of the art on AlON preparation we can conclude that the currently available and used techniques are still all expensive, as well as being energy and time consuming. High temperatures above 1600–1900 °C are needed for a long time to achieve appropriate phase and densification. We intend to develop an eco-friendly preparation method of AlON in which we develop a novel way to reduce the temperature and/or time thus requiring lower energy (technique, temperature and so on). Moreover, we are planning to recycle and utilize the industrial by-products or aluminium waste (such as aluminium cans) as Al source.

Acknowledgement

The authors acknowledge the support from „Eco-friendly AlON Processing” NNE129976 NKFIH project.

References

[1] McCauley J. W., Patel P., Chen M., Gilde G., Strassburger E., Paliwal B., Ramesh K. T., Dandekar D. P.: *AlON: A brief history of its emergence and evolution.* Journal of the European Ceramic Society,

29/2. (2009) 223–236.
https://doi.org/10.1016/j.jeurceramsoc.2008.03.046

[2] McCauley J. W., Corbin N. D.: *Phase Relations and Reaction Sintering of Transparent Cubic AIurninum Oxynitride Spine1 (AION)*. Journal of the American Ceramic Society, 62/9-10. (1979) 476–479.
https://doi.org/10.1111/j.1151-2916.1979.tb19109.x

[3] McCauley J. W.: *Structure and Properties of Aluminum Nitride and AlON Ceramics*. Army Research Laboratory Aberdeen Proving Ground, (2002) MD 210053069.
https://doi.org/10.1016/B0-08-043152-6/00028-0

[4] Shan Y., Zhang Z., Sun X., Xu J., Qin Q., Li J.: *Fast densification mechanism of bimodal powder during pressureless sintering of transparent AlON ceramics*. Journal of the European Ceramic Society, 36/3. (2016) 671–678.
https://doi.org/10.1016/j.jeurceramsoc.2015.10.026

[5] Zhang N., Liang B., Wang X. Y., Kan H. M., Zhua K. W., Zhao X. J.: *The pressureless sintering and mechanical properties of AlON ceramic*. Materials Science and Engineering A, 528/19-20. (2011) 6259–6262.
https://doi.org/10.1016/j.msea.2011.04.072

[6] Jiang N., Liu Q., Xie T., Ma P., Kou H., Pan Y., Li J.: *Fabrication of highly transparent AlON ceramics by hot isostatic pressing post-treatment*. Journal of the European Ceramic Society, 37/13. (2017) 4213–4216.
https://doi.org/10.1016/j.jeurceramsoc.2017.04.028

[7] Chen F., Zhang F., Wang J., Zhang H., Tian R., Zhang Z., Wang S.: *Hot isostatic pressing of transparent AlON ceramics with Y_2O_3/La_2O_3 additives*. Journal of Alloys and Compounds, 650. (2015) 753–757.
https://doi.org/10.1016/j.jallcom.2015.08.028

[8] Xue J. M., Liu Q., Xiu T., Ma L., Fang M., Gui L.: *Hot-Pressed Translucent Aluminum Oxynitride (AlON) Ceramics*. Key Engineering Materials, 368-372. (2008) 450–452.
https://doi.org/10.4028/www.scientific.net/KEM.368-372.450

[9] Shan Y, Zhang Z., Sun X., Xu J., Qin Q., Li J.: *Further experimental investigation on fast densification mechanism of bimodal powder during pressureless sintering of transparent AlON ceramics*. Ceramics International, 43/11. (2017) 8195–8201.
https://doi.org/10.1016/j.ceramint.2017.03.146

[10] Sahin F. C., Kanbur H. E., Apak B.: *Preparation of AlON ceramics via reactive spark plasma sintering*. Journal of the European Ceramic Society, 32/4. (2012) 925–929.
https://doi.org/10.1016/j.jeurceramsoc.2011.10.043

[11] Li X., Huang J., Luo J.: *Progress and Challenges in the Synthesis of AlON Ceramics by Spark Plasma Sintering*. Transactions of the Indian Ceramic Society, 76/1. (2017). 14–20.
https://doi.org/10.1080/0371750X.2016.1257956

[12] Zientara D., Bucko M. M., Lis J.: *Dielectric properties of aluminium nitride-γ-AlO materials*. Journal of the European Ceramic Society, 27/13-15. (2007) 4051–4054.
https://doi.org/10.1016/j.jeurceramsoc.2007.02.093

[13] Zheng J., Forslund B.: *Carbothermal Synthesis of Aluminium Oxynitride (ALON) Powder: Influence of Starting Materials and Synthesis Parameters*. Journal of the European Ceramic Society, 15/11. (1995) 1087–1100.
https://doi.org/10.1016/0955-2219(95)00078-9

[14] Su M., Zhou Y., Wang K., Yang Z., Cao Y., Hong M.: *Highly transparent AlON sintered from powder synthesized by direct nitridation*. Journal of the European Ceramic Society, 35. (2015) 1173–1178.

[15] Kim Y. W., Park B. H., Park H. C., Lee Y. B., Oh K. D., Riley F.: *Sintering, microstructure and mechanical properties of AlON–AlN particulate composites*. British Ceramics Transactions, 97/3. (1998) 97–104.

[16] Kim Y. W., Park H. C., Lee Y. B., Oh K. D., Stevens R.: *Reaction sintering and microstructural development in the system Al_2O_3–AlN*. Journal of the European Ceramic Society, 21/13. (2001) 2383–2391.
https://doi.org/10.1016/S0955-2219(01)00200-X

[17] Trabelsi R., Treheux D., Goeuriot-Launay D., Goeuriot P., Thevenot F., Orange G. et al.: *Friction, wear resistance and mechanical properties of an alumina–γ-aluminum oxynitride composite (ALUMINALON)*. In: High Tech Ceramics. (ed. P. Vincenzini) Elsevier Sci. Pub., (1987) 2683–2695.

[18] Berriche Y., Vallayer J., Trabelsi R., Treheux D.: *Severe wear mechanisms in Al_2O_3–AlON ceramic composites*. Journal of the European Ceramic Society, 20/9. (2000) 1311–1318.
https://doi.org/10.1016/S0955-2219(99)00294-0

Acta Materialia Transylvanica 2/1. (2019) 13–18.
https://doi.org/10.33924/amt-2019-01-03
Hungarian: https://doi.org/10.33923/amt-2019-01-03
https://eda.eme.ro/handle/10598/31423

Examination of Layer Thicknesses of a Model Produced by Fused Filament Extrusion

Gergely DEZSŐ,[1] Gergely DEZSŐ[2]

[1] *jr, University of Debrecen, Faculty of Engineering, Debrecen, Hungary, gergelydsd@gmail.com*

[2] *University of Nyíregyháza, Institute of Engineering and Agriculture, Department of Production Engineering, Nyíregyháza, Hungary, dezso.gergely@nye.hu*

Abstract

Nowadays additive manufacturing continues to gain more and more space in industrial technology. In particular, FDM (fused deposition modelling) machines have become easily available to the public. Quality of parts is impacted by several factors. In this study we investigate layer thicknesses of a prototype manufactured from PLA, and we pay special attention to the thickness of sequentially deposited layers.

Keywords*: additive manufacturing, material extrusion, 3D printing, fused deposition modeling.*

1. Introduction

Nowadays additive manufacturing (AM) technologies are continuously being developed and drawn in industrial manufacturing. Applications in almost all fields is possible thanks to the versatility of AM technologies. It is a challenge for AM to prove its ability to produce real, competitive and robust products [1].

Amongst extrusion processes, fused deposition method (FDM) or (fused filament fabrication (FFF) is increasingly wide spread. These methods used not only form plastics [2, 3], but successful experiments have been performed for bulk metal glasses [4] and filaments containing ceramics [5].

Ensuring size and shape accuracy is an important prerequisite of competitiveness [6]. It is possible to reach good dimensional accuracies if extrusion is performed with constant temperature and mass flow controlled according to the curvature of the pathway of the printing head [7].

Frequently studied parameters in the properties of models produced by additive manufacturing are the following: layer thickness, extrusion temperature, raster angle, speed of printing head and orientation of the model within the tray. It can be demonstrated that layer thickness significantly influences tensile strength, flexural modulus and impact energy [8, 9].

Processing parameters with layer thickness amongst them plays important role also in simulation models devised for additive manufacturing [10].

Publications point out that layer thickness affects numerous mechanical properties of models additively manufactured with PLA (polylactic acid) material [11, 12].

It is an important and interesting tendency that several AM technology have become increasingly available for the wider public. Here we feature FDM (fused deposition modelling) technology amongst those.

FDM manufacturing machines are widely available on the market. They can be purchased even by private individuals. Production parameters they set up can be not optimal and because the microstructure of additive manufactured materials is sensitive to production parameters, we cannot know too much about the structure and material properties of parts produced by them. In this study we will especially focus on the spatial arrangement and thickness of layers.

2. Preparation of the test specimen

Electron microscopic study on the broken surface of a test specimen for Charpy impact test is a simple and effective way of investigating the layer thickness of bodies made of plastic [6].

Standard test specimens were manufactured by commercial Creality Cr-10 type, FDM 3D printer (**Figure 1.**). The dimensions of the test specimen were 80×10×4 mm. On one side of test specimen in the middle, there was a notch prescribed by the standard. The notch had an angle of 45 degrees, and a fillet radius of 0.25 mm. This notch was not created subsequently by material removing classical technology, such as cutting, or cold pressing. This notch was involved in the CAD model loaded in the additive manufacturing machine and was manufactured simultaneously with the whole part of the specimen.

The main dimensions of this manufacturing machine are 615×600×490 mm, and the size of the working area is 300×300×400 mm. Nozzle diameter is 0,4 mm, although other nozzles can also be applied with diameters of 0.3 and 0.2 mm. Layer thickness can be varied from 0.05 mm to 0.4 mm with steps of 0.05 mm. Size accuracy is ±0.1 mm. Highest printing temperature is 250 °C. The tray is heatable, and can be set to horizontal manually.

This manufacturing machine can use several different plastic filaments like PLA (poly lactic acid), ABS (acrylic butyl styrene), TPU (thermoplastic PUR elastomer).

Our 3 pieces of specimen were made of PLA (dark blue) at 205 °C nozzle and 70 °C build plate temperatures, with 0.1 mm layer thickness, printing speed 30 mm/s, and 100 % infill density.

Body models of the specimen were exported to STL (standard triangulation language) format.

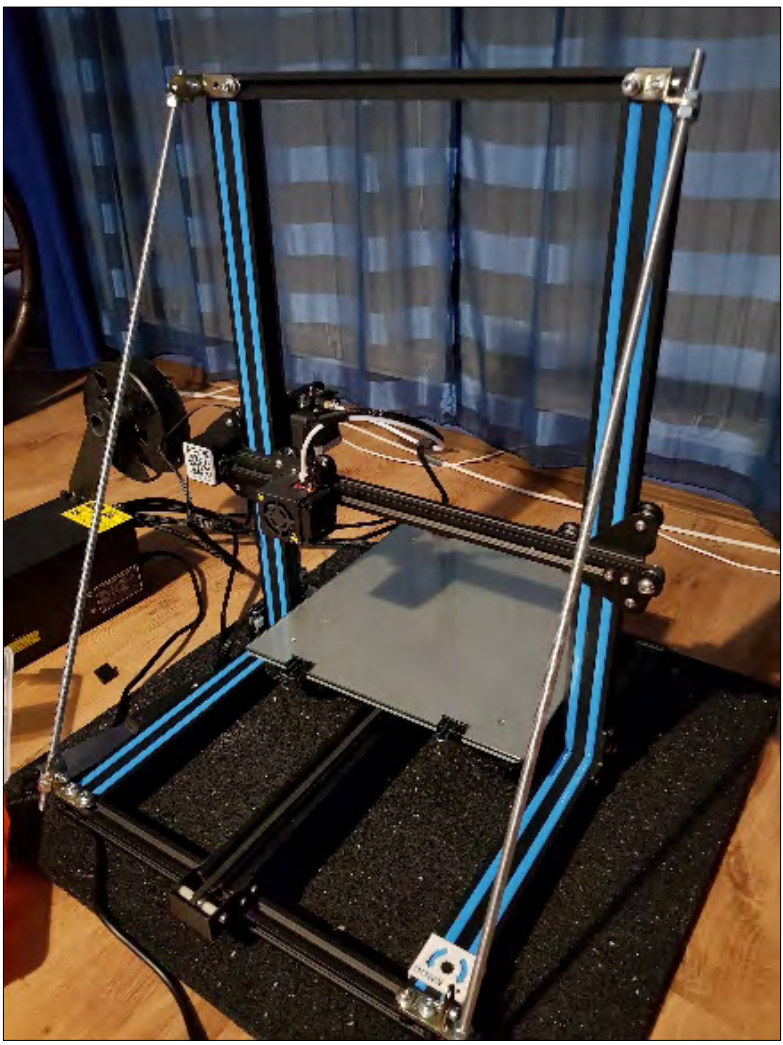

Figure 1. *Machine applied for manufacturing the specimen, Creality Cr 10*

Then those were processed by „Cura" free software, which these days is applied frequently worldwide for such purposes [3]. This software divides the body model into layers, and provides an environment for defining production and geometric parameters. Cura produces the gcode file which is applicable for control of the 3D printer.

Arrangement of strands within the specimen (raster) was 45 degrees angled. This can be observed in Figures 3. and 6.

3. Electron microscopic investigations

3.1. The electron microscope

A HITACHI SU-1050 scanning electron microscope is available at electron microscope laboratory at University of Nyíregyháza. Its maximal acceleration voltage is 15 kV, magnification ranges between 10 and 10000. The size of the tray is 150 mm.

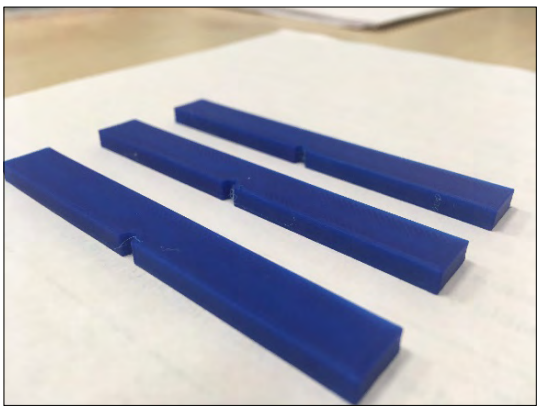

Figure 2. *The printed test specimens*

The sample is fixed with a carbonized tape, which can conduct electricity thereby eliminating static charge. Furthermore, the surface of sample is covered with a very thin layer of gold, which also serves to dissipate the charge coming from the electron beam. This is highly important for gaining a clear picture.

3.2. Sample preparation

After performing a Charpy impact test, the end part of the specimen containing the broken surface was cut. This was necessary to implement it onto the tray of the electron microscope. Its surface was coated with gold in order to avoid static electronic charging and to ensure good quality imaging. Then the sample was fixed onto the tray.

Figure 3. shows an overview of the sample fixed on the tray of the electron microscope. The lower part on the right side of the picture shows the surface of the notch, so this part is not generated by fracture, this is original as was manufactured. The left part of the figure shows the broken surface.

A magnified view of the portion of the picture included in the rectangle is shown in Figures 4. and 5. On these pictures the structure of original and broken surfaces can be easily observed. On the original surface, layers bulge and are squeezed. This is why the original surface of the model cannot be used for layer thickness measurements. On the broken surface, layers are well dissevered and are not deformed, therefore such surfaces are used for investigation of layer thickness.

Broken surface shown in Figure 6. can be divided to two parts. The surface of one is smoother, and the surface of the other is more proportioned.

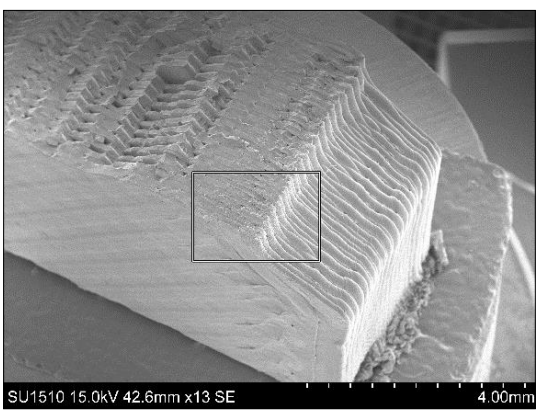

Figure 3. *An overview of the broken surface of the specimen*

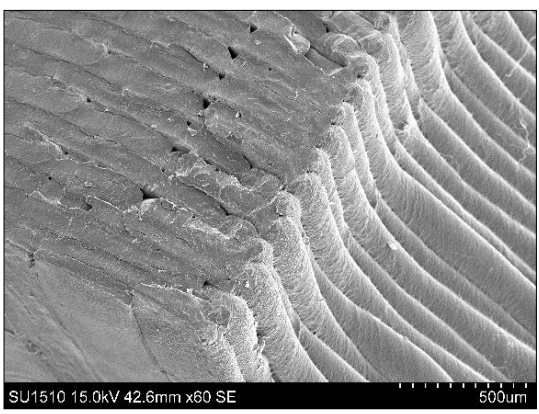

Figure 4. *Detail marked by rectangle on Figure 3. with magnification 8*

Different surfaces indicate slight differences in fracture process in the two region of the broken surface. Here we do not study this because our method is not suited to doing this. In general it can be stated that a smoother surface signifies brittle fracture and the jagged one, a ductile fracture. Delamination between printed layers cannot be observed.

The circled part in **Figure 6.** shows a crack, which is perpendicular to the direction of strands.

It can be noted that the structure of the proportioned, jagged surface resembles strain arrangement applied during the additive manufacturing process.

That part of the surface is more amenable to measurement, which is more is more proportioned, because borders of layers can be distinguished more effectively.

3.3. Investigation of layer thickness

Nominal layer thickness during the manufacturing was 0.1 mm, and the thickness of the specimen was 4 mm, so it was built up of 40 layers.

Figure 5. shows a portion of the broken surface, where 8 layers can be observed. Layers built up with different filament orientation can be well distinguished. This provides an excellent opportunity for measurement of layer thickness.

We selected such details on the broken surface in which the borders of layers could be easily observed. This is an indispensable condition of data recording by optical information. **Figure 7.** shows those parts of the broken surface that have been pointed out for this purpose.

It can be found out before measurement by survey that layers are not equal in thickness, and,

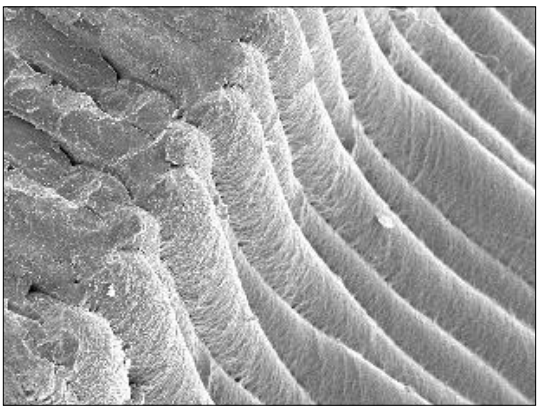

Figure 5. *Laminated structure observable on the surface of the specimen that is not suitable for measurement because of layers crinkled each order and deformed*

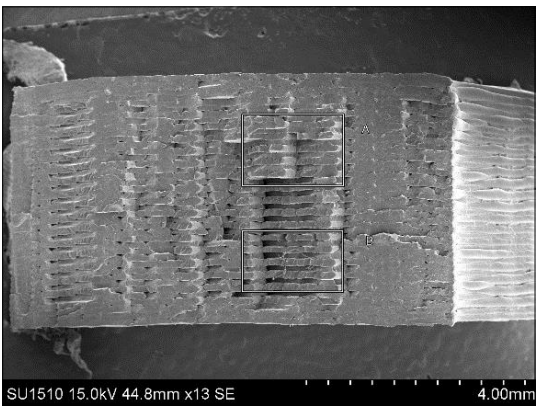

Figure 7. *Two details of the broken surface used for measurement of layer thickness (A and B)*

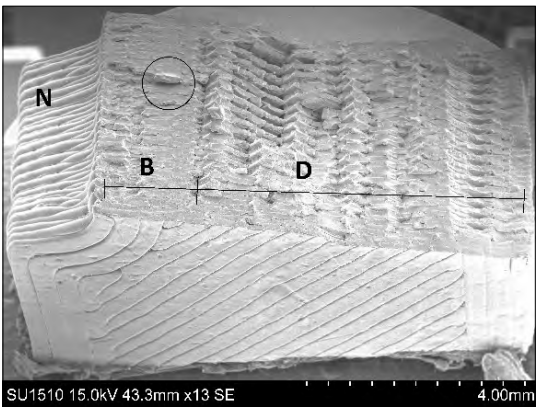

Figure 6. *Typical parts of the broken surface. N: original surface of the notch. B: area showing a bit more brittle fracture. D: area showing a bit more ductile fracture*

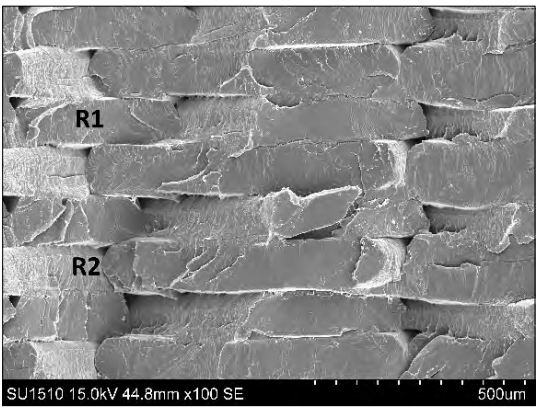

Figure 8. *A part of the broken surface that was used for layer thickness measurement (A)*

additionally, thickness can vary within a layer. That's why measurements were performed on multiple layers.

Three layers were selected in which cross sections of broken strands were visible. Five equidistant measuring points were determined for investigation. For reading of the thickness we applied the post processing software module of electron microscope, which provided distance of selected points by the operator in micrometer units.

Another detail was also selected on the broken surface where an additional two layers were studied in the way described above. This part of the surface is shown in **Figure 9.** We read thickness data. Data records are presented in **Table 1.**

It can be concluded from data presented in **Table 1.** and **2.** that the mean value of layer thickness in each case is larger than 0.1 mm, which was set as a production parameter. Standard deviation of data within a layer is high. In 4 layers of 5 investigated, more than 10 % difference can be observed between the highest and lowest data. Only for the seventh layer of the first investigated area (**Table 1.** 3rd row) can it be stated that layer thickness does not differ significantly from 0.1 mm, because of the large standard deviation.

The mean of layer thickness values is 114,4 µm, standard deviation of mean values

It can be determined by a statistical test that the mean of layer thicknesses differs from nominal value significantly. We assume that probability density function of layer thickness is a normal density function, and variance is approximated by standard deviation presented in the last column of **Table 1.** We apply a Z-test. Test statistics of Z are summarized in **Table 2.**

In the first four cases layer thicknesses significantly differ from nominal value even in the case of confidence level 0.005. In fifth row a significant difference cannot be proved.

The standard deviation of recorded data within a layer is high. Mean of means of layer thicknesses is 114.4 µm, standard deviation of means is 7.71 µm.

4. Conclusions

The broken surface of the specimen has a jagged surface. This structure comes from the special arrangement of strands in the FDM manufactured bodies, and in itself cannot be used to diagnose a brittle or ductile nature of fracture.

Table 1. *Measurement readings regarding layer thickness shown on Figure 7. in micrometer units*

	a (µm)	b (µm)	c (µm)	d (µm)	e (µm)	Average (µm)	Deviation (µm)
R1	117	113	121	124	106	116	7,05
R2	119	129	130	119	126	125	5,32
R3	128	116	128	118	122	122	5,55
R4	108	106	100	116	105	107	5,83
R5	97,2	91,3	116	120	94,2	104	13,26

Table 2. *Test statistics Z of data in Table 1*

Layer	u (value of Z-test)
R1	5.07
R2	10.51
R3	8.86
R4	2.68
R5	0.67

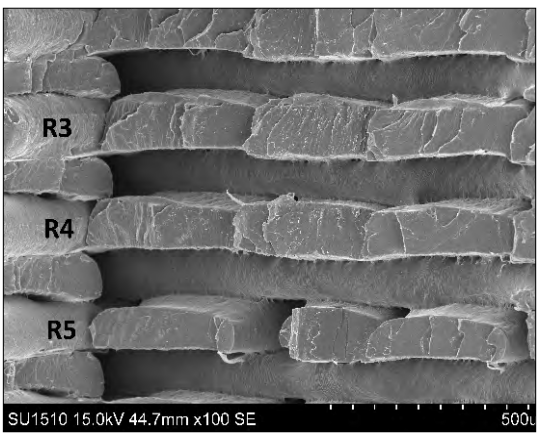

Figure 9. *Other part of the broken surface used for layer thickness measurement (B)*

On cross sections of fibres within a layer both flat and jagged fracture can be observed.

Layer thickness definitely changes from point to point, and significantly larger than 0.1 mm which was the prescribed parameter of the production.

Acknowledgement

Authors thank Miklós Fecskovics for manufacturing test specimen.

Authors thank Material Test Laboratory and Electron Microscope Laboratory of University of Nyíregyháza for their kind assistance in experimental investigations.

References

[1] Tofail S. A. M, Koumoulos E. P., Bandyopadhyay A., Bose S., O'Donoghue L., Charitidis C.: *Additive manufacturing: scientific and technological challenges, market uptake and opportunities.* Materials Today, 21/1. (2018) 22–37. https://doi.org/10.1016/j.mattod.2017.07.001

[2] Wu H., Sulkis M., Driver J., Saade-Castillo A., Thompson A., Koo J. H.: *Multi-functional ULTEM™1010 composite filaments for additive manufacturing using fused filament fabrication (FFF).* Additive Manufacturing, 24. (2018) 298–306. https://doi.org/10.1016/j.addma.2018.10.014

[3] Brenken B., Barocio E., Favaloro A., Kunc V., Pipes R. B.: *Fused filament fabrication of fiber reinforced polymers: A review*. Additive Manufacturing, 21. (2018) 1–16. https://doi.org/10.1016/j.addma.2018.01.002

[4] Nötzel D., Eickhoff R., Hanemann T.: *Fused filament fabrication of small ceramic components.* Materials, 11/8. (2018) 1463–1468. https://doi.org/10.3390/ma11081463

[5] Gibson M. A., Mykulowycz N. M., Shim J., Fontana R., Schmitt P., Roberts A., Ketkaew J., Shao L., Chen W., Bordeenithikasem P., Myerberg J. S., Fulop R., Verminski M-, D., Sachs E., M., Chiang Y-M., Schuh C. A., Hart A. J., Schroers J.: *3D printing metals like thermoplastics: fused filament fabrication of metallic glasses.* Materials Today, 21/7. (2018) 697–702. https://doi.org/10.1016/j.mattod.2018.07.001

[6] Dezső G., Százvai A., Kósa P.: *Additív gyártással készített testek alakhelyességének vizsgálata.* In: Fiatal Műszakiak Tudományos Ülésszaka XVII., Kolozsvár, Románia, 2012. március 22–23., 99–102. https://eda.eme.ro/handle/10598/15520

[7] Ertay D. S., Yuen A., Altintas Y.: *Synchronized material deposition rate control with path velocity on fused filament fabrication machines*. Additive Manufacturing, 19. (2018) 205–213. https://doi.org/10.1016/j.addma.2017.05.011

[8] Huang B., Meng S., He H., Jia Y., Xu Y., Huang H.: *Study of processing parameters in fused deposition modeling based on mechanical properties of acrylonitrile-butadiene-styrene filament*. Polymer Engineering and Science, 59. (2019) 120–128. https://doi.org/10.1002/pen.24875

[9] Leite M., Guedes M., Marat-Mendes R., Baptista R.: *Effect of fused filament fabrication processing parameterson the mechanical properties of PLA components*. In: XVI. Portugese Conference of Fracture, Covilha, Portugal (2018) https://www.researchgate.net/publication/325847551

[10] Bikas H., Stavropoulos P., Chryssolouris G.: *Additive manufacturing methods and modelling approaches: a critical review.* International Journal of Advanced Manufacturing Technology, 83. (2016) 389–405. https://doi.org/10.1007/s00170-015-7576-2

[11] Chacón J. M., Caminero M. A., García-Plaza E., Núñez P. J.: *Additive manufacturing of PLA structures using fused deposition modeling: Effect of process parameters on mechanical properties and their optimal selection*. Materials and Design, 124. (2017) 143–157. https://doi.org/10.1016/j.matdes.2017.03.065

[12] Camargo J. C., Machado Á. R., Almeida E, C., Silva E. F. M. S.: *Mechanical properties of PLA-graphene filament for FDM 3D printing*. International Journal of Advanced Manufacturing Technology, (2019) (online) https://doi.org/10.1007/s00170-019-03532-5

Acta Materialia Transylvanica 2/1. (2019) 19–26.
https://doi.org/10.33924/amt-2019-01-04
Hungarian: https://doi.org/10.33923/amt-2019-01-04
https://eda.eme.ro/handle/10598/31424

Electrospinning of Polymer Fibres Using Recycled PET

Attila GERGELY,[1] József KÁNTOR,[2] Enikő BITAY,[3, 4] Domokos BIRÓ[5]

[1] *Sapientia Hungarian University of Transylvania, Faculty of Technical and Human Sciences Târgu Mureș, Department of Mechanical Engineering, Târgu Mureș, Romania, agergely@ms.sapientia.ro*

[2] *Elitex Prodexim Kft., Ceuașu de Câmpie, Romania, jkantor106@gmail.com*

[3] *Sapientia Hungarian University of Transylvania, Faculty of Technical and Human Sciences Târgu Mureș, Department of Mechanical Engineering, Târgu Mureș, Romania*

[4] *Transilvanian Museum Sociaty, Cluj Napoca, Romania, bitay@eme.ro*

[5] *Sapientia Hungarian University of Transylvania, Faculty of Technical and Human Sciences Târgu Mureș, Department of Mechanical Engineering, Târgu Mureș, Romania, dbiro@ms.sapientia.ro*

Abstract

The effective recycling of polymer materials remains unresolved to this day, and this has had a devastating effect on the environment. This study examines an alternative method to PET recycling that is the generation of polymer fibers and fiber mats for filtration applications. The electrospinning instrumentation used in this study had to be designed and built in order to carry out the research. We have managed to produce PET fibers with 200-600 nm diameter, and free-standing fiber mats that could potentially be used in filtration applications.

Keywords*: polymer fiber, electrospinning, recycling, PET.*

1. Introduction

The recycling of poly(ethylene terephthalate) (PET) is an urgent problem, since this material is exclusively used for the packaging of water and refreshing drinks. In the United States of America 12.7 % of the generated garbage was polymeric based materials in 2012 [1, 2]. Only 9 % of the polymeric material was recycled, and 30 % of this was PET bottles [3]. Recycled PET is used in many areas, such as in the automotive-, packaging-, textile industry, container manufacturing and foil production [4]. However, recycled PET cannot be used in the medical industries, in the manufacturing of protective clothing and some filtration applications [5, 6].

The PET material used to manufacture plastic bottles is semi crystalline, has good mechanical properties, is resistant to environmental effects and the products keep their shapes up to 70 °C [7, 8]. The manufacturing of plastic bottles involves the contact of PET with different additives and other material, thus recycled PET cannot be used in medical applications. Due to the increasing air pollution [9] and the advantageous mechanical properties of recycled PET [10], it could be potentially used in filtration applications.

There are several products that use polymer fibers in filtration applications. One of the methods that is capable of producing polymer fibers with nano- and micrometer range diameter is electrospinning. There are two way to generate polymer fibers with electrospinning: melt- and solution electrospinning [11]. Melt electrospinning requires the polymer to be molten. Thus, this process has high energy requirements. Additionally, the polymer fibers produced have relatively high diameter, in the micrometer range. Furthermore, the method seems to provide poor control over the fiber diameter [12]. Recycled PET fibers with melt electrospinning have resulted in fiber diameters of 30 μm [8]. In contrast to the mentioned disadvantages solution electrospinning has lower energy requirement and has proved a better in control of the produced polymer fiber diameter [10].

Figure 1. shows the schematics of a solution electrospinning instrument. The instrument has 3 major components: a high DC power supply, a

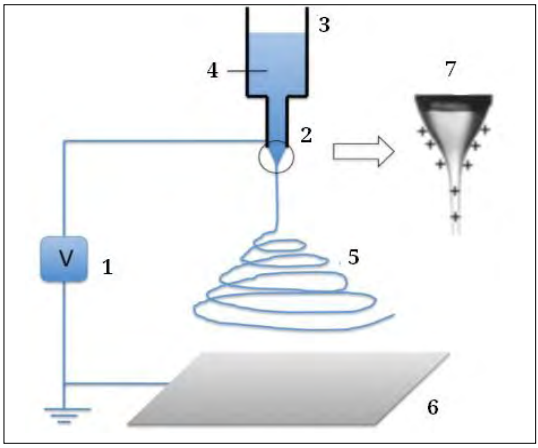

Figure 1. *Solution electrospinning setup* **[14]**. *1: high voltage power supply, 2: spinneret, 3: syringe, 4: polymer solution, 5: liquid jet, 6: collector, 7: Taylor cone*

container that holds the polymer solution, with a small opening, and a collector that is used to collect the polymer fibers. Solution electrospinning requires an electric field that charges and drives the charged polymer jet from the small opening of the container to the collector. In the process, the solvent, used to produce the polymer solution evaporates and the polymer fibers deposit on the collector in random orientation, with diameters in the nano- and/or micrometer range, producing a porous membrane (**Figure 2.**) **[11, 13]**.

The container is usually a syringe holding the polymer solution and is connected to a needle, serving as the small opening, with tubing. The needle is set to positive potential whereas the collector is set to either ground or negative potential. Due to the positive potential at the needle, the polymer solution becomes positively charged. The positive charges repel one another, and when the repelling forces become greater than the surface tension of the polymer solution a charged polymer jet is generated. The so-called Taylor cone that forms in the process is shown in **Figure 1. [15]**. During the travel of the charged polymer jet from the needle to the collector, almost all of the solvent evaporates, and the jet elongates, resulting the polymer fiber **[11, 13]**.

Strain et al. **[10]** used the solution electrospinning process to generate polymer fibermats from recycled PET. They used Coca-Cola PET bottles, trifluoroacetic acid (TFA) and dichloromethane (DCM) to prepare the polymer solution. The electrospinning parameters were set as follows: distance between the needle and the collector was 250 mm, the inner diameter of the needle was 0.6 mm, the flow rate was varied between 5, 10 and 20 µL/min, the applied potential difference was varied between 7 and 12 kV, whereas 10, 15 and 20 wt% polymer solution concentrations were used.

They produced polymer fibers with average fiber diameters between 0.4 and 4.3 µm. The authors concluded that the lower the polymer solution concertation the smaller the produced fiber diameters. The produced porous polymer membranes were used to manufacture a filtration device to filter cigarette fumes. The results show that the weight of a polymer membrane, produced by polymer fibers with 0.4 µm diameter, increased by 43 times after the filtration. Stain et. al concluded that the smaller the polymer fiber diameter the better the mechanical and filtration properties of the resulting fibermats. This result shows the potential use of recycled polymer fibermats in air filtration application. The publication generated great interest in the use of recycled PET in filtration applications. Since the original publication, recycled PET fibermats have been used in water filtration application too **[16]**.

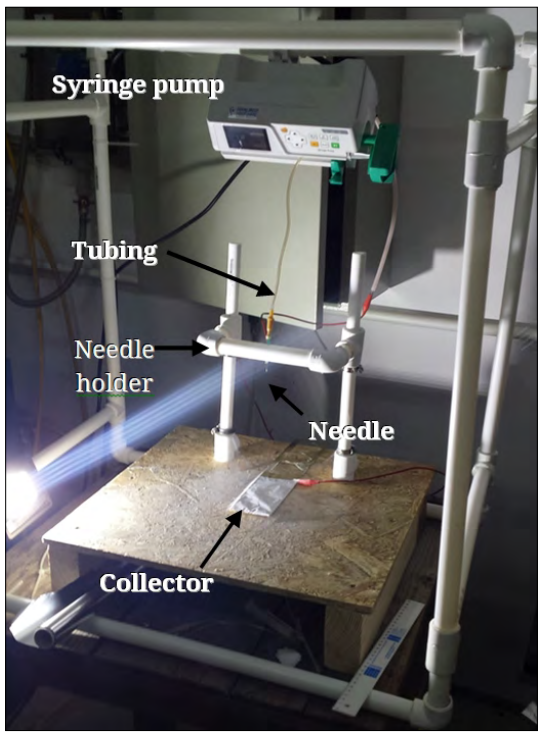

Figure 2. *The electrospinning equipment built for this project*

This study aims to investigate the effect of solution electrospinning parameters, such as polymer solution concentration, flow rate, applied potential difference, distance between needle tip and collector and the inner diameter (ID) of the needle, on the diameter of the produced recycled PET fibers and membrane morphology.

2. Experimental

2.1. Polymer solution

In the experiments Carpatica sparkling water bottles made of transparent PET were used. The bottles were washed with ethanol and were cut into squares of 10×10 mm^2. Solutions of PET with various concenteations were prepared in trifluoroacetic acid. The vials were placed on a shaker at 400 rpm. The PET completely dissolved in 15–90 minutes, depending on the concentration.

2.2. Electrospinning

Electrospinning was performed with an electrospinning instrument built within this project. The PET solutions were dispensed from 5 ml syringes through a 1/16 inch inner diameter polytetrafluoroethylene (PTFE) tube and a needle. The syringes were paced in a syringe pump, while the needles were inserted into the needle holder of the instrument. Positive high potential was connected to the needle and the collector was attached to the ground potential. The electrospinning was performed for 8 minutes per sample.

2.3. Scanning electron microscopy (SEM)

SEM imaging was carried out with a JEOL JSM-5200 scanning electron microscope at 10 kV potential and 1000x, 5000x and 10000x magnification. At x10000 magnification images were taken from three different spots of the fiber mats.

The fiber sizes were measured with the ImageJ software. The 10000x magnification images were used for fiber size measurement and at least 10 measurements were taken per image. In the case of beaded fibers at least 30 beads were measured per image.

3. Results

3.1. Instrumentation designing and building

The goal was to design an instrument that was easy to build and customize **Figure 2.** shows the instrument. The syringe pump was placed above the needle on a separate stand. The syringe was mounted in the pump, while the needle was placed in the needle holder. The syringe and the needle were connected with a PTFE tube. The collector was placed below the needle and the needle-collector distance could be adjusted. The image doesn't show the voltage source.

Figure 3. shows a porous PET fiber mat and its SEM image. It is white instead of transparent and it resembles a thin plastic foil. However, looking at the SEM image it can be seen that it's actually porous which is caused by the random orientation of the PET fibers.

3.2. Design of experiments

The list of electrospinning parameters used in the experiments can be seen in **Table 1.** Out of the plethora of factors the effects of PET concentration (C), volumetric flow rate (F), voltage (V), needle-collector distance (D), and the inner diameter of the needle (ID) on the electrospinning process were studied.

The conditions were created from the variation of these parameters in the following way:

- The effect of V was studied with the experimets 1, 2 and 3. C = 10 wt%, F = 15 µL/min, D = 250 mm, ID = 0.8 mm, and V = 15, 20 and 25 kV.
- The effect of F was studied with the experiments 2, 4, and 5. C = 10 wt%, V = 20 kV, D = 250 mm, ID = 0.8 mm, and F = 15, 30 and 45 µL/min.
- The effect of D was studied with the experiments 2, 8 and 9. C = 10 wt%, V = 20 kV, F = 30 µL/min, ID = 0.8 mm and D = 200, 250 and 300 mm.
- The effect of D was studied with the experiments 4, 6, and 7. C = 10 wt%, V = 20 kV, F = 15 µL/min, D = 250 mm and ID = 0.8, 0.55 and 0,3 mm.
- The experimental design was created with 5, 10 and 15 wt% solutions in mind, however the 15 wt% solution couldn't be spun which was due to its high viscosity.

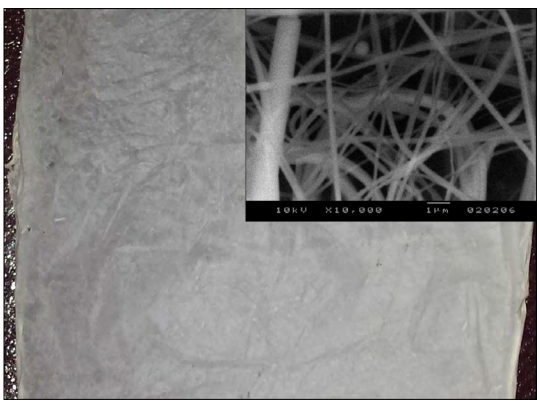

Figure 3. *PET fiber mat and its SEM image*

Table 1. *Performed electrospinning experiments*

No.	C (wt %)	F (µL/min)	V (kV)	D (mm)	ID (mm)	Fiber diameter (nm)	Bead diameter (µm)
1	10	15	15	250	0.8	289.6 ± 98.8	0 ± 0
2	10	15	20	250	0.8	502.8 ± 263.9	0 ± 0
3	10	15	25	250	0.8	452.4 ± 165.6	0 ± 0
4	10	30	20	250	0.8	322.4 ± 151.3	9.73 ± 4.40
5	10	45	20	250	0.8	359 ± 112.5	0 ± 0
6	10	30	20	200	0.8	549.3 ± 236.1	0 ± 0
7	10	30	20	300	0.8	407.1 ± 169.9	11.60 ± 3.85
8	10	15	20	250	0.55	297 ± 106.7	7.69 ± 2.42
9	10	15	20	250	0.3	377.4 ± 138.8	0 ± 0
10	5	15	15	250	0.8	126 ± 49	4.5 ± 1.3
11	5	15	20	250	0.8	0 ± 0	5.5 ± 0.8
12	5	15	25	250	0.8	118 ± 165.6	3.5 ± 1.1
13	5	30	20	250	0.8	283.5 ± 192.2	5.5 ± 1.7
14	5	45	20	250	0.8	171 ± 80.5	4.2 ± 2
15	5	30	20	200	0.8	295.9 ± 225.8	4.9 ± 2.4
16	5	30	20	300	0.8	346 ± 132.2	5.9 ± 2.1
17	5	15	20	250	0.55	159.7 ± 92.2	5.9 ± 1.9
18	5	15	20	250	0.3	245.9 ± 75.8	0 ± 0

3.3. Results of SEM examination

3.3.1. The effect of electrospinning parameters on fiber diameter

In the following the effect of the process parameters on the cross-sectional diameter of the produced PET fibers is discussed. The experiments were carried out with 5 and 10 wt% solutions, and the plots in **Figures 4–7**.

Figure 4. shows the PET fiber diameters as a function of V.

In **Figure 4.** it can be seen that in case of a C = 10 wt% solution by increasing the applied voltage, the PET fiber diameter also increased. At 15 kV fibers with 289.6 ± 98.8 nm diameter were produced while at 25 kV the average fiber diameter was 452.4 ± 165.6 nm. At 20 kV the PET fibers were a bit thicker with a diameter of 502.8 ± 263.9 nm, which had a large deviation. These results match well with the data reported in the literature **[10]**. According to an explanation found in the literature the higher voltage generates a stronger electric field, which increases the local volumetric flow rate at the tip of the needle and this leads to the increase of fiber size. In case of C = 5 wt% this effect wasn't as strong as it had been for the 10 wt% solution. On the other hand at V = 15 kV the average diameter of PET fibers was 126 ± 49 nm, and beading also occurred with bead sizes of 4.5 ± 1.3 µm. At 20 kV there were barely any fibers and the bead sizes were 5.5 ± 0.8 µm. At 25 kV the morphology consisted of beaded fibers and standalone beads. The average fiber diameter was 118 ± 165.6 nm. Voltage had a low influence on fiber diameter at C = 5 wt%.

The F vs. fiber diameter plot can be seen in **Figure 5.**

The general trend reported in the literature is that higher volumetric flow rates lead to thicker fibers. The results shown in **Figure 5.** indicate that for C = 10 wt% the increase in fiber diameter occurred between F = 30 and 45 µL/min. The

increase of fiber diameter was due to a larger amount of solution getting into the solution jet at the higher flow rates. For C = 5 wt% the increase of fiber size with higher F did not occur, however there weren't many fibers to begin with, and instead beads formed. The bead sizes were 5.5 ± 0.8 µm, 5.5 ± 1.7 µm and 4.2 ± 2 µm at 15, 30 and 45 µL/min respectively.

Figure 6. shows the fiber diameter-D plot.

It can be seen that at C = 10 wt% the diameter vs. D plot had a minimum value at D = 250 mm. For D = 200 mm needle-collector distance the average fiber diameter was 549.3 ± 236.1 nm, for D = 250 mm it was 322.4 ± 151.3 nm, and for D = 300 mm it was 407.1 ± 169.9 nm. According to the literature at short needle-collector distances there is only a short time for the evaporation of the solvent, resulting in wet fibers which have a relatively large diameter. As the distance increases, the fibers are able to dry out more, and the fiber diameters decrease. Further studies are necessary to explain the difference between our results and the results reported by others.

At C = 5 wt% there was a similar tendency, but in this case there were also beads forming. The bead diameters were similar for all three experi-

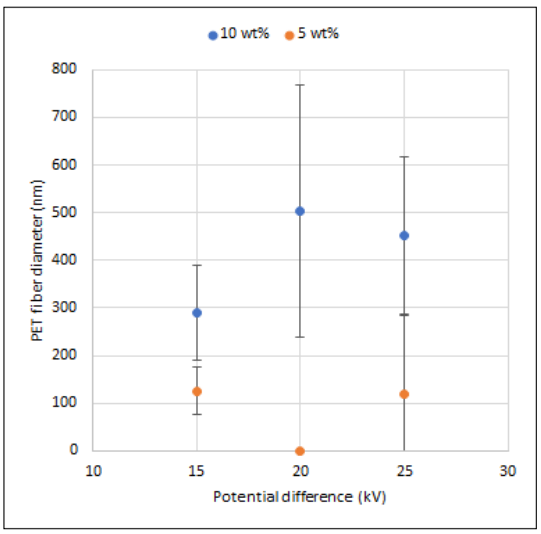

Figure 4. *The effect of V on the fiber diameter. F = 15 µL/min, D = 250 mm, ID = 0.8 mm*

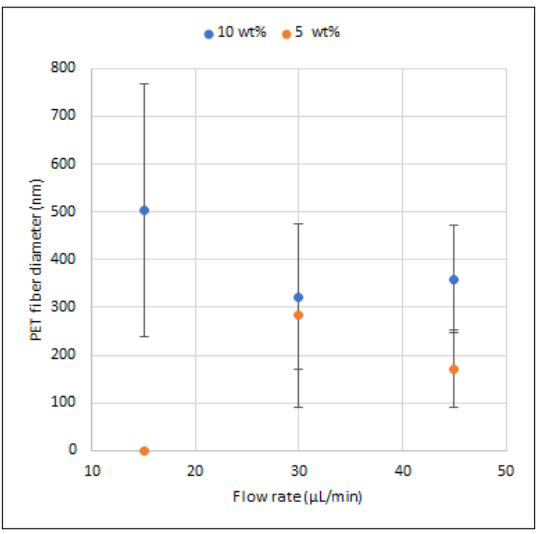

Figure 5. *The effect of F on the fiber diameter. 20 V = kV, D = 250 mm, ID = 0.8 mm*

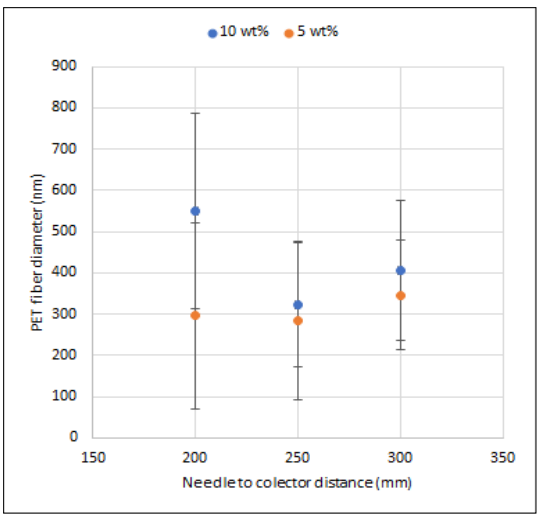

Figure 6. *The effect of D on the fiber diameter. V = 20 kV, F = 30 µL/min, ID = 0.8 mm*

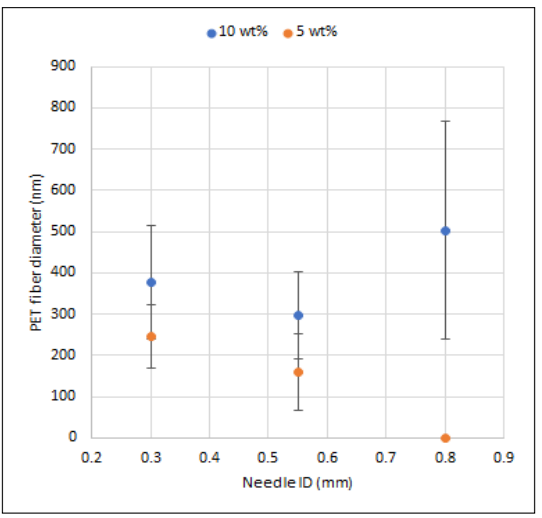

Figure 7. *The effect of ID on the fiber diameter. V = 20 kV, F = 15 µL/min, D = 250 mm*

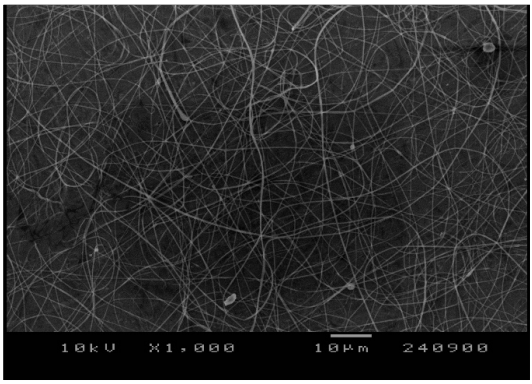

C = 5 wt%, ID = 0,3 mm

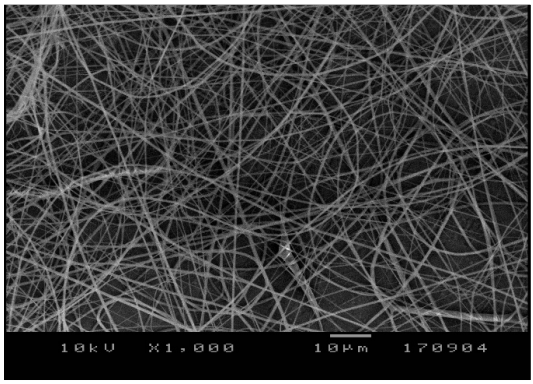

C = 10 wt%, ID = 0,3 mm

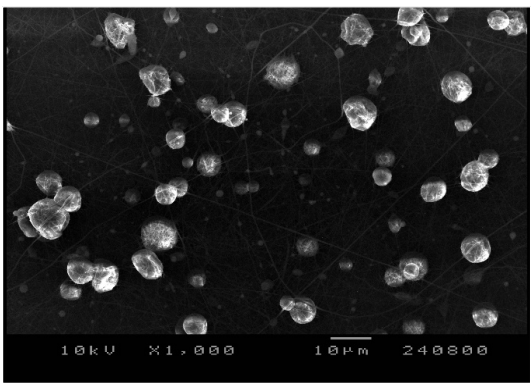

C = 5 wt%, ID = 0,55 mm

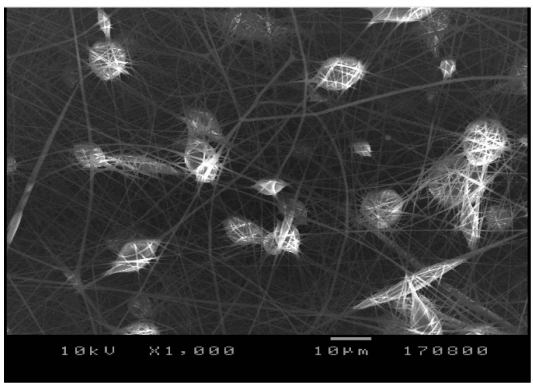

C = 10 wt%, ID = 0,55 mm

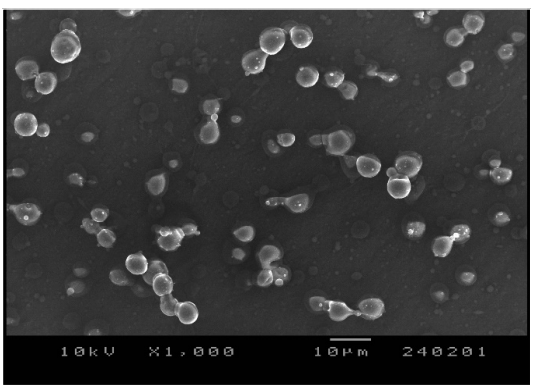

C = 5 wt%, ID = 0,8 mm

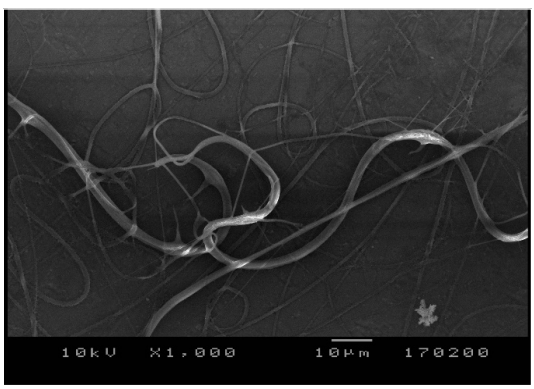

C = 10 wt%, ID = 0,8 mm

Figure 8. *SEM micrographs of beaded PET fibers in function of ID. C = 5 and 10 wt%, V = 20 kV, F = 15 µL/min, and D = 250 mm*

ments, 5.9 ± 2.1 at μm D = 200 mm, 5.5 ± 1.7 μm at D = 250 mm and 5.9 ± 1.9 μm at D = 300 mm.

The fiber diameter vs. ID plots are shown in **Figure 7.**

As the plots indicate, experiments with lower ID did not produce thinner fibers. In both cases – C = 5 and 10 wt%, at 0.3 mm ID the fiber diameters were 245.9 ± 75.8 nm and 377.4 ± 138.8 nm – larger than in case of a 0,55 mm ID: 159.7 ± 92.2 nm and 297 ± 106.7 nm. It should be noted that at C = 5 wt% and ID = 0.3 mm beads weren't produced, while in all other experiments with C = 5 wt% the mats contained beads. Interestingly at C = 5 wt%, ID = 0.8 mm there were beads with 5.5 ± 0.8 μm diameter, and no fibers. However at C = 10 wt% and ID = 0.8 mm there weren't any beads, and the PET fibers had diameters of 502.8 ± 263.9 nm.

Generally speaking **Figures 4–7.** indicate that fiber diameter is strongly influenced by the concentration of the PET solution. It should be emphasized that, as confirmed by the literature at lower concentrations beaded fibers or standalone beads appear.

3.3.2. The effects of electrospinning parameters on fiber mat morphology

The investigation of the fiber mat morphology showed that at 5 wt% PET concentration – with one exception – beaded fibers were produced or in ceration cases almost exclusively beads. At 10 wt% concentration beading occurred in experiments 4, 7, and 8, but most of these were attached to fibers. These results are in accordance with those reported in the literature, i.e. beads are less likely to form at higher solution concentrations.

In **Figure 8.** SEM images of the electrospun fiber mats can be seen, in function of various ID values, with C = 5 and 10 wt%, V = 20 kV, F = 15 μL/min, and D = 250 mm.

4. Conclusions

In summary it can be stated that the designed electrospinning instrument is capable of producing PET fibers. In addition the effects of electrospinning parameters on fibers created from the recycled Carpatica sparkling water bottles were investigated. The results are in good agreement with the data published in the literature from a qualitative perspective. PET fibers with 200–600 nm diameters were successfully spun. The produced fiber mats can potentially be used in filtration applications.

Acknowledgements

We would like to thank Dr. László Jakab-Farkas for his help in the SEM imaging. The research was funded by the Institute of Research Programs (Kutatási Programok Intézete, KPI), 13/14/17.05.2017.

References

[1] Khan W. S., Asmatulu R., Davuluri S., Dandin V. K.: *Improving the Economic Values of the Recycled Plastics Using Nanotechnology Associated Studies*. Journal of Materials Science & Technology, 30/9. (2014) 854–859. https://doi.org/10.1016/j.jmst.2014.07.006

[2] EPA U.S. Environmental Protection Agency, Wastes – Resource Conservation – Common Wastes & Materials – Plastics. http://www.epa.gov/osw/conserve/materials/plastics.htm

[3] Welle F.: *Twenty years of PET bottle to bottle recycling – an overview*. Resources, Conservation and Recycling, 55/11. (2011) 865–875. https://doi.org/10.1016/j.resconrec.2011.04.009

[4] Oromiehie A., Mamizadeh A.: *Recycling PET beverage bottles and improving properties*. Polymer International, 53/6. (2004) 728–732. https://doi.org/10.1002/pi.1389

[5] Veleirinho B., Rei M. F., Lopes-Da-Silva J. A.: *Solvent and concentration effects on the properties of electrospun poly(ethylene terephthalate) nanofiber mats.* Journal of Polymer Science, Part B: Polymer Physics, 46/5. (2008) 460–471. https://doi.org/10.1002/polb.21380

[6] G. Li, Y. Zhao, M. Lv, Y. Shi, D. Cao: *Super hydrophilic poly(ethylene terephthalate) (PET)/poly(vinyl alcohol) (PVA) composite fibrous mats with improved mechanical properties prepared via electrospinning process.* Colloids and Surfaces A: Physicochemical and Engineering Aspects, 436. (2013) 417–424. https://doi.org/10.1016/j.colsurfa.2013.07.014

[7] Awaja F., Pavel D.: *Recycling of PET.* European Polymer Journal, 41/7. (2005) 1453–1477. https://doi.org/10.1016/j.eurpolymj.2005.02.005

[8] Rajabinejad H., Khajavi R., Rashidi A., Mansouri N., Yazdanshenas M. E.: *Recycling of used bottle grade poly ethyleneterephthalate to nanofibers by melt-electrospinning method.* International Journal of Environmental Reserch and Public Health, 2009/3. 663–670.

[9] Anandjiwala R. D., Boguslavsky L.: *Development of needle-punched nonwoven fabrics from flax fibres for air filtration applications.* Textile Research Journal, 78. (2008) 614–624. https://doi.org/10.1177%2F0040517507081837

[10] Strain I. N., Wu Q., Pourrahimi A. M., Hedenqvist M.S., Olsson R. T., Andersson R. L.: *Electrospinning of recycled PET to generate tough mesomorphic fibre membranes for smoke filtration.* Journal of

Materials Chemistry A, 3/5. (2015) 1632–1640. https://doi.org/10.1039/C4TA06191H

[11] Huang Z.-M., Zhang Y.-Z., Kotaki M., Ramakrishna S.: *A review on polymer nanofibers by electrospinning and their applications in nanocomposites.* Composites Science and Technology, 63/15. (2003) 2223–2253. https://doi.org/10.1016/S0266-3538(03)00178-7

[12] Thompson C. J., Chase G. G., Yarin A. L., Reneker D. H. : *Effects of parameters on nanofiber diameter determined from electrospinning model.* Polymer, 48/23. (2007) 6913–6922. https://doi.org/10.1016/j.polymer.2007.09.017

[13] Reneker D. H., Yarin A. L.: *Electrospinning jets and polymer nanofibers.* Polymer, 49/10. (2008) 2387–2425. https://doi.org/10.1016/j.polymer.2008.02.002

[14] Athira K., Sanpui P., Chatterjee K.: *Fabrication of Poly(Caprolactone) Nanofibers by Electrospinning.* Journal of Polymer and Biopolymer Physics Chemistry, 2/4. (2014) 62–66.

[15] Taylor G. I.: *Electrically driven jets.* Proceedings of Royal Society A, 313/1515. (1969) 453–475. https://doi.org/10.1098/rspa.1969.0205

[16] Zander N. E., Gillan M., Sweetser D.: *Recycled PET Nanofibres for Water Filtration Applications.* Materials, 9/4. (2016) 247–253. https://doi.org/10.3390/ma9040247

sciendo

Acta Materialia Transylvanica 2/1. (2019) 27–31.
https://doi.org/10.33924/amt-2019-01-05https://doi.org/10.33923/amt-2019-01-05
https://eda.eme.ro/handle/10598/31425

ACTA MATERIALIA TRANSYLVANICA

Mechanical and Microstructural Features of Ceramic Hollow Spheres

Alexandra KEMÉNY[1, 2, a], Dóra KÁROLY[1, 2, b]

[1]*Budapest University of Technology and Economics, Faculty of Mechanical Engineering, Department of Materials Science and Engineering, Budapest, Hungary*

[2]*MTA–BME Lendület Composite Metal Foams Research Group, Budapest, Hungary*

[a] *alexa@eik.bme.hu*

[b] *kdora@eik.bme.hu*

Abstract

In this study two different types of hollow sphere were examined by mechanical, geometrical and microstructural measurements, and the fracture force, geometrical properties and chemical composition were determined. The diameter of the „01 globocer" type specimens was 2.37 mm on average, while the value for the „03 globocer" type specimens was 6.88 mm, both were smaller than the nominal diameter. The average deviation from the circularity of the 01 globocer specimens was 8 %, the value for the 03 globocer specimens was 6 %, while the average wall porosity was 53±3 % and 56±3 % respectively. The surface of the hollow spheres was uneven, which has an impact on the contact surfaces during pressure tests, which affects the fracture force values. The average value of the fracture force of 01 globocer spheres was 42 N, and of 03 globocer hollow spheres was 288 N. The diameter had a bigger impact on the fracture force values of the type 01 specimens than in the case of 03.

Keywords*: ceramic hollow sphere, metal foam, mechanical properties.*

1. Introduction

Nowadays the reduction of a components' mass with the enhancement of specific mechanical properties plays a primary role in industrial applications. Materials design methods are increasingly focusing on lightweight materials considering energy efficiency and the best value for money. Increasing the specific resistance of the structure or the equipment to compressive loads can be achieved by using lower density and higher strength materials, to which closed cellular metal foams provide one of the best solutions. This composite material is mainly used in vehicles as an energy absorber or sandwich panel [1].

Metal matrix syntactic foams (MMSFs) are a special type of closed cell foams, where the porosity inside the metallic matrix is ensured by a second phase or filling material. Various matrix and filler materials are investigated in the literature, but the most common type of the latter is the ceramic hollow sphere, which can be made from mixed oxide ceramics [2, 3], high purity and quality alumina [4, 5] or silicon carbide [6, 7]. There are experiments in using metallic hollow spheres [8] or expanded perlite [9, 10] too. Syntactic foams made with these spheres have excellent specific energy absorbing properties and compressive strength, but their price is relatively high [11].

The properties of the filler materials alone are a poorly researched area, although they have a great impact on the produced metal foams' properties. Dong et al., and Ruan et al. investigated the fracture mechanisms of thin-walled hollow spheres during dynamical compression tests. Both groups made compression measurements with different sized compression tools and different strain rates. They reported that the load speed greatly affects the mode of the failure [12, 13].

Song et al. examined the microstructure and failure methods of metallic hollow spheres with both experimental and finite element methods. The different distribution of microporosity in the sphere walls resulted in diverse failure modes in each case [14].

Since there are only a few studies available on the subject, and as other research groups have investigated the compression behaviour of material hollow spheres other than ceramic, this research aims at to investigate the geometrical, microstructural and mechanical properties of two commonly used ceramic hollow sphere types.

2. Materials and methods

Two types of ceramic hollow spheres were tested (Figure 1.) from Hollomet during the research. From both types, 50-50 different pieces were examined for various mechanical, geometrical and microstructural properties.

The nominal material type, bulk density and diameter of the investigated hollow spheres are shown in Table 1.

First, the diameter of the samples was measured using a Mitutoyo Absolute Digimatic CD-15DC caliper, rotating the specimens to determine the average deviation from circularity. Then, the fracture measurement of the hollow spheres was performed at the rate of 0.1 mm/min between two flat plates (Figure 2.). The examination was performed with an Instron 5965 electromechanical universal material testing device.

Embedded in a two-component epoxy resin, the hollow spheres were polished up to their centerplane, so that the wall thickness, internal structure, porosity and the circularity of the samples were examined optically by Olympus SZX16 stereo and Olympus PMG-3 metallurgical microscopes. The deviation from circularity was determined by the formula (1), with the smallest and largest measured values D_{min} and D_{max} respectively.

$$\frac{D_{max} - D_{min}}{\overline{D}} \cdot 100\ (\%) \qquad (1)$$

For further investigation of the morphology, a Zeiss EVO MA10 scanning electron microscope (SEM) was used, and the composition of the material was determined by the microscope EDAX energy dispersive X-ray spectrometry (EDS) module. Images were made with 20 kV accelerating voltage and a secondary electron detector.

Table 1. *Data of the examined ceramic hollow spheres*

	Material	ρ (g/cm³)	ØD$_n$ (mm)
01 globocer	Al_2O_3 C795	0,59	2,4
03 globocer	Al_2O_3 C795	0,60	7,0

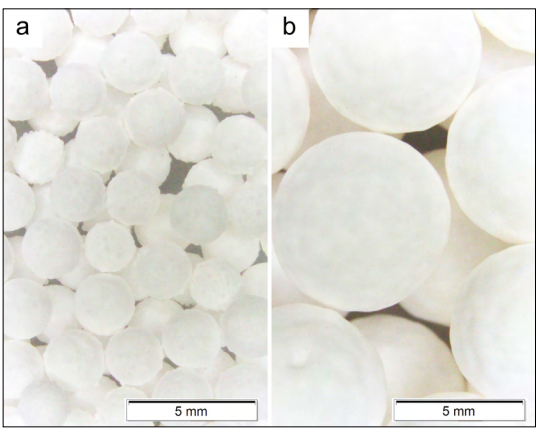

Figure 1. *Macro image of the investigated hollow spheres: 01 globocer® (a) and 03 globocer® (b)*

3. Results

The average (Ø$\overline{D}$) and the standard deviation (s) of the measured diameters of the hollow spheres are shown in Table 2. It can be observed that the samples are smaller on average than the nominal size.

In addition to measuring the diameters with a calliper, the circularity of the samples and the thickness of the samples were measured using a stereomicroscope on the embedded and polished samples. As can be seen in Figure 3., the test samples, although close to circular, have uneven surfaces and wall thicknesses, which can have a

Figure 2. *Mechanical testing layout*

major impact on their mechanical properties, depending on the direction of the load. The average deviation from the circularity of 01 globocer was 8 % and that of 03 globocer was 6 %.

The average thickness of the wall measured with the microscope is 0.125 mm for 01 globocer and 0.346 mm for 03 globocer. The data can be used to calculate the average diameter factor resulting from the ratio of internal to external diameter (**Table 3.**).

Based on pressure infiltration technique, which results a ~64 % filling and homogeneous filler distribution using the random close-packing theory **[15]**, the ratio of internal and external diameters and theoretical porosity (P_{FOAM}) of metal foam can be calculated **[16, 17]**.

The more accurate examination of surface morphology was possible by scanning electron microscopy (**Figure 4.**). Both types of ceramic hollow spheres have an uneven surface, but the smaller spheres are more uneven than the larger ones. The outer and inner surfaces of the hollow spheres are rough compared to their whole sizes.

The morphology of the internal porosity was observed on metallurgical microscopic images (**Figure 5.**), and on the fracture surface of the samples' walls (SEM) (**Figure 6.**).

Table 2. *Diameter values of the examined hollow spheres*

	01 globocer	03 globocer
$Ø\bar{D}$ (mm)	2,37	6,88
$ØD_{min}$ (mm)	2,00	6,44
$ØD_{max}$ (mm)	2,65	7,36
s (mm)	0,13	0,22

Table 3. *The diameter ratio and theoretical porosity value of the examined hollow spheres*

	01 globocer	03 globocer
$Ø\bar{d}$ (mm)	2,12	6,19
$\sum_{i=1}^{n} \frac{Ød_i/ØD_i}{n}$	0,90	0,90
P_{FOAM} (%)	55	58

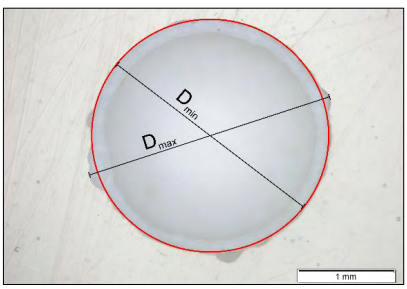

Figure 3. *Cross section image of 03 globocer hollow sphere*

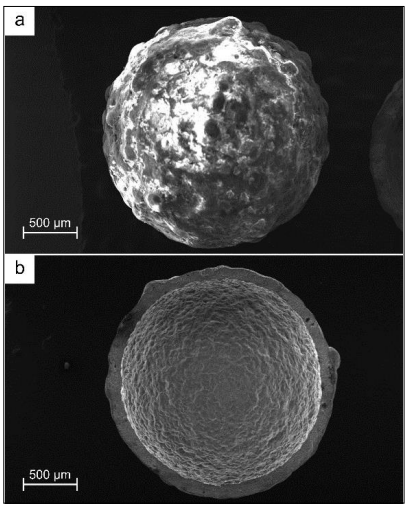

Figure 4. *SEM image of the outer (a) and inner (b) surface of 01 globocer hollow sphere*

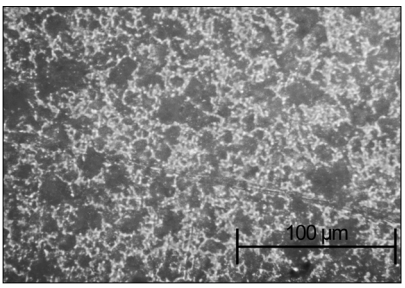

Figure 5. *Metallurgical microscopic image of the wall of 03 globocer hollow sphere*

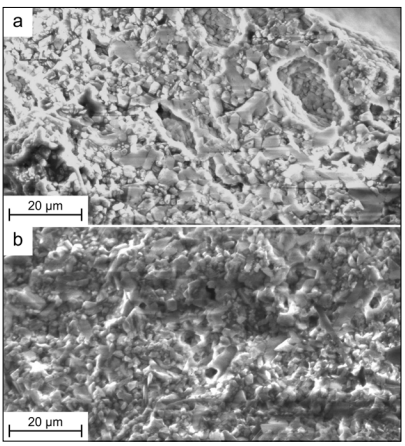

Figure 6. *Inner porosity of 01 globocer (a) and 03 globocer (b)*

This shows that, although made of the same material, pores in the smaller diameter hollow spheres were larger than those found in the larger diameter hollow spheres. The total porosity was in opposition to this observation (for 01 globocer 53±3 % and for 03 globocer 56±3 %).

In addition a part of the hollow spheres are not floating on the surface of the water, but sink beneath. This is caused by the high porosity of the walls.

The mechanical characterization of the hollow spheres was marked by the fracture force, because due to the unevenness of the wall thickness of the hollow spheres, an acceptable stress value could not be obtained. The fracture force is the maximal force measured during the compression tests.

Figures 7–8. show the fracture forces of the two different sample correlated to their diameter. It can be observed that in the smaller hollow spheres, the deviation of the diameter influences the force value associated with the failure; there is a correlation between the two values.

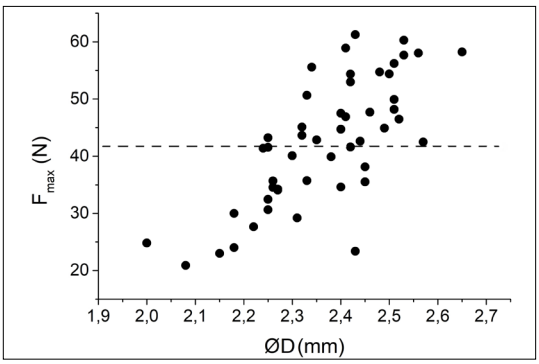

Figure 7. *Fracture force of 01 globocer in correlation to the diameter values*

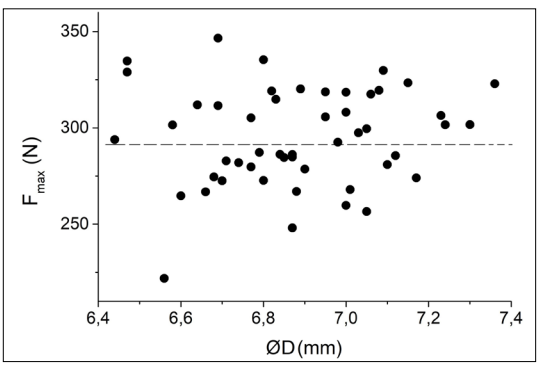

Figure 8. *Fracture force of 03 globocer in correlation to the diameter values*

Table 4. *Composition of the examined hollow spheres*

	O (t%)	Al (t%)
01 globocer	56±4	42±3
03 globocer	49±3	50±5

Table 4. shows the composition of the aluminium oxide based ceramic hollow spheres measured by EDS measurement as the average of at least 3 different spots on one sample, on the total of 3 different samples' fracture surfaces from each type.

It can be observed that the measured average values show 97–99 wt% aluminium and oxygen in the material. Also the spheres may contain 1 % or less Si and Ca too. This value is in accordance with the IEC 60672-3:1997 standard and the manufacturer specified C795 material.

4. Conclusions

Overall, it can be stated that it is important to have measurement data on mechanical, geometrical and microstructural properties of the ceramic hollow spheres – which are often used as filler in metal foams – for engineering design purposes. The following observations were made during the research:

- the diameter of the 01 globocer specimens was 2.37 mm on average, while the value for the 03 globocer specimens was 6.88 mm, both were smaller than the nominal diameter;
- the average deviation from circularity of the 01 globocer specimens was 8 %, the value for the 03 globocer specimens was 6 %;
- the surface of the hollow spheres was uneven, which has an impact on the contact surfaces during pressure tests, which affects the fracture force values;
- the average wall porosity of 01 and 03 globocer specimens was 53±3 % and 56±3 % respectively;
- the average value of the fracture force of 01 globocer spheres was 42 N, with the standard deviation of 12.5 N, and of 03 globocer hollow spheres, the average was 288 N, with the standard deviation of 41 N;
- the diameter had a bigger impact on the fracture force values of the type 01 specimens than in the case of 03;
- and it can be stated that both sized ceramic hollow spheres' material is in accordance with the quality that manufacturer specified.

Acknowledgement
The publication reported herein has been supported by the Gépészmérnök-képzésért Alapítvány.

References

[1] Gupta N., Rohatgi P. K.: *4.15 Metal Matrix Syntactic Foams.* In: Comprehensive Composite Materials II. Elsevier, Oxford, 2018. 364–385. doi.org/10.1016/B978-0-12-803581-8.09971-9

[2] Szlancsik A., Katona B., Károly D., Orbulov I. N.: *Notch (In)Sensitivity of Aluminum Matrix Syntactic Foams*. Materials, 12/574. (2019) 15. doi.org/10.3390/ma12040574

[3] Zhang Q., Lee P. D., Singh R., Wu G., Lindley T. C.: *Micro-CT characterization of structural features and deformation behavior of fly ash/aluminum syntactic foam.* Acta Materialia 57. (2009) 3003–3011. doi.org/10.1016/j.actamat.2009.02.048

[4] Ferguson J. B., Santa Maria J. A., Schultz B. F., Rohatgi P. K.: *Al–Al_2O_3 syntactic foams–Part II: Predicting mechanical properties of metal matrix syntactic foams reinforced with ceramic spheres*. Materials Science and Engineering, A 582. (2013) 423–432. doi.org/10.1016/j.msea.2013.06.065

[5] Omar M. Y., Xiang C., Gupta N. Strbik, O. M., Cho K.: *Data characterizing flexural properties of Al/Al_2O_3 syntactic foam core metal matrix sandwich.* Data Br, 5. (2015) 564–571. doi.org/10.1016/j.dib.2015.09.054

[6] Katona B., Szlancsik A., Tábi T., Orbulov I. N.: *Compressive characteristics and low frequency damping of aluminium matrix syntactic foams*. Materials Science and Engineering, 739. (2019) 140–148. doi.org/10.1016/j.msea.2018.10.014

[7] Cox J., Luong D. D., Shunmugasamy V. C., Gupta N., Strbik O. M., Cho K.: *Dynamic and Thermal Properties of Aluminum Alloy A356/Silicon Carbide Hollow Particle Syntactic Foams*. Metals, 4. (2014) 530–548. doi.org/10.3390/met4040530

[8] Pérez L., Villalobos M., Órdenes C., Drew R. A. L., Ruiz-Aguilar C., Alfonso I.: *Elastic Modulus Estimation for Copper Syntactic Foams Reinforced with Iron Hollow Spheres of Different Wall Thicknesses.* Journal of Materials Engineering and Performance, 28/1. (2019) 100–106. doi.org/10.1007/s11665-018-3827-3

[9] Taherishargh M., Belova I. V., Murch G. E., Fiedler T.: *The effect of particle shape on mechanical properties of perlite/metal syntactic foam.* Journal of Alloys and Comppunds, 693. (2017) 55–60. doi.org/10.1016/j.jallcom.2016.09.168

[10] Fiedler T., Taherishargh M., Krstulovic-Opara L., Vesenjak M.: *Dynamic compressive loading of expanded perlite/aluminum syntactic foam.* Materials Science and Engineering, A, 626. (2015) 296–304. doi.org/10.1016/j.msea.2014.12.032

[11] Szlancsik A., Katona B., Orbulov I. N., Taherishargh M., Fiedler T.: *Fatigue properties of EP/A356 aluminium matrix syntactic foams with different densities.* IOP Conference Series: Materials Science and Engineering, 426. (2018) 8p. doi.org/10.1088/1757-899X/426/1/012045

[12] Dong X.L., Gao Z.Y., Yu T.X.: Dynamic crushing of thin-walled spheres: An experimental study. International Journal of Impact Engineering, 35/8. (2008) 717–726. doi.org/10.1016/j.ijimpeng.2007.11.004

[13] Ruan H. H., Gao Z. Y., Yu T. X.: *Crushing of thin-walled spheres and sphere arrays*. International Journal of Mechanical Science, 48/2. (2006) 117–133. doi.org/10.1016/j.ijmecsci.2005.08.006

[14] Song J., Sun Q., Luo S., Arwade S. R., Gerasimidis S., Guo Y., Zhang G.: *Compression behavior of individual thin-walled metallic hollow spheres with patterned distributions of microporosity*. Materials Science and Engineering A, 734. (2018) 453–475 doi.org/10.1016/j.msea.2018.08.016

[15] Finney J. L.: *Random packings and the structure of simple liquids I. The geometry of random close packing.* Royal Society of London A, 319/1539. (1970) 479–493. doi.org/10.1098/rspa.1970.0189

[16] Gupta N., Woldesenbet E., Mensah P.: *Compression properties of syntactic foams: effect of cenosphere radius ratio and specimen aspect ratio.* Composites Part A: Applied Science and Manufacturing, 35/1. (2004) 103–111. doi.org/10.1016/j.compositesa.2003.08.001

[17] Kiser M., He M. Y., Zok F. W.: *The mechanical response of ceramic microballoon reinforced aluminum matrix composites under compressive loading.* Acta Materialia, 47/9. (1999) 2685–2694. doi.org/10.1016/S1359-6454(99)00129-9

Acta Materialia Transylvanica 2/1. (2019) 32–42.
https://doi.org/10.33924/amt-2019-01-06
Hungarian: https://doi.org/10.33923/amt-2019-01-06
https://eda.eme.ro/handle/10598/31426

Examination of Laser Microwelded Joints of Additively Manufactured Individual Implants

János KÓNYA,[1] Klaudia KULCSÁR[2]

[1] *Dent-Art-Technik Kft. Győr, Hungary, labor@dentarttechnik.hu*

[2] *Dent-Art-Technik Kft. Győr, Hungary, kulcsar.klaudia@dentarttechnik.hu*

Abstract

Digital product processing and the utilization of novel, tissue-friendly materials allow the use of fixed dentures for patients. Its basis is a titanium plate fixed to the cortical bone surface at given screw positions. A digital dental cast is created from the existing bone surface, and modelling and necessary statistical analyses are carried out in a virtual environment. Safety of the welded joint is evaluated with mechanical methods. When designing the fixing points, an idealized denture is used that was previously designed for the patient. The number and position of pillar elements used for screw fixation of the denture are determined by the complex geometry of the denture itself, and the location, direction, and articulating position of existing teeth. The additively manufactured implant and the machined pillar sleeves are joined with laser-welding at given nesting positions. Homogeneity of the metallic material structure at the welded joint zone of the product is examined with micro-CT. Due to this implementation method, surgical time decreases together with complication rates and post-operative problems.

Keywords*: additive manufacturing, implant, laser micro welding, titanium, 3D printing.*

1. Introduction

Titanium and its alloys are among the best metallic materials of choice in industrial and medical applications. Ti-6Al-4V alloy is mainly used in aerospace and for surgical implant material as well due to its high tensile and fatigue strength and good corrosion resistance [1]. Titanium – commercially pure titanium or titanium alloy – welding can be necessary in aerospace industry, but also in the manufacturing of medical instruments. Titanium and its alloys have several advantages in surgical implant and prosthesis manufacturing because of their outstanding corrosion resistance, mechanical properties, and biocompatibility [2]. Laser welding is present in the manufacturing process of diverse medical products, such as pacemakers, defibrillators, catheters, and orthopaedic implants [3]. Biocompatible metals and alloys e.g. titanium, nitinol, cobalt-based alloys, stainless steel, platina, and niobium are used for implantable devices. Titanium is a unique material that requires special attention in every processing step, especially in welding [4]. Titanium has a complicated welding technology as at temperatures higher than 550 °C, and especially in liquid phase, it is highly reactive with atmospheric gases such as oxygen and nitrogen. Inadequate preparation or cleaning of jointing and filling materials, insufficient protection of weld joint zone or inert gas contamination before or during welding can cause material impurities [5–7].

Several joining technologies are used for titanium materials, for example tungsten inert gas welding, laser welding, and brazing [2]. Three different techniques for jointing material layup on metallic components are investigated in today's practice: direct laser welding, electron beam deposition [8–10], and shaped metal deposition (SMD) [11]. Argon atmosphere provides a cost-effective solution compared to processes that require a high vacuum chamber [15]. Titanium welding is mostly carried out with a high-energy beam in inert atmosphere. Electron beam welding, despite its high costs, is fully capable of fusing

titanium particles together. The vacuum chamber protects high-temperature material during the welding process and impurities will not be present [16, 17]. The widely-used welding process for titanium alloys is gas tungsten arc welding due to its simple applicability and cost-effectiveness. Magnetic arc oscillation and electric current impulse welding are more popular as these technologies are possibly applicable in actual industrial situations with minor modifications of existing welding machines [18].

Several studies investigated the effect of air contamination on the microstructure and mechanical properties of welded joints in pure titanium and titanium alloys [19]. Two welding technologies were compared in additively manufactured Ti-6Al-4V alloy: one possible solution was Nd:YAG laser welding, the other was tungsten inert gas welding [20]. Several methods were successfully implemented to obtain a fine-grained microstructure at the welded joint zones, such as surface nucleation induced by choked gas flow. Experiments with grade 2 titanium alloy concluded that welded zone pigmentation is correlated with the absence of inert gas, oxygen and nitrogen content in welded zones, and mechanical properties of the joint [19]. However, this correlation is also affected by other variables apart the surficial colour of the welded joint and material impurities. It was detected that the surface colour of the welded zone only indicated surficial impurities [19]. The effect of oxygen contamination in the argon atmosphere on welded material microstructure and material properties was investigated during laser welding of thin titanium plates. Welded joint examination was carried out mostly with optical and scanning electron microscopes. Mechanical tests revealed a relationship between the colour of the welded joint surface and the structure and mechanical properties (strength, ductility, hardness) of the welded joint [19].

2. Precision cast subperiosteal implant

The re-thought implant structure was created with a conventional casting process, which met considerable practical difficulties. Necessary manual post-processing steps become more difficult due to problems with metal structure homogeneity, wear and erosion of the ceramic embedding cast, and embedding of ceramic wear debris into the implant structure. The cast contained only one structural element where the perforated membrane for the contact surface and the fixing pillars were cast together as one piece (Figure 1.). Design of screw locations was carried out after parallel positioning.

The metal structure was subjected to non-destructive material testing with micro-CT to analyse material homogeneity after hole-drilling and threading (Figure 2.). During software evaluation of results, material defects were found in more than 80 % of casts. The purpose of our first corrective measure was to open up and fill internal voids using a laser welding machine. Following this intervention, mechanical strength and machinability of this filled-up material structure differed from the original cast material, which further aggravated the creation of fixing points.

3. Design and evaluation of dual-phase pillars

Using the previous results and experiences a complex new solution was found. It meant the laser welding of the cast base structure and the machined axis-symmetric and parallel pillar elements. The final fixing points had already been created on these pillar elements. It provided a good technical solution as it allowed the necessary mechanical strength and structural stability. The precise machinability of the welded pillar element connecting to the base structure made it possible to create high-precision surficial fitting for further implant connecting elements.

Figure 1. *Raw cast of one-piece titanium metal structure, and the device ready to be implanted*

Connecting elements for this dual-phase implant were necessary so that the surgical wound could be closed during the implantation procedure and healing time was reduced. Hereby, threaded sleeves of fixing pillars can be closed with so called healing screws.

Other advantages of threaded sleeves are detachability, maintainability, and diversity of pillar geometries that are applicable in different environments. It embodies the possibility of both axis correction and solutions for special anatomical positions and different gingival thicknesses.

Our implants that had been manufactured previously in this way did not possess a thorough background in material testing and structure analysis. It was provided by virtual design, a new level of information retrieved from (Cone Beam Computer Tomography) CBCT images, and special software. Hereby, the subperiosteal implant was completely re-thought. It was now manufactured with 3D subtractive technology after virtual product design. Both the frame structure, the fixing pillars, and their proper connection were designed and implemented by considering the possibilities of modern computer science together with our previous experiences (**Figure 3.**).

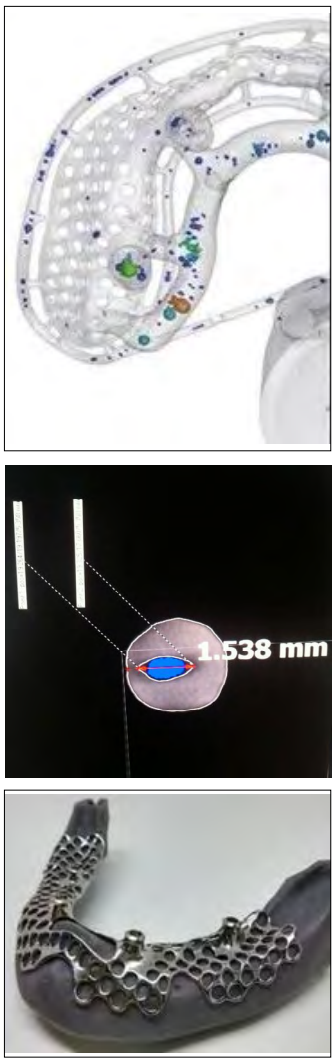

Figure 2. *Revealed material continuity defects and void fractions in micro-CT images*

4. Finite element analysis of the frame structure

Finite element analysis utilizes the mathematical model of the physical structure. It contains structural parts, material models, boundary conditions, and all other properties that model physical reality (**Figure 4.**).

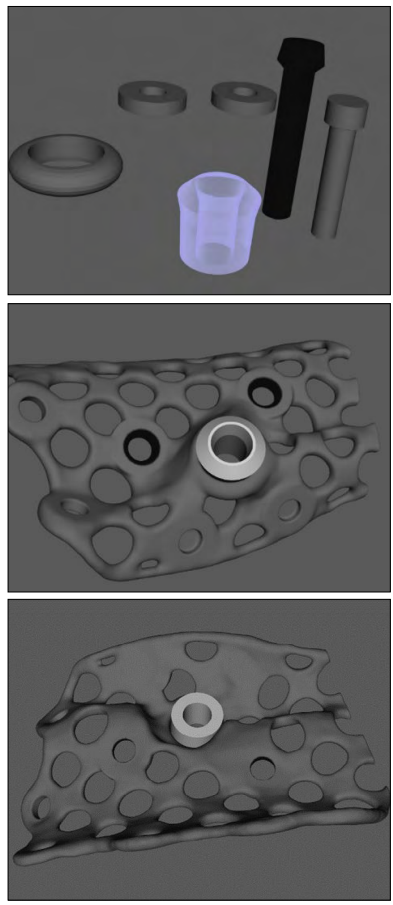

Figure 3. *Virtual joining of designed pillar elements with the frame structure*

Stress distribution of the membrane was examined with finite element analysis in locations where the threaded sleeve, which holds the implant superstructure, is attached with laser micro welding. **Figure 5.** shows the direction of mechanical loads and stress distribution. In this case, an axial occlusal force of 150 N and its horizontal components were determined for implant loading. Hereby, an average of 15 mm interocclusal distance was calculated for cases of bone deficiency.

Finite element analysis provided a great support for determining dimensions of the frame structure. Frame extension, peripheries, minimum material thickness, perforation diameter, consistence, and position were all idealised for a given load.

5. Mechanical testing of welded titanium alloy specimens

The material of structural parts such as frame and threaded sleeve were both titanium alloys. The frame structure, however, was built up with additive manufacturing process from Grade 23 titanium material, while the CNC machined threaded sleeves were made from Grade 5 titanium rods. We had previous practical experiences regarding cast Grade 1 and Grade 5 titanium welding with Grade 1 filler material. Their quality and material homogeneity had been evaluated with micro-CT analysis. These experiences made it necessary for us to test the new welded structure as well.

Additively manufactured Grade 23 titanium test specimens were subjected to structural material testing. Comparative tensile testing was also conducted during which test specimens were cut apart and then joined back together with laser micro welding to retain their original geometry.

Firstly, simple test specimens were used (**Figure 6.**). We observed that the extent of tensile elongation at break can affect the strength of the welded structure itself (**Figure 7.**).

Az eredeti próbatest módosítására azért volt szükség, hogy a szakadási nyúlás mértékét csökkentsük.

The modification of the original test specimen was necessary to minimize tensile elongation at break.

The modified geometry was determined based on this approach (**Figures 8.** and **9.**).

Cut and welded test specimens were created, and the comparative tensile test was repeated (**Figures 10.**, **11.** and **12. ábra**).

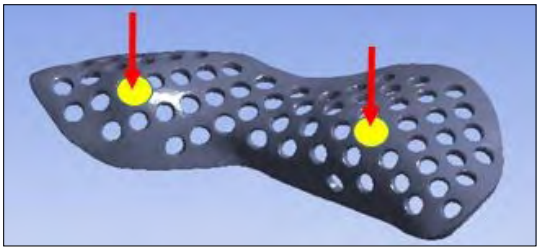

Figure 4. *Pillar positioning on the solid model*

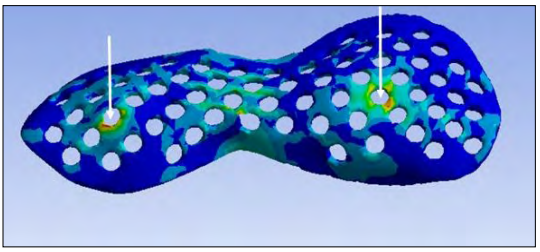

Figure 5. *Stress distribution nearby the placed pillar elements*

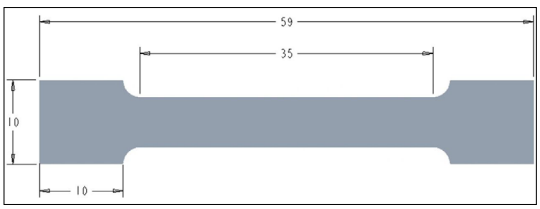

Figure 6. *Original test specimen*

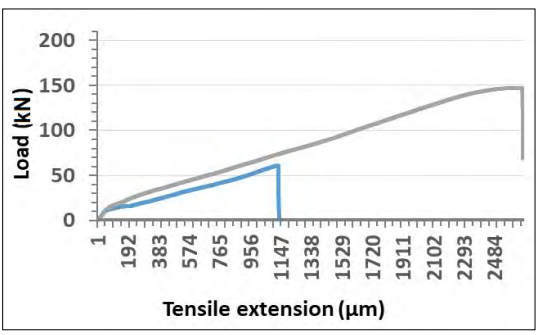

Figure 7. *Force-displacement curve of original test specimens. Grey colour indicates the original, blue indicates the welded test specimens*

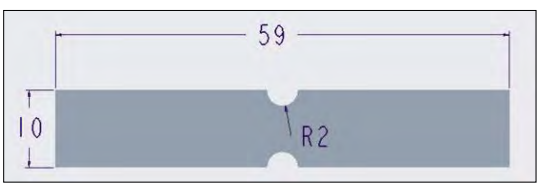

Figure 8. *Modified test specimen*

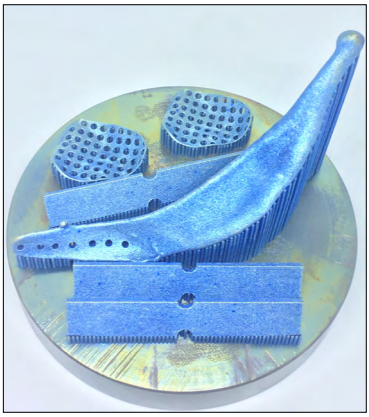

Figure 9. *Additive manufacturing of test specimens*

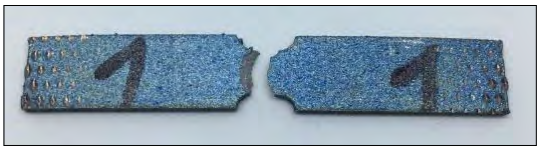

Figure 10. *Split modified test specimen*

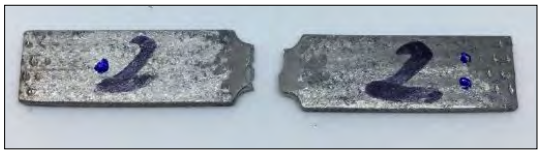

Figure 11. *Split welded and modified test specimen*

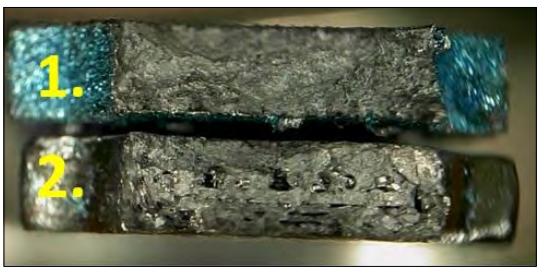

Figure 12. *Fracture surfaces of test specimens: no. 1 is modified and no.2 modified and welded test specimen*

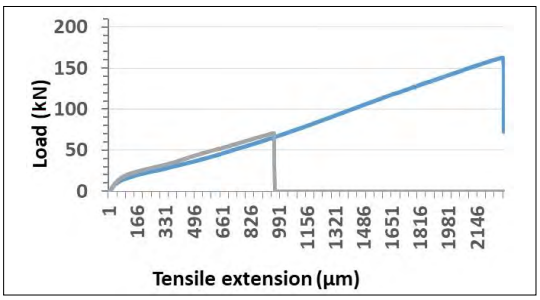

Figure 13. *Force-displacement curve of modified test specimens. Colour blue indicates the original, grey indicates welded test specimen*

Based on results of tensile testing and comparative numerical analysis of stress distributions in frame structures, we conclude that the mechanical strength of the welded joint fulfils the expected physical requirements. According to our calculations, the welded structure can withstand forces twenty times higher than the average axial articulation force (considering 140 N average acting force) (**Figure 13.**).

6. Base plate created with additive manufacturing

Precision casting could be substituted due to development in manufacturing technology and available machinery. The idea presented itself to create the additively manufactured – Selective Laser Melting (SLM) – base plate together with fixing points in one structure. Machining became complicated because of the relative material brittleness resulting from the heat treatment, which was carried out according to the manufacturer's recommendations, of the printed metal structure (**Figure 14.**). The use of conventional screw taps

Figure 14. *Examples of unsuccessful machining outcomes of one-piece-printed metal structures*

was not possible. Precision post-machining of further implant fitting surfaces was also problematic as accurate fixing and positioning of the workpiece was not accomplishable.

Clear results of our investigation and experiences showed that laser welding is the most precise and cost-effective method to join the 3D-printed base plate with the threaded sleeves, which provide dual-phase fixing. It necessitated the use of virtual elements during product design. They defined the exact location of the sleeves and joint geometry parameters such as groove angles material thicknesses (**Figure 15.** and **Table 1.**).

The 3D-printed metal part went through stress relieving heat treatment for 20 minutes on 600 °C (atmospheric pressure, without protective gas). It was followed by corundum particle blasting on 3-4 bar with a particle size of 50 µm. After manual surface processing, the two ele-

Table 1. *Technical parameters of the additive laser manufacturing unit*

Technical parameters	SISMA mysint100
Effective cylinder volume	dia. 100×100 mm
Max output power	200 W
Laser spot diametre	50 µm
Tipical layer thickness	20-40 µm
Power supply	220–240 V / 50–60 Hz
Max. power absorbed	1,53 kW
Inert protection gas	nitrogen, argon
Inert gas supply	6 mm/2,5–5 bar 35 L/min
Inert gas consumption	<0,3 L/min on 0,5 % O_2
O_2 concentration	0,3 %
Equipment dimensions	1390×777×1600 mm
Equipment weight	650 kg

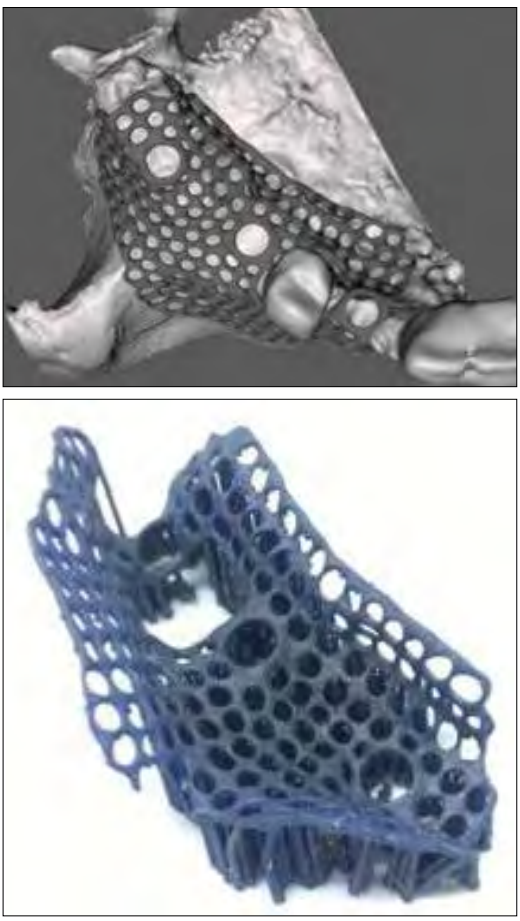

Figure 15. *Base plate created with additive manufacturing (powder bed fusion), and the printed solid part with support structures*

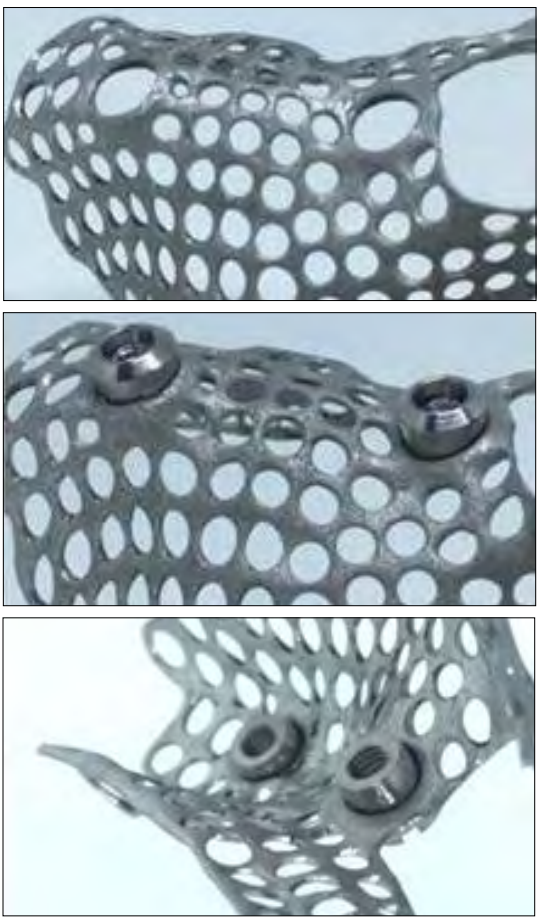

Figure 16. Structural part assembly for welding: joining sleeve components

ments were positioned together (**Figure 16.**) for welding according to the existing virtual design. Simultaneously, complex parallelism check of the fixing elements is necessary. Assembly of structural elements was done on the SLA 3D-printed photopolymer bone surface, which had been generated from DICOM file of the CBCT image.

7. Laser beam welding

Impulse laser welding can join materials with extremely high melting temperature. Heat input takes such a short time that surfaces in the welding zone are heated above the melting temperature before the end of the laser impulse cycle. With the periodicity of the laser impulses and the laser beam scanning, the welded joint is formed. This welding process is the basis of micro laser beam welding. Titanium and titanium alloys can be welded with high penetration depth this way.

Parts to be assembled include a 3D printed base frame (Ti Grade 23, Ti-6Al-4V), filling material (Ti Grade 1, Ø 0,2 mm wire), and the threaded sleeves of the pillars (Ti Grade 5 from turned rolled rod).

Laser welding is implemented in an argon atmosphere and starts with fixing spot welding in order to avoid deformations.

The joining of the workpieces with our cross-sectional design is carried out with filling material (unalloyed, Grade 1) according to the adjusted technical variables of the welding machine (300–320 V / 8.5 ms 5.0 Hz, Focus: between 1–2) after circular symmetric deep penetration welding of the root gap (260–280 V 5–8.5 ms 5.0 Hz focus: between 0 and 2) (**Figure 17.**).

Facing of the deposited layers: 260-290 V 8.5 ms 5.0 Hz, focus between 3-10. Welded joint surface is finished by increasing laser inclination angle and the diameter of the laser spot (**Table 2.**). The last welding step is the placing of the base plate for the threaded sleeve. After welding, the merged part is subjected again to stress relieving heat treatment.

Final finishing (cleansing of the welded joints, facing of wrinkles) of the welded implant plate structure takes place with complex-geometry polishing tools. Despite digital design and manufacturing, the final finishing stage requires a significant amount of manual work. It consists of the micro-particle (50 µm, 1,5 bar) blasting of the dorsal surface, which is followed by acid etching to decrease micro grooves on the surface. The process ends with the mirror finishing of the buccal surface (**Figure 18.**).

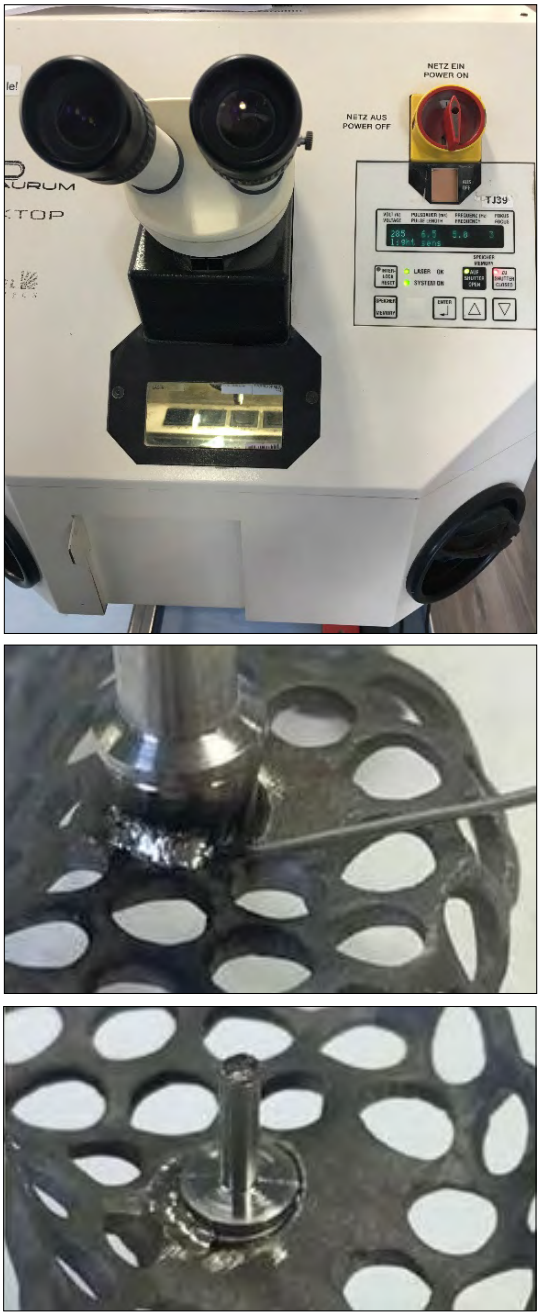

Figure 17. Interface of the laser beam welding unit and the phases of welding

Surface preparation is important at the interface between the implant structure and the mucous membrane and bone tissue, as it influences the osseointegration rate, which increases implant stability. Finally, check assays were conducted on each custom-made implant using micro CT.

Table 2. *Main technical features of our Dentaurum Basel Laser Desktop micro welding unit*

Parametres of laser welding unit	
Laser crystal	Nd: YAG
Wavelength	1064 nm
Max. average power	50 W
Pulse energy	50 J
Pulse peak power	5 kW
Pulse duration	0.5–20 ms
Pulse frequency single pulse	25 Hz
Pulse shape	4 pre-formed pulse shapes
Laser cooling	integrated water-air-heat exchanger
Electrical connection	200–240 V / 50–60 Hz /10 A
Max. power consumption	2,2 kW

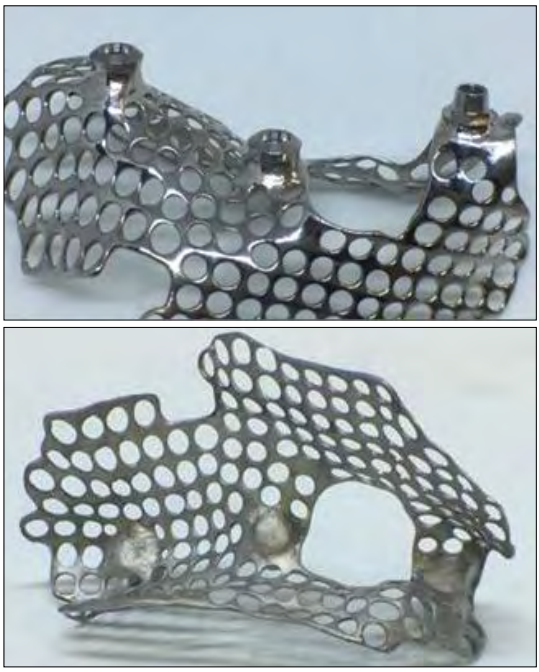

Figure 18. *Joined structure of subperiosteal implant after surface processing*

8. Non-destructive material testing with micro CT

Material homogeneity defects in the welded joint can be analysed during this material testing procedure. These material defects influence mechanical strength, quality, and durability of the welded joint (**Figure 19.**).

Quality standards were determined based on analyses of tensile test specimens made for welded joint evaluation. Welded joint volume of test specimens had to have a homogeneity of 90 % evaluated by micro CT, and the size of the largest void could not exceed 0.05 mm^3. Moreover, its distance from the material surface had to be greater than 0.3 mm.

9. Metallographic analysis of the welded joint of the test specimen

For welding joint quality analysis a trial implant, with a material and manufacturing technology identical to the original implant, was manufactured. A metallographic section was microscopically analysed after acid etching (with a Nikon TS100 microscope) (**Figure 20.**).

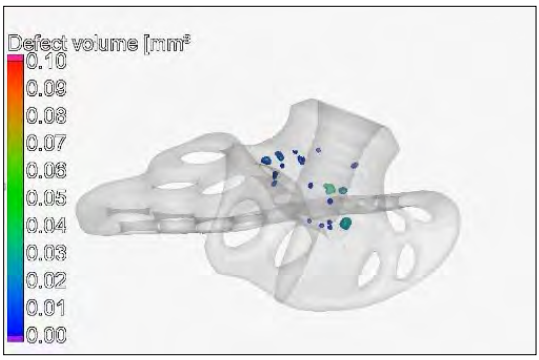

Figure 19. *Micro CT evaluation of the test specimen's welded joint*

Figure 20. *Microscope used for metallographic analysis*

No significant grain coarsening takes place during laser micro welding. The heat affected zone is also narrow. These kinds of welding joints are advantageous from several points of view: homogeneous joint structure with uniform and consistent heat affected zone (**Figure 21.**).

Cut position and metallographic section were chosen to show the largest welding void fractions according to micro CT images. See marked positions in **Figure 22.**

10. Summary

Implantation of the final screw-fixed denture takes place after the completed mucous membrane recovery over the dental implant, and after proper osseointegration titanium frame surrounding bone tissue (**Figure 23.** and **24.**).

Our completely re-thought and manufacturing technologically developed subperiosteal implant with dual-phase fixing points represents a novel technical solution regarding both its material and the complex technology of its geometric design. Separable, dual-phase fixing locations allow isolated healing under skin level. Subgingival mucous surface irritation during surgical wound closure and after healing is reduced by the minimising of welded sleeve height. It helps patients for whom conventional cylindrical dental implants are not an option due to the patient's insufficient bone volume resulting from tooth loss and bone resorption.

Acknowledgement

We would like to thank for the support provided within "Internationalization, initiatives to establish a new source of researchers and graduates and development of knowledge and technological transfer as instrument of intelligent specializations at Széchenyi István University" project.

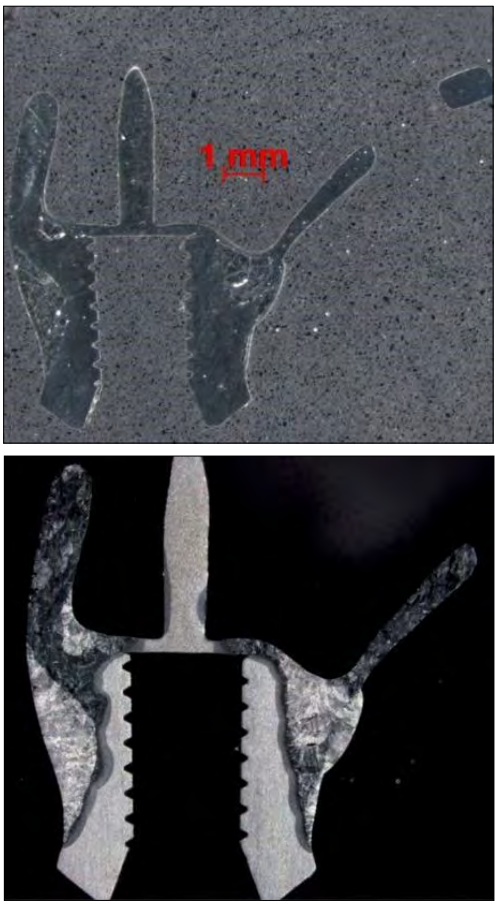

Figure 21. *Structural and sectional photos the welded titanium structure*

Figure 22. *Sectional images of the welded titanium frame structure with marked void fractions*

Figure 23. *Finished implant frames together with denture model before sterilising*

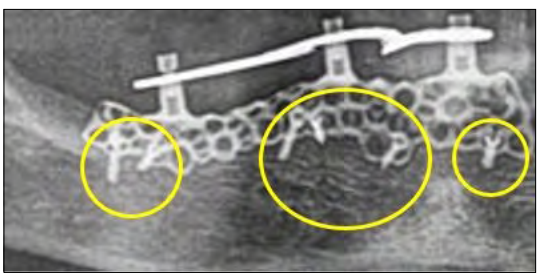

Figure 24. *X-ray image of implanted custom-made subperiosteal implant with fixing screws*

References

[1] Malinov S., Sha W.: *Application of artificial neural networks for modeling correlations in titanium alloy.* Materials Science and Engineering A, 41/1-2. (2010) 140–146. https://doi.org/10.1016/j.msea.2003.09.029

[2] Shrivastava S.: *Medical Device Materials, Anaheim CA*. In: Proceedings of the Materials and Processes for Medical Devices Conference, 2003. 417. https://www.asminternational.org/documents/10192/1849770/06974g_frontmatter.pdf

[3] Xie J., Safarevich S.: *Laser materials porcessing for medical devices.* In: Shrivastava S. (ed.): Proceedings of the Materials and Processes for Medical Devices Conference, Anaheim, CA, ASM International. 2003. 25–30.

[4] Saresh N., Gopalakrishna Pillai M., Mathew J.: *Investigations into the effects of electron beam welding on thick Ti-6Al-4V titanium alloy*. Journal of Materials Technology, 192–193. (2007) 83–88. https://doi.org/10.1016/j.jmatprotec.2007.04.048

[5] *Welding Handbook. Weldings Processes*. vol. 2., American Welding Society, Miami, FL, 1988. 695–697.

[6] *Welding Handbook. Metals and Their Weldability*, vol. 4., American Welding Society, Miami, FL, 1982. 447–449.

[7] Gupta B., Krishna V. G.: *Aerospace Materials*, vol. 1., S-Chand and Company Ltd., New Delhi, India, 1996.

[8] Kelly S. M, Kapmpe S. L.: *Microstructural evolution in laser-deposited multilayer Ti-6Al-4V builds.* PartII. Thermalmodeling. Metallurgicaland Materials Transactions, A 35/6. (2004) 1869–1879. https://doi.org/10.1007/s11661-004-0095-7

[9] Qian L., Mei K., Liang J., Wu X.: *Influence of position and laser power on thermal history and microstructure of direct laser fabricated Ti-6Al-4V samples*. Materials Science and Technology, 21/5. (2005) 597–605. https://doi.org/10.1179/174328405X21003

[10] Dinda G. p., Song L., Mazumder J.: *Fabrication of Ti-6Al-4V scaffolds by direct metal deposition.* Metallurgical and Material Transactions A - Physical Metallurgy and Materials Science, 39/12. (2008) 2914–2922. https://doi:10.1007/s11661-008-9634-y

[11] Nowotny S., Scharek S., Beyer E., Richter K. H.: *Laser beam build-up welding: precision in repair, surface cladding, and direct 3D metal deposition.* Journal of Thermal Spray Technology, 16/3. (2007) 344–348. https://doi:10.1007/s11666-007-9028-5

[12] Taminger K. M., Hafley R. A.: *Electron beam freeform fabrication for cost effective near-net shape manufacturing.* In: NATO/RTO AVT-139 specialists meeting on cost effective manufacture via net shape processing,

Amsterdam (The Netherlands): NATO, (2006) https://ntrs.nasa.gov/archive/nasa/casi.ntrs.nasa.gov/20080013538.pdf

[13] Katou M., Oh J., Miyamoto Y., Matsuura K., Koduh M.: *Freeform fabrication of titanium metal and intermetallic alloys by three-dimensional micro welding*. Materials and Design, 28/7. (2008) 2093–2098. https://doi.org/10.1016/j.matdes.2006.05.024

[14] Clark D., Bache M., Whittaker M.: *Shaped metal deposition of a nickel alloy for aero engine applications*. Journal of Materials Processing Technology, 203/1-3. (2008) 439–448. https://doi.org/10.1016/j.jmatprotec.2007.10.051

[15] Baufeld B., Van der Biest O., Gault R.: *Additive manufacturing of Ti-6Al-4V components by shaped metal deposition: Microstructure and mechanical properties*. Materials and Design, 31/1. (2010) 106–111. https://doi.org/10.1016/j.matdes.2009.11.032

[16] Barreda J. L., Santamaram F., Azpiroz X., Irisarri A. M., Varona J. M.: *Electron beam welded high thickness Ti-6Al-4V plates using filler metal of similar and different composition to the base plate*. Vacuum 62/2–3. (2001) 143–150. https://doi.org/10.1016/S0042-207X(00)00454-1

[17] Baeslack W. A., Becker D. W., Froes F. H.: *Advances in titanium alloy welding metallurgy*. Journal of Metals, 36/5. (1984) 46–82. https://slideheaven.com/queue/advances-in-titanium-alloy-welding-metallurgy.html

[18] Balasubramanian M., Jayabalan V., Balasubramanian V.: *Developing mathematical models to predict tensile properties of pulsed current gas tungsten arc welded Ti-6Al-4V alloy*. Materials and Design, 29/1. (2008) 92–97. https://doi.org/10.1016/j.matdes.2006.12.001

[19] Li X., Xie J., Zhou Y.: *Effects of oxygen contamination in the argon shielding gas in laser welding of commercially pure titanium thin sheet*. Journal of Materials Science, 40/13. (2005) 3437–3443. http://www.camj.uwaterloo.ca/pdf/Zhou/JMS-2005%20Li.pdf

[20] Brandl E., Baufeld B., Leyens C., Gault R.: *Additive manufactured Ti-6Al-4V using welding wire: comparison of laser and arc beam deposition and evaluation with respect to aerospace material specifications*. ScienceDirect – Physics Prodedia, 5/1. (2010) 595–606. https://doi.org/10.1016/j.phpro.2010.08.087

Acta Materialia Transylvanica 2/1. (2019) 43–48.
https://doi.org/10.33924/amt-2019-01-07
Hungarian: https://doi.org/10.33923/amt-2019-01-07
https://eda.eme.ro/handle/10598/31427

Investigation of Imperfections Formed at the Ultrasonic Welding of Copper Sheets

Tünde Anna KOVÁCS

Óbuda University, Donát Bánki Faculty of Mechanical and Safety Engineering, Department of Materials Technology, Budapest, Hungary, kovacs.tunde@bgk.uni-obuda.hu

Abstract
Ultrasonic welding is a very useful and simple welding process. It is suitable for establishing a joint between thin sheets and dissimilar metals with short preparation and finish work time [1]. Some welding defects were detected due to less than optimal ultrasonic welding parameters. These defects were ruptures, surface colour change and unacceptable deformations. This article aims to identify these failures and their causes.

Keywords: *copper, ultrasonic welding, weld imperfections, heat affected zone.*

1. Introduction

The thin sheet welding process specification is an industrial requirement. The applicable processes in the joining of thin metal sheets are brazing, soldering, adhesive bonding and welding. To maintain good conductivity of the metal it is necessary to establish a metalloid joint by welding. It is important to assure the consistency of the welded joint, heat affected zone and the base material microstructure, chemical composition and mechanical properties. In the case of welding defects in the joint, it is necessary to inspect the process specification and modify the technology parameters or change the process.

Ultrasonic welding is advantageous in the electronics industry because in the joining process the generated heat is small and does not need any filler metal. The established joint is metallic with suitable mechanical properties and without significant deformation.

2. Theoretical background

2.1. Fatigue, fatigue strength

The cracking and the fracture of metals is usually explained as being due to fatigue. In the case of nonferrous and non-titanium base metal alloys (Al, Mg, Cu) a useful mechanical property is the fatigue strength. The fatigue strength is a strength level, which under definite repetition number (107) is suitable for sizing (**Figure 1.**) shows the fatigue strength curve without an asymptote. Fatigue strength depends on the grain size, corrosion, frequency and vacuum attendance, the middle stress, plasticity, surface roughness, microstructure (crack sensitivy) and the temperature **[3]**. The temperature increase causes a decrease in the fatigue strength.

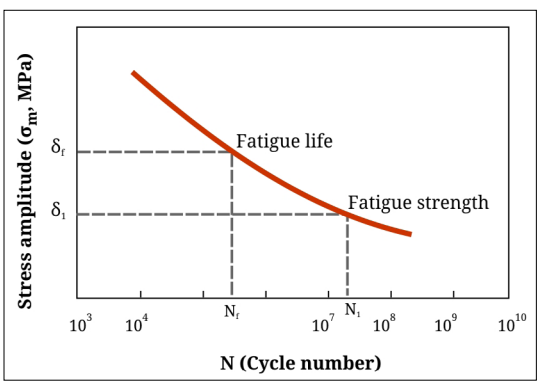

Figure 1. *Fatigue strength* **[2]**

2.2. Theoretical background of ultrasonic welding

Ultrasonic welding is not a new welding process, it was introduced many years ago, yet even now the material science background of this bonding process is not well understood. Ultrasonic welding is a solid state welding process, one which is useful for joining thin sheets. The joint is established by pressure and high frequency ultrasound.

The theory of the ultrasound effect for the dislocation movement is known in cold metal working technology.

The basis of ultrasonic welding is the plasticity increasing phenomenon affected by ultrasound vibration because the welded joint is formed by plastic deformation [4–6].

Figure 3. shows the dislocation intensity and microhardness changes as a function of ultrasound actiontime. This theory is one of the reasons for the change in mechanical properties.

The established heat depends on the material's physical properties and the welding parameters. In the case of the aluminium and copper sheets, a high level of heat increase was detected. The welding process is shown in Figure 4.).

It was verified by measurement that during the copper ultrasonic welding, the temperature of the joint reached 500 °C. This temperature is higher than the recrystallization temperature. The join is supported by plastic deformation. Figure 5. shows the imprint of the hammer on the joint surface, and Figure 6. shows the cross section of

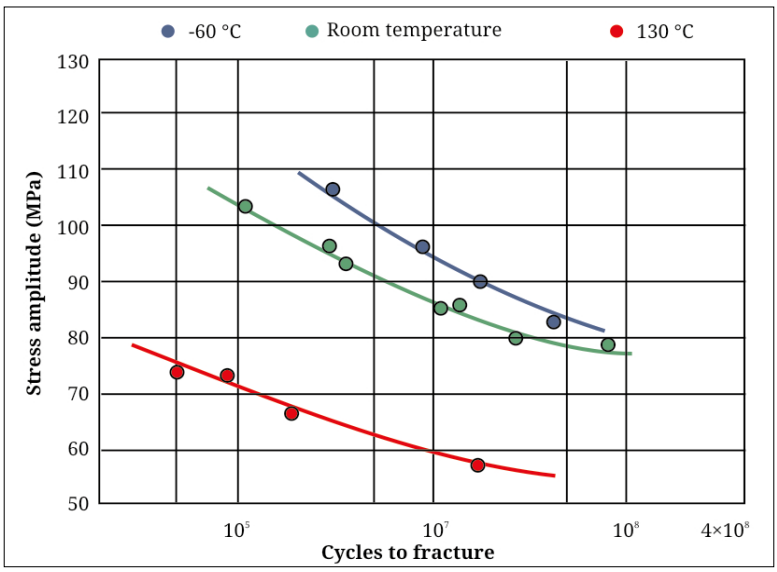

Figure 2. *The pure annealed copper fatigue strength function* [2]

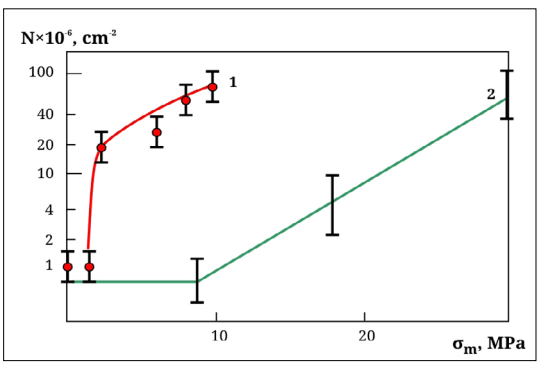

Figure 3. *The dislocation intensity as a function of ultrasound stress amplitude(1) Al 20 °C, and Cu 45 °C* [7]

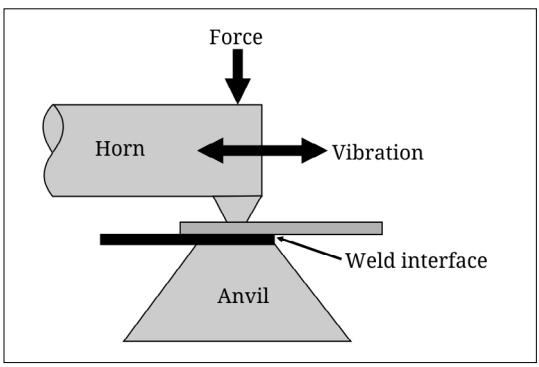

Figure 4. *Ultrasonic welding* [1]

the welded joint. The grains are deformed and the grain sizes are different.

In the case of solid state welding the dislocation movement is very important, because this phenomenon supports the plastic deformation which is needed to establish the welded joint. The recrystallization phenomenon produced in the bond by ultrasound and friction generates heat. The grain size in the welded join can change with the mechanical properties. The grain size and the mechanical properties can change in the welded joint.

3. Investigations of the ultrasonic welded copper sheets

3.1. Investigated material

Copper has always been a very popular metal, being used in the ancient times. It has good plasticity (elongation at rupture A = 50 %), good heat and electric conductivity and good corrosion resistance. Its melting temperature (1084 ºC) is lower than steels and higher than aluminium. In industrial practice the brazing process is suitable for joining copper sheets because for resistance spot welding special electrodes and work cycle are required, for fusion welding a high temperature is needed. The reflexion and the very good heat conductivity of copper is problematic in the case of low heat input processes such as laser welding [6–7].

Even though copper is a ubiquitously used industrial metal, the strength is low (annealed: R_m= 240 MPa, $R_{p0.2}$= 70 MPa, hardness 30 HB). Annealed state copper fatigue strength 62-75 MPa [2]. Cold worked copper strength (380-415 MPa), with alloys and heat treatment is increasable, as against other advantages like electrical conductivity decrease. Applicable in the electrical industry.

Pure copper (CW024A) sheets were used for the investigations, being a common metal for electrical industry applications. Its microstructure is shown in Figure 7. We used annealed copper (99,90 %) sheets with 0,5 mm thickness, the sample size was: 15 mm wide, 60 mm length (Standard sign: Cu-DHP, EN 1172).

3.2. The used welding device

For ultrasonic welding the frequency was constant f = 20 000 Hz ± 50 Hz. The used welding device was the Branson Ultraweld L20. Other parameters were the time of the vibration t (s), and

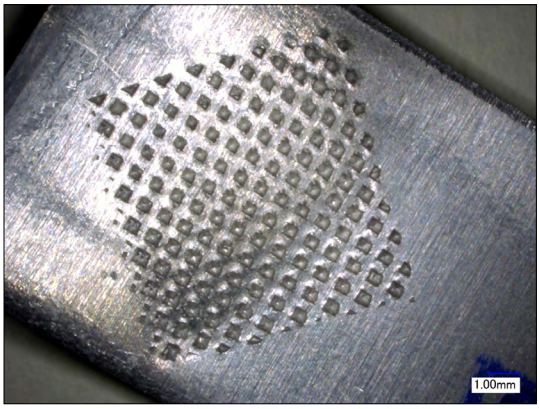

Figure 5. *Ultrasonic welded joint surface*

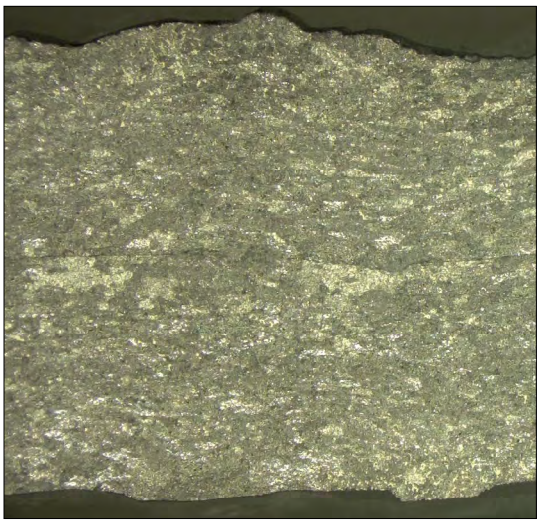

Figure 6. *Cross section of the joint (aluminium sample)*

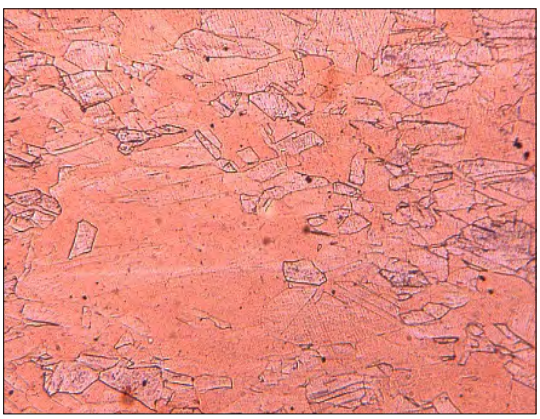

Figure 7. *Copper microstructure linear magnification 50x, etched by ammonium hydroxide/hydrogen peroxide* [7]

the vibration amplitude A (μm), the pressure normal force F (N), the power P (W) from (1) equation, where the f (Hz) is the frequency:

$$P = F \cdot A \cdot f \quad (1)$$

The anvil size was (12,5 mm × 12,5 mm square) and the sonotrode size was (14,5 mm × 12,5 mm rectangle) the contact area was different. The cooling by air is optional during the welding process.

The welding parameters are readable from the menu system. The energy mode limits the ultrasound effect time to maximal energy. In the case of the time mode the user determines the ultrasound effect duration. The work cycle of the welding process is shown in **Figure 8.**

In the welding cycle, the trigger pressure takes the sample on the position before welding the welder pressure and the ultrasound affect together establish the welded joint (**Figure 4.**). The steel anvil and the hammer surfaces are rough to inhibit them joining with the sample **[8–9]**.

3.3. Investigation of imperfections

Test welding was carried out using different parameters. In the time mode, the welding time is adjustable. Some pretesting was parformed to determine how the parameters affect intensity of the deformation and joint strength.

The experimental results show that the vibration amplitude and time effects are critical in the joint quality **[10]**. **Figure 9** shows an unsuitable joint. The joint didn't established and in the cross section some cracks were found.

During the welding process the temperature of the samples can increasing high, cause melting in the joint. The **Figure 10.** shows the melting in the joint cross section. In the case of the ultrasound welded joining this is an unsuitable joint.

Some parameters collectively can affect cracking and rupture, as **Figure 11.** shows.

The cracks typically proceed from the border of the joint. **Figure 11.** shows the process affected rupture.

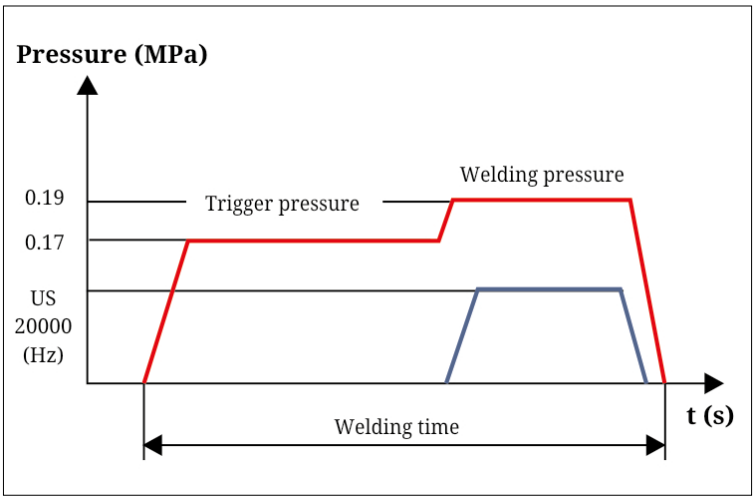

Figure 8. *Ultrasonic welding cycle*

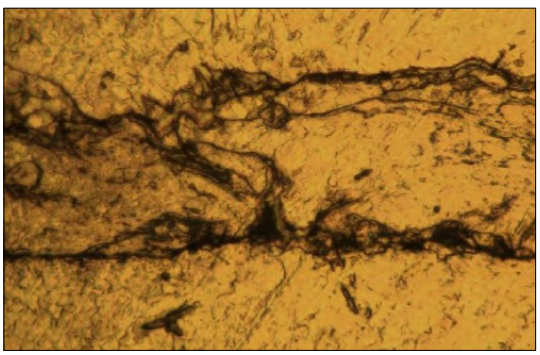

Figure 9. *Ultrasonic welded copper joint*

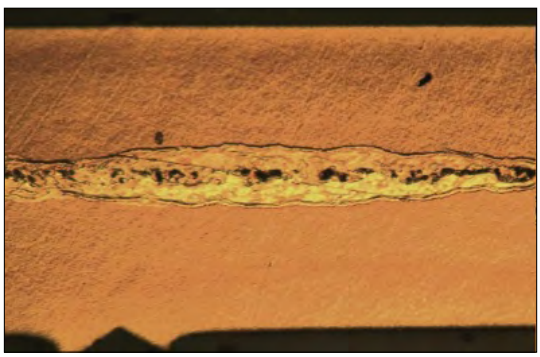

Figure 10. *Melted zone in the joint cross section*

The required tests in the case of the ultrasonic welding are the visual test and the tensile test to determine the maximal force. Also required is the investigation of rupture process.

The welding parameters used for the experiments are shown in **Table 1.** The trigger pressure (T.P.), and the welding pressure (W.P.) were constant in the experiments (0,17 MPa).

4. Conclusions

The results of the experiments are summarized in the **Tabel 1**. On the basis of the experimental results, it can be concluded that, as function of the welding time, we can detect imperfections (deformation, cracking, changing of the sample color, melting in the joint).

In each case the cracks and crack propagation investigated under long ultrasound effect time. The copper fatigue life time decreases under ultrasound effects.

Surface burning was detected under vibration amplitude and with long welding time. It was concluded also that under high vibration amplitude and short welding time the joint was not suitable.

As a function of the welding time and vibration amplitude, the nascent temperature is determinable, to find this equation requires more experimental results.

Future plan

We wish to investigate, by experiment, the decrease in copper fatigue life time due to the effects of ultrasound vibration.

More experimental results for the relationship between microstructural changes and resulting mechanical property changes are also the aim of future work.

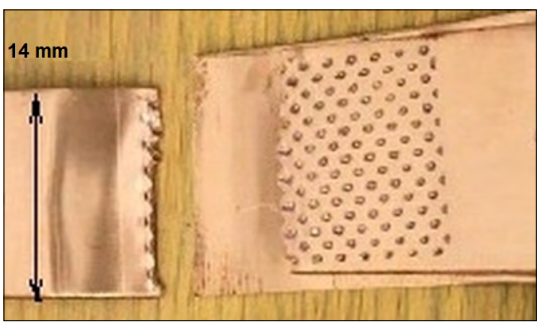

Figure 11. *Cracking in the joint*

Table 1. *The used parameters where; A amplitude (μm), t welding time (s)*

Number	A (μm)	t (s)	Joint, remark
1	60	0,14	Without bonding
	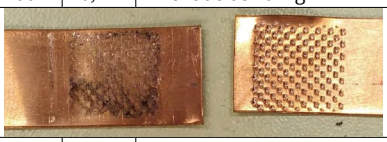		
2	40	1	Cracked and burned
	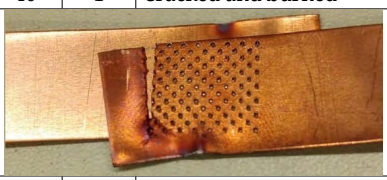		
3	40	0,5	Suitable
	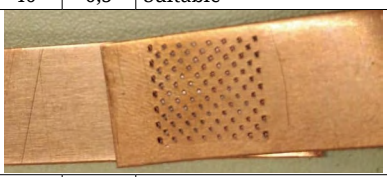		
4	40	0,7	Unsuitable deformation, burned
			
5	40	0,8	Deformation and cracking
	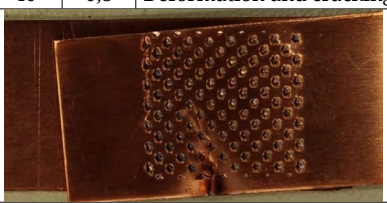		
6	50	0,9	Cracked, burned
	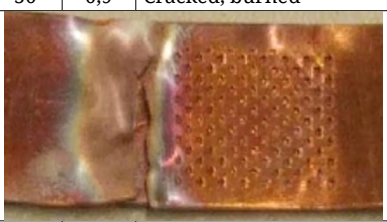		
7	42	3	Colour changing, cracking
			

Acknowledgement

The author wishes to thank Gergely Alvin and Meruyert Rakhimzhan for their assistance in the experiments.

The authors acknowledge the financial support of this work by the Hungarian State and the European Union under the EFOP-3.6.1-16-2016-00010 project.

References

[1] Bagyinszky Gy., Bitay E.: *Ultrahangos hegesztés alkalmazástechnikai jellemzői.* In: A XXIII. Fiatal műszakiak tudományos ülésszak előadásai. Proceedings of the 23th international scientific conference of youngth engineers, Kolozsvár/Cluj, Románia, Műszaki Tudományos Közlemények 7. (2018) 31–34. http://eda.eme.ro/handle/10598/30312

[2] Haikkinen S.: *Fatigue of Metals, Copper Alloys*, 2003. http://clic-meeting.web.cern.ch/clic-meeting/2003/06_26sh.pdf

[3] University of Ljubljana: *ESDEP oktatási segédlet.* 2018. (accessed: 2018. 03. 22.) http://fgg-web.fgg.uni-lj.si/~/pmoze/esdep/master/wg12/l0200.htm

[4] Wu X et al.: *Microstructure, welding mechanism, and failure of Al/Cu ultrasonic welds.* Journal of Manufacturing Processes 20. (2015) https://doi.org/10.1016/j.jmapro.2015.06.002

[5] Astashev V. K.,· Babitsky V. I.: *Ultrasonic Processes and Machines, Dynamics, Control and Applications*. Springer-Verlag, Berlin–Heidelberg, 2007. 33–45.

[6] Abramov O. V.: *High-Intensity Ultrasonics: Theory and Industrial Applications*. 1st Edition, CRC Press Published 1999. Januar 18,

[7] Bagyinszki Gy., Bitay E.: *Hegesztéstechnika II. - Berendezések és mérések*. Műszaki Tudományos Füzetek 10., EME, Kolozsvár/Cluj, 2010. 286. http://eda.eme.ro/handle/10598/15438

[8] Langford G.: *Microstructures*. Massachusetts Institute of Technology, Cambridge, MA, Non Ferrous Alloys 1966. https://www.georgesbasement.com/Microstructures/NonFerrousAlloys/Lesson-1/Specimen01.htm

[9] Bagyinszki Gy., Bitay E.: *Hegesztéstechnika I. - Eljárások és gépesítés*. Műszaki Tudományos Füzetek 9., EME Kolozsvár/Cluj, 2010. 288. http://eda.eme.ro/handle/10598/15437

[10] Szilágyi M., Kovács T.: *Thin aluminium sheets ultrasonic welding.* Hegesztéstechnika, Budapest, 2016.

[11] Szilágyi M., Kovács T.: *Ultrasonic Welding process in case of aluminium sheets*. In: Proceedings of 8th International Engineering Symposium at Bánki, Budapest, 55. (2016). http://bgk.uni-obuda.hu/iesb/2016/publication/55.pdf

Acta Materialia Transylvanica 2/1. (2019) 49–54.
https://doi.org/10.33924/amt-2019-01-08
Hungarian: https://doi.org/10.33923/amt-2019-01-08
https://eda.eme.ro/handle/10598/31428

Machinability of Ni-based Superalloys by Indexable End Mills

Krisztián KUN,[1] János KODÁCSY,[2] Dániel VACZKÓ,[3] Zsolt Ferenc KOVÁCS[4]

John von Neumann University, GAMF, Dep. of Vehicle Technology, Kecskemét, Hungary

[1] *kun.krisztian@gamf.uni-neumann.hu*

[2] *kodacsy.janos@gamf.uni-neumann.hu*

[3] *vaczko.daniel@gamf.uni-neumann.hu*

[4] *kovacs.zsolt@gamf.uni-neumann.hu*

Abstract

The subject of this research is the machining of Ni-based super alloys using indexable end mills. The cutting ability of these materials is known to be difficult, even challenging with modern tools, so our goal is to create an efficient technology recommendation on an experimental basis. To this end, we have developed an experimental design from which results are used to determine the optimal technological parameters. This research took place at John Von Neumann University, Department of Vehicle Technology of GAMF Faculty.

Keywords*: Ni-based super alloy, built-up edge, tool wear.*

1. Introduction

In the automotive industry, especially in aerospace and aerospace industries, the use of Ni-based super alloys is becoming increasingly widespread. Today's modern aircraft are driven by one of our most advanced energy conversion systems; the gas turbine, but these are also used in our power plants. The gas temperature at the turbine inlet can reach 1650 ° C for high-performance jet engines. The turbine blades have to withstand speeds up to 10,000rpm at high temperature. Nowadays, turbine blades, which are exposed to high temperatures in turbines are made of nickel alloys, also called nickel-based super alloys [1]. The advantageous properties of these alloys are high strength, poor thermal conductivity, and paramagnetism. A further advantage is that they retain their strength and resist corrosion at extremely high temperatures. The parts they are made of are often machined, (even though they can be classified as difficult-to-cut materials) and they present a challenge even with modern machining tools. Typically, intensive tool wear and chip breaking are the biggest problems. During the experimental work described, we examined the possibilities of milling the GTD-111 nickel super alloy [2–7].

1.1. Applied materials and tools used in the experiments

Choosing the right tools requires careful attention and expertise in each case. With a good decision, we can increase the safety, raise our productivity and reduce cycle times [8]. Numerous methods are suitable for machining Ni super alloy. It's a fact that we can use EDM [9], but its cycle time is long, so research is being done to explore alternative options [10] but its cycle time is long, so research is being done to explore alternative options [11]. In addition to the tool materials, the machining strategy used for cutting can also be an important factor [12, 13].

1.1.1. The material used in the experiment

The GTD-111 investigated in the research is a special Ni-based super alloy produced by vacuum casting. Table 1. shows the chemical composition of the material. [14]

In terms of its cutting ability, the nickel super alloys are one of the most difficult to cut materials.

Table 1. *The chemical composition of the GTD-111* [14]

Addition (GTD-111)	Percentage (%)
Ni	62.37
C	0.08
Cr	13.7
Co	9
Al	2.8
Ti	4.7
W	3.5
Mo	1.4
Ta	2.4
B	0.05

It is characterized by poor thermal conductivity. This is critical, because ideally the separated material (chips) carries most heat. Furthermore, it requires a very stable and powerful machine tool to manufacture, because of the high cutting force. The mechanical and physical properties that are important for cutting the GTD-111 Ni-based material are shown in **Table 2.** .

Table 2. *Mechanical and physical properties of GTD-111* [14]

Tensile strength, R_m (MPa)	1310
Strain, A_5 (%)	5
Contraction, Z (%)	5
Hardness	HRC 41,4
Thermal conductivity at 20 °C, λ (W/(m·K))	12,56

1.1.2. Considerations of the tool- and the insert selection

The indexable milling tools consist of three main parts: the tool body, the insert and the insert's coating. First of all, the coating of the insert was selected for the material from TaeguTec® tool manufacturer. For this purpose, a coating selection application is available in which all TaeguTec® coatings are ranked. These are arrange in the table shown in **Figure 1.**, based on their toughness and hardness, from bottom to top. In our case, the GTD-111 is a Ni-based superalloy, which belongs to the group S, which is indicated by the brown color in the table.

Based on this guide, the following coatings are available: TT9080, TT9030, TT8080 and TT8020. All four optional coating qualities are Physical Vault Deposition (PVD) coatings, the difference being the quality of the coating layers, and the field of applications. The manufacturer does not manufacture all insert geometry with every kind of coating. The next step was to select the possible tools and inserts. Our experiment requires Ø20 mm corner mill with Weldon clamping, and we had to choose an insert capable of a 3 mm depth of cut. When selecting the tool, the insert geometry used in practice was taken into account. The 0-degree back rack angle was chosen, since with this property the inserts are much more stable and have a longer cutting edge. Based on this information, the 4NKT 060308R-ML and 6NKU 040308R-M inserts were selected from the catalogue (**Figure 2.**).

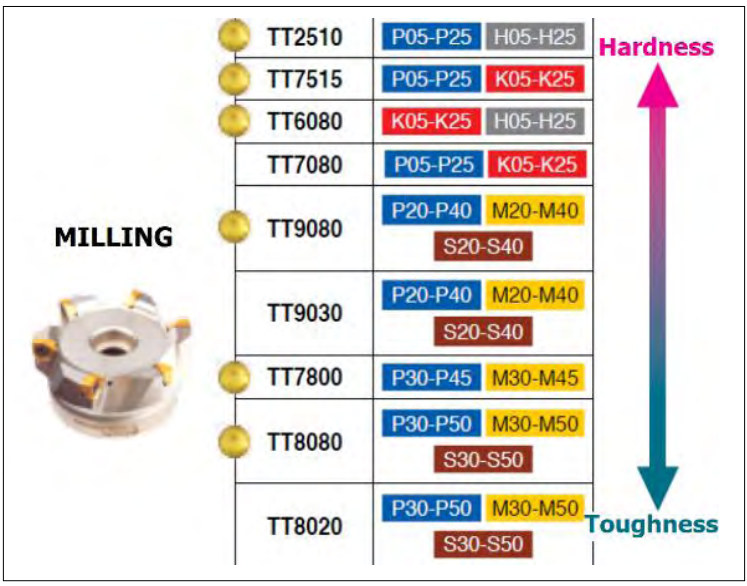

Figure 1. *TaeguTec® coating selection application* [15]

After selecting the inserts, two types of coatings were chosen for them, which differ greatly in their properties. We chose TT9080 and TT8080 quality coatings.

Since our objective was to test the tools while roughing, we chose the TT8080 coating as recommended by the catalogue. Since we planned to use tools with the same number of teeth for each geometry, we chose the 3-toothed cutter. They are marked 4N TE90-320-W20-06, which is a milling tool for the 4NKT 060308R-ML insert, and 6N TE90-320-W20-04, which is for the 6NKU 040308R-M insert (**Figure 3.**).

During the experiments, the tools were named as „A" and „B" tools. The „A" tool had the 4NKT 060308R-ML insert and the associated 6N TE90-320-W20-06 milling tool body, while the „B" tool had the 6NKU 040308RM insert with the 6N TE90-320-W20-04 milling tool body.

2. The experimental design

We used the Taguchi method to perform the experiments, which was designed by the Minitab17 software. This experimental design method helps to find the most defining factors and their possible combinations of experimental results and their effect on the experimental results. It helps to find the right combination of factors for optimal results. Levels for milling factors, including the levels of Cutting speed (v_c) and feed per tooth (f_z), are given based on the TaeguTec® catalog.

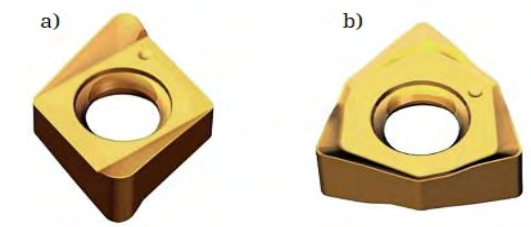

Figure 2. *a) 4NKT 060308R-ML and b) 6NKU 040308R-M inserts* **[16]**

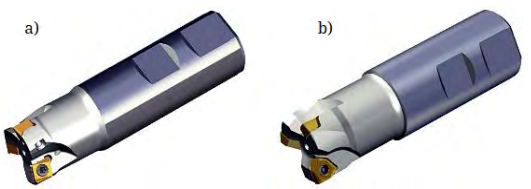

Figure 3. *a) 6N TE90-320-W20-04 and b) 6NKU 040308R-M indexable milling tools* **[16]**

Table 3. *Milling factors and levels for experimental design*

Milling factors		Levels			
		1	2	3	4
A	v_c (m/min)	10	20	30	40
B	f_z (mm/tooth)	0.03	0.07	0.11	0.15
C	Tool	A geometry		B geometry	

2.1. Details of the cutting experiment

The workpiece was fixed in a vice, on the table of the NCT EML850D CNC machining center (**Figure 4.**).

The depth of cut was 3 mm, and repeated eight times with the A and B tools along the 130 mm machining length. Since the maximum depth of 24 mm was too deep for to the geometry of the B tool, and the outlet of the chips would have been more difficult in the 24 mm deep grooves, two grooves were machined with one tool at 12-12 mm depth.

So that the workpiece was clamped enough and the technical parameters were optimally. The parameters of the experiment are summarized in **Table 4.**

Table 4. *The used experimental parameters for GTD-111 material milling by Taguchi-method*

#.	v_c (m/min)	f_z (mm/tooth)	Tool	Mark*
1.	10	0.03	A	AB1
2.	10	0.07	B	BB1
3.	10	0.11	A	AB2
4.	10	0.15	B	BB2
5.	20	0.03	B	BB3
6.	20	0.07	A	AB3
7.	20	0.11	B	BB4
8.	20	0.15	A	AB4
9.	30	0.03	A	AJ1
10.	30	0.07	B	BJ1
11.	30	0.11	A	AJ2
12.	30	0.15	B	BJ2
13.	40	0.03	B	BJ3
14.	40	0.07	A	AJ3
15.	40	0.11	B	BJ4
16.	40	0.15	A	AJ4

*The marking of the grooves:
AB – „A" tool and „B" left-side groove.
BB – „B" tool and „B" left-side groove.
AJ – „A" tool and „J" right-side groove.
BJ – „B" tool and „J" right-side groov

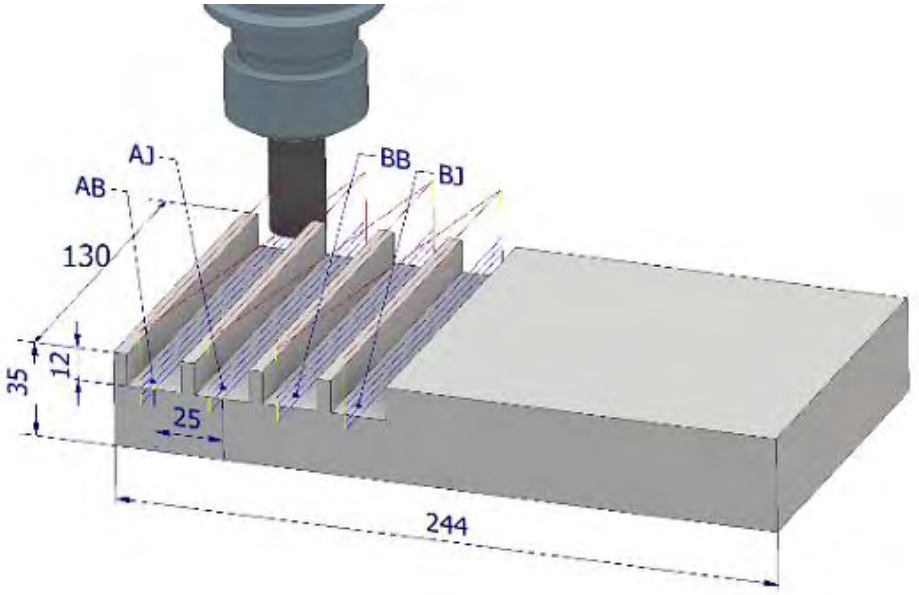

Figure 4. *The experimental method designed in CAD software*

3. Evaluation of results

In order to evaluate the toolware, we have created a list of criteria that we have compiled on the basis of the tests and the expected criteria. The list of criteria is evaluated from 1 to 9. The list is summarized in **Table 5.**, where number 9 is the best, and 1 is the worst result.

The best experimental result is proven by AB1.

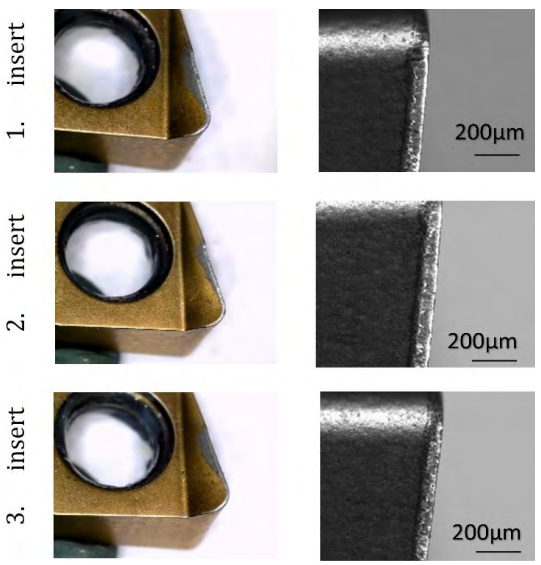

Figure 5. *The inserts of the tool A in the AB1 ex-periment after cutting with microscopic pictures of edges*

Figure 5. shows the microscope image of the three inserts. The tool wear on front and backside of the inserts surface are uniform. On the cutting edge of the inserts, it is clearly visible that the coating is worn, but there are no other damages.

For the sake of clarity, **Table 6.** summarizes the assessment of the technological parameters of the experiment according to the criteria system of **Table 5.**

4. Summary

The cutting effect (v_c) was the greatest impact on the lifetime of the tool during machining, followed by the feed per tooth (f_z). It is noticeable that the effect of tool geometry had a negligible influence on the life span.

The most effective technological variables with the experimental values are:

– cutting speed v_c=10 m/min,
– feed per tooth f_z=0,03 mm/tooth,
– Tool geometry: „A" tool.

The groove made by these parameters is shown in **Figure 6.**

Acknowledgments

We are grateful for the support provided by the EFOP-3.6.1-16-2016-00006 "Development and Expansion of Research Potential at the John von Neumann University". The project is supported by the Hungarian State and the European Union, cofinanced by the European Social Fund, and is part of the Széchenyi 2020 program.

Table 5. *The used inserts evaluated by the created list of criteria*

Rating (value)	Viewpoints
1	It couldn't go through the machining length.
2	It went through the length, but it critically fractured the edges and the inserts were broken.
3	It went through the machining length, but critically fractured the cutting edges of the inserts.
4	It went through the machining length, but it fractured or broke the inserts.
5	It went through the machining length, but the cutting edge- and the flank of the insert were cracked.
6	It went through the machining length, but the cutting edge of the insert was cracked.
7	It went through the machining length, but the flank of the insert was cracked
8	It went through the machining length but the wear was significant.
9	He went through the machining length and the tool wear was even.

Table 6. *Evaluation of the parameters of the experiment according to the criteria system*

#	v_c (m/min)	f_z (mm/tooth)	Tool	Value
AB1	10	0.03	A	**9**
AB2	10	0.11	A	5
AB3	20	0.07	A	6
AB4	20	0.15	A	2
BB1	10	0.07	B	7
BB2	10	0.15	B	4
BB3	20	0.03	B	**8**
BB4	20	0.11	B	5
AJ1	30	0.03	A	**8**
AJ2	30	0.11	A	1
AJ3	40	0.07	A	1
AJ4	40	0.15	A	1
BJ1	30	0.07	B	3
BJ2	30	0.15	B	1
BJ3	40	0.03	B	1
BJ4	40	0.11	B	1

Figure 6. *The AB1 groove's surface with protruding ragged edge (burr)*

References

[1] Sajjadi S. A., Nategh S., Isac M., Zebarjad S. M.: *Tensile deformation mechanisms at different temperatures in the Ni-base superalloy GTD-111*. Journal of Materials Processing Technology 155–156. (2004) 1900–1904. https://doi.org/10.1016/j.jmatprotec.2004.04.273

[2] Bhadeshia H. K. D. H.: *Recrystallisation of practical mechanically alloyed iron-base and nickel-base superalloys.* Materials Science and Engineering A 223. (1997) 64–77. https://doi.org/10.1016/S0921-5093(96)10507-4

[3] Kodácsy J., Viharos Zs. J., Kovács Zs.: *A forgácsolhatóság meghatározásának módszerei Ni-bázisú szuperötvözetek horonymaráskor*. Gépgyártás 55(2). (2015) 125–129.

[4] Zhu D., Zhang X., Ding H.: Tool wear characteristics in machining of nickel-based superalloys. International Journal of Machine Tools & Manufacture 64. (2013) 60–77. https://doi.org/10.1016/j.ijmachtools.2012.08.001

[5] Lendvai János: *Szuperötvözet egykristályok–drágakövek a gázturbinákban.* Fizikai Szemle 2006/10.

[6] Qi Y., Zhang Y., Zhang W., Gao J., Yuan Z., Bu W., Li Y., Guo S.: *Hydrogen storage thermodynamics and kinetics of RE-Mg-Ni-based alloys prepared by mechanical milling*. International Journal of Hydrogen Energy 42/29. (2017) 18473–18483. https://doi.org/10.1016/j.renene.2018.07.134

[7] Ulutan D., Arisoy Y. M., Özel T., Mears L.: *Empirical modeling of residual stress profile in machining nickel based superalloys using the sinusoidal decay function.* Procedia CIRP 13. (2014) 365–370. https://doi.org/10.1016/j.procir.2014.04.062

[8] Mali H. S., Unune D. R.: Machinability of Nickel-Based Superalloys: An Overview. Reference Module in Materials Science and Materials Engineering, (2017). https://doi.org/10.1016/B978-0-12-803581-8.09817-9

[9] Kang X., Tang W.: *Micro-drilling in ceramic-coated Ni-superalloy by electrochemical discharge machining. Journal of Materials* Processing Technology, 255. (2018) 656–664. https://doi.org/10.1016/j.jmatprotec.2018.01.014

[10] Obikawa T., Yamaguchi M., Funai K., Kamata Y., Yamada S.: *Air jet assisted machining of nickel-base superalloy.* International Journal of Machine Tools & Manufacture 61. (2012) 20–26. https://doi.org/10.1016/j.ijmachtools.2012.05.005

[11] Sajgalik M., Czan A., Drbul M., Danis I., Miklos M., Babik O., Joch R.: *Identification of Technological Parameters when Machining Ni-Alloys by Monolithic Ceramic Milling Tool.* Procedia Manufacturing 14. (2017) 51–57. https://doi.org/10.1016/j.promfg.2017.11.006

[12] Pleta A., Mears L.: *Cutting Force Investigation of Trochoidal Milling in Nickel-Based Superalloy.* Procedia Manufacturing 5. (2016) 1348–1356. https://doi.org/10.1016/j.promfg.2016.08.105

[13] Luo M., Lou H., Zhang D., Tang K.: *Improving tool life in multi-axis milling of Ni-based superalloy with ball-end cutter based on the active cutting edge shift strategy.* Journal of Materials Processing Technology 252. (2018) 105–115. https://doi.org/10.1016/j.jmatprotec.2017.09.010

[14] Raznjevic K.: Hőtechnikai táblázatok. Műszaki könyvkiadó, Budapest, 1964.

[15] TaeguTech: *Grade Chart*. (accessed on: 2019. 05.12.) http://www.taegutec.co.kr/Media/DownloadFiles/grade_en.pdf

[16] IMC Companies: *TaeguTec e-Catalogue.* (accessed on: 2019. 05.12.) http://www.imc-companies.com/TaeguTec/ttk-Catalog/Index.aspx

Acta Materialia Transylvanica 2/1. (2019) 55–60.
https://doi.org/10.33924/amt-2019-01-09
Hungarian: https://doi.org/10.33923/amt-2019-01-09
https://eda.eme.ro/handle/10598/31429

Effects of Additive Manufacturing on the Mechanical and Corrosion Properties of Austenic Stainless Steel

János Endre MARÓTI,[1] Dávid Miklós KEMÉNY,[2] Dóra KÁROLY[3]

Budapest University of Technology and Economics, Faculty of Mechanical Engineering, Department of Materials Science and Engineering, Budapest, Hungary

[1] *maroti@eik.bme.hu*

[2] *kemenydavid@edu.bme.hu*

[3] *kdora@eik.bme.hu*

Abstract

Additive manufacturing (AM) offers the possibility to produce complex parts without the design constraints of traditional manufacturing routes. Our aim was to determine different mechanical and corrosion properties of direct metal laser sintered austenitic stainless steel (X2CrNiMo17-12-2) material with tensile test, Charpy impact test, scanning electron microscopy and corrosion test. The measured values were evaluated, and our results compared with literary values, furthermore, we also examined how the printing direction affects the properties.

Keywords*: additive manufacturing, austenitic stainless steel, corrosion, mechanical testing.*

1. Introduction

Products made with additive manufacturing technology (AM) are becoming more popular and widespread, their qualities are getting better, and this meets the demands of quality in the industrial field. Furthermore, it makes possible the production of different geometries or components that would be very expensive or would not have even been possible to produce with other material manufacturing technology just a few years ago. They can now be made to high standards using a wide range of metal powders. Additive manufacturing is no longer solely a prototyping technology, but is now being used for the production of series components for the most demanding applications [1].

We can separate the production process into several phases. First, we need a 3D model that can be designed with a specific CAD (Computer Aided Design) software. This 3D model needs to be converted to STL (Standard Tessellation Language) format, which grants connections between the 3D software and the AM technology. The STL file simulates the model surface with triangles which means if the triangles are smaller than the original geometry of the model it is more accurate [1, 2].

Additive manufacturing has seven major types [3] distinguished by the technology used to build the 3D body. The specimen that we used was made with Direct Metal Laser Sintering (DMLS) technology, where the energy source is the laser beam. In this technology only metal alloy powders are used.

First, the powder of the chosen material is added to the construction platform in one 50-100 µm thick layer. After this, the desired cross section is lighted and heated to near melting temperature until the particles are chemically fused by laser. After the layer is created, the construction platform moves down then the printer adds another layer [1, 2]. The finished product is removed from the powder and is usable after cleaning.

The most important advantage of DMLS is that high geometric accuracy and good surface quality can be achieved without support and surface-treatment. Due to the pre-heating, the product will also have less residual stress. The technology can also be applied to high-strength materials [4, 5].

Previous research has shown that production parameters like laser scanning speed, distance between laser path, linear-, surface- and volu-

metric energy density modification and their relationship to each other [6], as well as porosity of the specimen [7] are most affecting the microstructure and mechanical properties (Young's modulus, Yield strength) of 3D printed specimens.

An interesting question is to examine the 3D printability of various complex geometric medical implants (e.g. coronary artery stents, orthopaedic implants with bone like structure). Thus, the purpose of our research is also to study a commonly used biocompatible material: austenitic stainless steel (316L steel).

2. Materials and methods

Our specimens were X2CrNiMo17-12-2 steel manufactured with an EOS M100 direct metal laser sintering 3D printer (specimen marked with: A) or traditionally manufactured (specimen marked with: H).

2.1. Charpy impact test

Six samples were used for the Charpy impact test with edge lengths of l_1 = 55 mm and l_2 = 10 mm, thickness of h = 2.5 mm, and V-notch of 2 mm deep, with 45° angle. Half of these were additive manufactured, the others were traditionally manufactured from a bulk material.

We also used three standardised specimens with edge lengths of l_1= 55 mm and l_2 = 10 mm, thickness of h = 10 mm, and V-notch of 2 mm deep, with 45° angle. The sample were tested at room temperature by WPN Charpy impact testing device according to [8].

2.2. Tensile test

For the tensile test we used 16 pieces of additive manufactured A marked specimens in total. 10 pieces were with a total length of L_t = 70 mm, original gauge length of L_0 = 27.5 mm, thickness of a_0 = 2 mm, width of b_0 = 2,5 mm and testing length of L_c = 40 mm (hereafter referred to as the long specimen). The other samples for tensile test were a total length of L_t = 37 mm, thickness of a_0 = 2 mm and width of b_0 = 6 mm, without original gauge length (hereafter referred to as the short specimen).

In addition, the direction of construction of the specimen layers was also varied. Some were printed vertically (the support being placed on the smaller side of the workpiece) and some horizontally (the support material was positioned on the larger side of the workpiece). Half of the long specimens were horizontally, half vertically produced. One of the short specimens was printed horizontally, the others were vertically produced. Our results were compared with the manufacturer's data, according to the horizontal test specimens data: R_m = 650 MPa, $R_{p0,2}$ = 535 MPa, A = 35 % and the horizontal test specimens data: R_m = 590 MPa, $R_{p0,2}$ = 490 MPa, A = 45 %[9].

The samples were tested with an MTS 810 universal hydraulic mechanical tester, under a constant loading speed of 3 mm/min at room temperature based on MSZ EN ISO 6892-1 standard [10].

2.3. Corrosion test

For the corrosion test cylindrical samples were 3D printed, with a diameter of d = 15 mm, and a height of h = 6 mm were used. We needed a corrosion cell to do the corrosion test (Figure 1.). The corrosion cell includes: a supersaturated KCl solution calomel electrode, which is the reference electrode; a Pt electrode, which is the counter electrode, a potentiostat with a computer, 250 millilitre glass measuring cup, a digital heating plate and a stand.

For the tests, 0.9 % and 3.5 % NaCl solution was used for the corrosion medium, which simulated the prevailing environment in the body and the seawater. During the measurement with the physiological saline solution, the solution was heated to 37±2 °C, thus approaching the conditions in the body.

At time 0, the current density voltage diagram also called the Tafel curve was measured, and this was repeated 1, 2, 3, 4, and 5 hours later. The tests were performed and evaluated according to ASTM G 102 [11]

Figure 1. *Corrosion measuring arrangement*

Similar measurements were made by L. Absora and his coworkers who measured the corrosion of the X2CrNiMo17-12-2 steel we tested in a 3 % NaCl solution, with a corrosion rate of 0.0071 mm/year [12].

The composition of the samples material were determined by Zeiss EVO M10 scanning electron microscopy (SEM) and the associated Octane elect EDAX (energy dispersive spectroscopy). Pictures were taken from the specimen's surface with accelerating voltage of 20 kV before and after the corrosion tests

3. Results

3.1. Charpy impact test

The linear expansion ($e = x - x_0$, mm), impact energy (KV, J) and the specific impact energy (KCV, J/mm2) of the thin specimens were determined. The results are summarized in Table 1.

The linear expansion, impact energy and specific impact energy for the standardized samples (H10) were also determined. The results can be seen in Table 2.

The fracture surfaces were investigated by scanning electron microscopy (Figure 2.). The fractured, bland-like nature of the surfaces does not differ greatly in the case of the additively manufactured and the conventional specimens, but the presence of potholes due to porosity can be observed in the additively produced samples.

Table 1. *Results of Charpy-impact test for A-marked and H-marked thin specimens*

Specimen		e (mm)	KV (J)	KCV (J/mm²)
Type	No.			
A2,5	1	0.641	18	0.96
A2,5	2	0.917	18	0.96
A2,5	3	0.625	18	0.96
H2,5	1	1.07	27	1.44
H2,5	2	1.07	28	1.49
H2,5	3	1.09	29	1.55

Table 2. *Enlargement (e) and absorbed energies (KV and KCV) of specimen serie H*

Specimen		e (mm)	KV (J)	KCV (J/mm²)
Type	No.			
H10	1	1.4	99	1.32
H10	2	1.2	118	1.57
H10	3	1.1	134	1.65

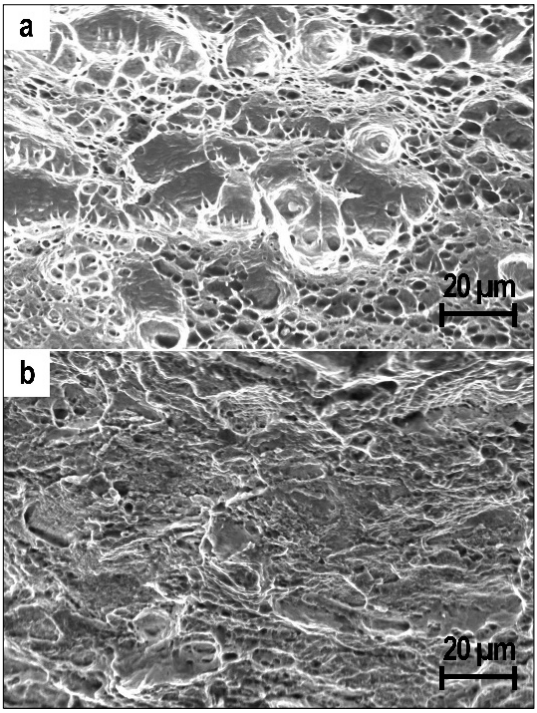

Figure 2. *Scanning electron microscopic image of fracture surfaces after Charpy impact test, additively manufactured (a), conventionally manufactured specimen (b)*

3.2. Tensile test

The tensile ($F - \Delta L$, force-displacement) diagram of one horizonal and one vertical long specimen can be seen in Figure 3. We did not represent the tensile diagram of all the test specimens, because the difference between the two layers of the construction direction is thus more visible.

The average Yield strength ($R_{p0,2}$), elastic modulus (E), tensile strength (R_m), elongation at break (A) and contraction (Z) of the long specimens are shown in Table 3. together with the standard deviation.

The measurement was repeated for the short specimens. For a better illustration of these specimens, the tensile curves of a vertically and horizontally produced workpiece are shown in Figure 4.

Table 3. *Specification of long specimens*

Print direc.	R_{p02} (MPa)	E (GPa)	Rm (MPa)	A (%)	Z (%)
Hor.	520± 43	138± 16	604± 20	23.83±2.25	41.8±7.54
Vert.	460± 17	111± 12	558± 18	26.5±1.9	54±5.2

The average and standard deviation of Yield strength, tensile strength and contraction of short specimens are shown in **Table 4.**

3.3. Corrosion test

Figure 5. shows that during the physiological saline corrosion test at near body temperature (which simulates conditions in the body), the spheres on the surface of the additively produced sample (which are metal splashes due to the laser melting) are released in several places.

The measurements of Tafel curves (corrosion-current density versus potential diagram) obtained in physiological saline are shown in **Figure 6.** From the curves we get the corrosion rate characteristic of the work piece. During the evaluation, the tangents are aligned with the linear section of the Tafel curve, taking into account the equilibrium corrosion potential (E_{corr}). The point of intersection of the tangents gives the current that is entered into the required formulas **[11]** to obtain the corrosion rate.

The surface of the specimens that were in contact with the corrosion medium was determined from the stereomicroscope images. In the case of the specimen used in the physiological saline solution, this is A = 0.88 cm^2, while in the case of seawater saline, the specimen surface area that contacted the corrosion medium is A = 0.875 cm^2. The weight % and atomic % were measured by

Table 4. *Specification of short specimens*

Print direction	R_{p02} (MPa)	R_m (MPa)	Z (%)
Hor.	565	735	26.2
Vert.	600 ± 20	656 ± 19	39.9 ± 2.3

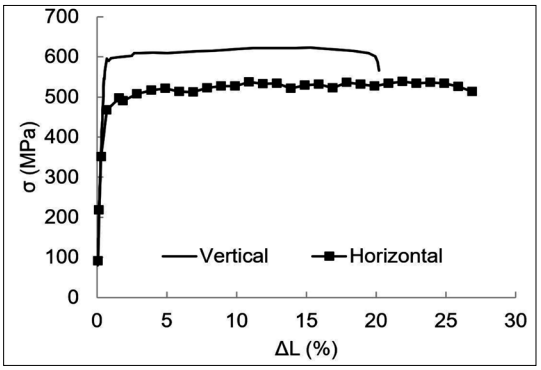

Figure 3. *Tensile test diagram of long specimens*

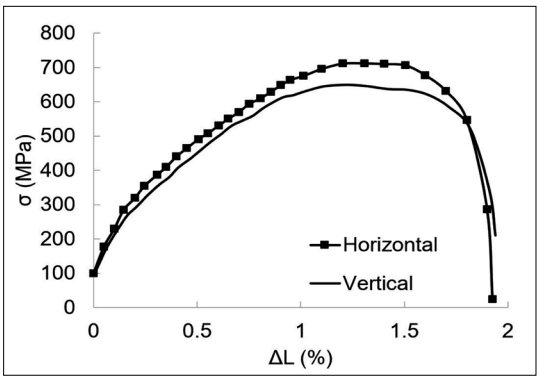

Figure 4. *Tensile test diagram of short specimens*

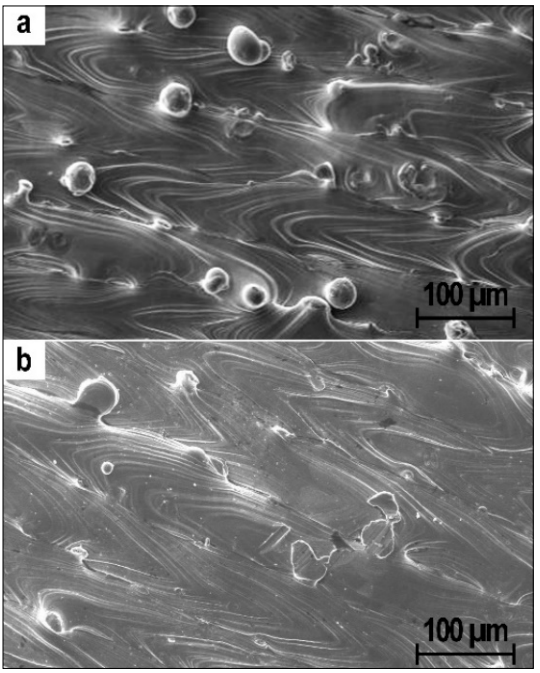

Figure 5. *Surface of additively manufactured specimens before (a) and after (b) corrosion test*

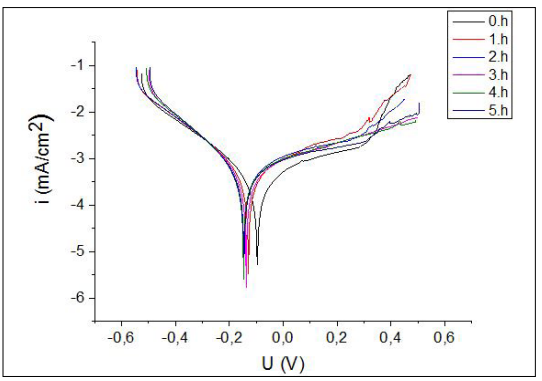

Figure 6. *Tafel curves of additively manufactured samples, 0.9 % NaCl at 0 –5. hours*

SEM-EDS analysis. The material composition of the specimens is summarized in the following table (Table 6.).

Based on these data, the density was ρ= 7.814 g/cm^3, and the equilibrium mass was E_w = 17.164. Corrosion rates (v_{corr}) are listed in Table 7.

Figure 7. shows the temporal changes in corrosion rates. It can be seen that the corrosion rate values measured in saline solution are smaller at 1, 2, and 3 hours than in seawater, and the corrosion rates measured in 0.9 % saline are exaggerated, due to high porosity and corrosion caused surface errors. However, a corrosion rate maximum of 0.13 mm/year is generally acceptable for biocompatible materials. All of our values are lower, so the additively manufactured material is adequate for medical use.

Table 6. *Material composition of additively manufactured specimens*

Element	Weight %
Fe	62.33–63.91
Cr	20.38–22.15
Ni	10.49–12.81
Mo	1.66–2.74
Mn	1.09–2.37
Si	0.13–0.55

Table 7. *AM specimens' corrosion rates*

t (h)	v_{korr} (mm/yr)	
	0,9 % NaCl	3,5 % NaCl
0	0.00023	0.0035
1	0.00096	0.0056
2	0.00133	0.0061
3	0.00100	0.0050
4	0.01668	0.0059
5	0.01541	0.0057

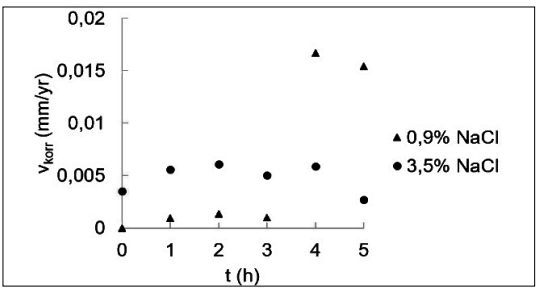

Figure 7. *Corrosion rate of AM specimens as a function of time*

4. Conclusions

4.1. Charpy impact test

To compare the specimens, which were produced by two different manufacturing processes the specific impact energy was ideal from the other result values of the impact test.

For the H2.5-marked specimens, the average specific impact energy was KCV = 1.493 J/mm^2, for the H10-marked specimens the average specific impact energy was KCV = 1.513 J/mm^2, in contrast the average specific impact energy for the A2.5 marked specimens was KCV = 0.96 J/mm^2. It can be seen that there is no significant difference between the same manufactured specimens, so the size reduction had no effect on these properties.

However, the difference between A-marked and H-marked specimens' specific impact energy is 0.543 J/mm^2, which was due to the porosity in the additively manufactured specimens.

All of the specimens were shown though their behaviour at room temperature.

4.2. Tensile test

Based on the tensile test it can be concluded that the short specimens are not suitable for determination of the mechanical properties, because with their geometry it is not possible to perform the test (insertion of extensometer was not possible), furthermore the notch in the center of the specimens is a stress concentrator.

The results of the long specimens indicate the tendency that the mechanical properties of the horizontally printed specimens are better than the vertically printed specimens. In the case of long test specimens, a difference is 60 MPa in yield strength, 27 GPa in elastic modulus and 46 MPa in tensile strength. In both cases this is in favour of the horizontally printed specimens. Comparing the measured results with the manufacturer's data [9] we can see that the Yield strength, tensile strength and elongation at break are higher in the manufacturer's data sheet than the value we have measured. This may be due to improper print settings that cause greater porosity in the material.

4.3. Corrosion test

The obtained corrosion rates were compared with the values found in the literature. The values obtained in physiological 0.9 % saline did not exceed the biocompatibility limit. The literature values were 0.0071 mm/yr [12], however we got 0.0053 mm/yr. This difference (0.0018 mm/yr) can be due to the characteristics of additive manufac-

turing technology, the surface roughness and the degree of porosity.

Acknowledgement

The project is funded by the National Research, Development and Innovation (NKFIH) Fund. Project title “Developing a new generation of customized medical aids for additive technologies”. The application ID number: NVKP-16-1-2016-022. The developers are grateful for the support.

The publication of the work reported herein has been supported by ETDB at BME. The authors gratefully acknowledgments the sponsorship.

References

[1] Redwood B., Schöffer F. , Garret B.: *The 3D Printing Handbook: Technologies, design and applications*. 1. kiadás. Coers & Roest, Amsterdam, 2017. 123–137. https://doi.org/10.1007/978-981-13-8281-9

[2] Keresztes Z., Pammer D., Károly D., Szabó J. P.: *EBSD examination of Ti-6Al-4V samples prodiced with additive technology*. IOP Conference Series: Materials Science and Engineering 426 012025 (2018) https://doi.org/10.1088/1757-899X/426/1/012025

[3] MSZ EN ISO/ASTM 52900:2017 *Additív gyártás. Általános alapelvek. Terminológia* (ISO/ASTM DIS 52900:2017)

[4] Zhang X.-Y., Fang G., Zhou J.: *Additively Manufactured Scaffolds for Bone Tissue Engineering and the Prediction of their Mechanical Behavior: A Review.* Material, 10/1. (2017) 50. https://doi.org/10.3390/ma10010050

[5] Gu D., Shen Y.: *Processing conditions and microstructural features of porous 316L stainless steel components by DMLS.* Applied Surface Science, 255 (5)/1. (2008) 1880–1887. https://doi.org/10.1016/j.apsusc.2008.06.118

[6] Chen S. Y., et al.: *Microsstructure and mechanical properties of open-cell porous TI-6AL-4V fabricated by selective laser melting.* Journal of Alloys and Compounds, 713. (2017) 248–254. https://doi.org/10.1016/j.jallcom.2017.04.190

[7] Mahmoudi M., et al.: *On the printability and transformation behavior of nickel-titanium shape memory alloy fabricated using laser powder-bed fusion additive manufacturing.* Journal of Manufacturing Processes, 35. (2018) 672–680. https://doi.org/10.1016/j.jmapro.2018.08.037

[8] MSZ EN ISO 148-1:2017 *Fémek. Charpy-féle ütővizsgálat*. 1. rész: Vizsgálati módszer (ISO 148-1:2016)

[9] *EOS Anyag adatlap, 316L.* (2019. 02.2 0.) www.eos.info/material-m

[10] MSZ EN ISO 6892-1:2016 *Fémek. Szakítóvizsgálat.* 1. rész: Vizsgálat szobahőmérsékleten (ISO 6892-1:2016)

[11] ASTM G102 - 89(2015): *Standard Practice for Calculation of Corrosion Rates and Related Information from Electrochemical Measurements*.

[12] Absora L., Ashour A. F., Mitchell S. C., Youseffi M.: *Corrosion of mild steel and 316L austenitic stainless steel with different surface roughness in sodium chloride saline solutions.* WIT Transactions on Engineering Sciences, Vol 65, ISSN 1743-3533. (2009) 168. https://doi.org/10.2495/ECOR090161

Acta Materialia Transylvanica 2/1. (2019) 61–68.
https://doi.org/10.33924/amt-2019-01-10
Hungarian: https://doi.org/10.33923/amt-2019-01-10,
https://eda.eme.ro/handle/10598/31420

The Role of Focus Position in Single Pulse Laser Drilling of Highly Reflecting Materials

György MESZLÉNYI,[1] Enikő BITAY [2]

[1] *Óbuda University, Budapest, Hungary, meszlenyi.gyorgy@kvk.uni-obuda.hu*

[2] *Sapientia Hungarian University of Transylvania, Faculty of Technical and Human Sciences Târgu Mureș, Department of Mechanical Engineering, Târgu Mureș, Romania, ebitay@ms.sapientia.ro*

Abstract

The laser processing of materials which are highly reflective at laser wavelengths is problematic. We have to take into account that only a small part of the energy is absorbed, the main part being reflected. In this article we examine the laser processing of highly reflective copper and silver at 1070 nm wavelength. In laser drilling of printed circuit boards it is necessary to drill copper layer as well. In highly reflecting materials we can drill smaller holes because of the low energy efficiency. Naturally in single pulse laser drilling the focus position plays a key role: at the focal spot of the laser beam smaller diameter holes are produced, further from the focal spot, higher diameter holes are produced.

Keywords*: laser drilling, focal position, highly reflecting materials.*

1. Introduction

From the literature of laser drilling we distinguish single pulse drilling, percussion drilling (using more than one pulse to produce a hole), trepan drilling for larger holes, and planetary drilling [1]. In this article we will examine single pulse drilling of copper and silver foils. In the laser drilling of printed circuit boards it is necessary to drill copper layers as well [2]. In this article we examine the laser drilling process of copper and silver foils.

2. Properties of the laser system

For the experiments we used an IPG 150/1500-QCW-AC fiber laser. Table 1. lists the properties of this single mode Ytterbium laser.

We would make a mistake, if we took into account into account only the average power of this laser system. If we calculate the pulse power by dividing the pulse energy with pulse length we can get higher values, for example: $P_p = E_p / t_p = 15$ J / 0,01s = 1500W. This means that this 150 W average power laser is more dangerous for the human eye than a continuous wave one with the same average power. In order to protect our eyes we have to wear protective goggles having an appropriate optical density at the laser wavelength; this optical density is defined by the standards.

3. Analysis of the focused beam parameters

In single pulse laser drilling the machining laser system plays a key role, most important are the parameters of the focused laser beam, such as focal spot diameter, and Rayleigh length. The focused laser beam is the tool for machining a work piece without touching it, using only the transfer of the laser's energy.

Table 1. *Technical data of IPG 150/1500-QCW-AC single mode Ytterbium fiber laser*

Wavelength l	1070 nm
Maximal average power	150 W
Maximal pulse power	1500 W
Maximal pulse energy	15 J
Pulse width	0.05–50 ms
Pulse frequency	10–50 kHz
M^2 factor	1.05

The diameter of the laser beam leaving the fiber is 14 microns (d_1); the focal length of the collimating lens is 50 mm (f_1). There is a lens focusing the parallel laser beam to the work piece, its focal length is 50 mm (f_2). The beam expander factor (B_e) setting is 1. On the basis of this given data we can calculate the spot size of the focused laser beam (d_2) with the following equation [3]:

$$d_2 = \frac{d_1 f_2}{f_1 B_e} \quad (1)$$

From this equation we obtain 14 microns for the focal spot diameter. Comparing it with an Nd:YAG laser's 81 micron focal spot diameter used for our former research [4] it is extremely small. This means that we can focus the laser energy in a small area producing a smaller cut slit, and we can cut thicker materials.

This difference is caused by the difference in the operation of these lasers influencing the beam quality factor. The Nd:YAG laser has a beam quality factor (M^2) of 3....5, the fiber laser has 1.05. Why is this data so important?

Analysing the other equation (2) of the focused laser beam spot size, we can see that the smaller the M^2 factor the smaller the diameter of the focused spot [5].

$$d_2 = \frac{d_1 f_2}{f_1 B_e} \quad (2)$$

The smaller is the diameter of the focused spot the higher the concentration of the laser energy. We can calculate the parallel laser beam diameter d_3 from this equation, it will be 5.11 mm. There is an important consequence of this laser wavelength (λ): if we use Ytterbium fiber laser (λ = 1.070 micron) instead of CO_2 laser (λ = 10.600 microns) we can focus the beam onto a 10 times smaller spot.

From this data we can calculate the Rayleigh length (Z_R) with equation (3). The Rayleigh length [6] is the distance from the focal spot, in the direction of the laser propagation, where the spot area will be increased by the a factor of two, and the beam radius will be increased by athe factor of√2.

In most cases we assume the laser beam to be in focus within the double of the Rayleigh length. The equation of the Rayleigh length is similar to the equation of the focused laser beam spot size, but in Rayleigh length equation f_2 and d_3 are toin the power of two. We can calculate the Rayleigh length from the above mentioned data, it will be 137 microns

$$Z_r = \frac{4\lambda M^2 f_2^2}{d_3^2 \pi} \quad (3)$$

Of course d_2 and Z_r are only approximations. For example in some articles M^2 is absent from these equations, which is strange. When the beam expander is a set of lenses with a zoom-system, this can make the focal spot larger so the focusing capability of the lenses are weaker.

The calculated d_2 and Z_r values indicate that it is better to leave the beam expander from the system, while the 14 microns focal spot from the unexpanded beam is small enough. If we expand the beam, the focal spot size will be smaller, but the value becomes also smaller. That means a bigger divergence of the beam, in other words, the beam, in a short distance towards laser propagation can easily be out of focus.

On the other hand the computed d_2 and Z_r values are only derived from geometric values. In truth the volume of the material we can melt with one pulse depends on many factors, the first factor being the power of the pulse concentrated on the focal spot, it can be maximum 1500 W.

The other factors are the relevant physical parameters of the material: density, melting point, specific heat coefficient, reflection on the wavelength of the laser. We will further discuss these factors ain chapter 4. According to the publication of Pulzor Művek company [7] operating this laser on stainless steel can be cut up to 1 mm thickness, and copper-alloys up to 0,4 mm. These thicknesses are two times larger than the computed Rayleigh-length.

The Ytterbium single mode fiber laser and the CNC work piece positioning system was mounted together, and programmed by Pulzor Művek, Hungary. This firm used his own CAM program generating CNC code form CAD data.

4. The properties of the processed materials

Why is it a great challenge to drill materials which are highly reflective at laser wave-lengths? Let's analyze a basic expression with the power entering the work piece: one part is reflected, the other is absorbed, and the third part is transmitted [8]:

$$P_1 = P_2 + P_3 + P_4 \quad (4)$$

Here P_1 is the whole power coming from the laser head, P_2 is the reflected, P_3 is the absorbed, and P_4 is the transmitted part. For bulk material

the transmitted part is negligible, so the higher part of the power is reflected, the lower part is absorbed by the material we want to process by laser light. If P_1=1, then P_3 is the absorption coefficient (a) of the material. P_2 is the reflective coefficient (r) for the given material and wavelength. Processing materials which are highly reflective at the laser wavelength, the major part of pulse energy is reflected, only a small part absorbed and used for melting the workpiece (see **Table 2.**).

We used 1.4304 stainless steel for our former research **[4]** We can predict from the data of **Table 2.** that the laser processing of silver and copper will be more difficult than the stainless steel. It will turn out that the extremely small focused spot size, and the high power density will help us to overcome this difficulty.

The high amount of reflected energy can cause harm to the laser **[11]**. During the research work the laser head was vertical, and the drilled material was stretched out at 8º angle from horizontal plane, so the incoming and reflected beam's angle was 16º preventing the reflected laser radiation returning to resonator.

4.1. The research work

We designed an instrument which stretches a metal foil at a given angle which can be set by a gauge block. This instrument fulfils the principle of a sinus mechanism. A 17.5 mm gauge block set comes to an 8.11° angle measured from horizontal plane. The research instrument mounted on the laser can be seen on **Figures 1.** and **2.**

The common experimental data were:
– relative focus set at laser head: –2.6 mm;
– process gas: nitrogen at 5 bar pressure.

5. Drilling performed on copper foil

We drilled 50 microns thin copper foil with different laser pulse energy. We set the pulse length 0, 2 ms constant value. We changed the output power between 60-80 %, this predicted the pulse power. We calculated the pulse energy by multiplying the pulse power by the pulse length. The laser pulse parameters can be seen in **Table 3.**

In **Figure 3.** the laser drilled set of holes can be seen under the stereo microscope with backlight illumination. The bottom of the picture was close to the laser head. The pulse grows from the right side to the left. The higher energy can make holes closer to the laser head. The holes on the top of **Figure 3.** get into each other, while the velocity was low, and the pulse frequency was constant.

Table 2. *Absorption coefficient (a), and reflection (r) of materials used for the former and this research*

Material	a	r
Stainless steel **[9]**	0.31	0.69
Silver **[10]**	0.03	0.97
Copper **[10]**	0.04	0.96

Table 3. *Laser pulse data of copper foil drilling, one row represents setting for a set of holes*

Pulse length (ms)	Pulse energy (mJ)	Pulse power (W)
0.2	198	989
0.2	213	1067
0.2	229	1145
0.2	245	1225
0.2	259	1296

Figure 1. *The research instrument mounted on the laser*

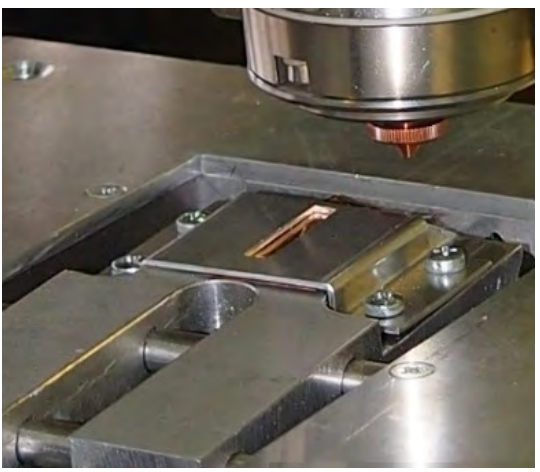

Figure 2. *Main parts of the foil strecher device*

The laser head was fixed, we set the workpiece positioning acceleration to 10 mm/s^2, and the maximal velocity to 20 mm/s. We had to measure the distance of the holes to calculate its vertical coordinate according to the focused laser beam propagation axis.

Figure 4. shows the interaction of the melting threshold energy (E_k) and the focused beam cross section. Far from the focal spot the laser beam intensity profile is low, the energy on a given area is not enough to melt the volume for drilling through the material, and it melts only the surface of the copper foil as can be seen on **Figure 5.** In **Figures 4.** and **8.** f. we can identify the same regions of drilled holes:

– Region 2: we can see holes with the diameter smaller than the maximal diameter, here only the top of the energy distribution of the beam cuts the melting threshold.
– Region 3: here are the holes with the maximal diameter.
– Region 4: we can see holes with the smallest diameter, because here is the focal spot of the beam, here is the maximal concentration of the energy.
– Region 5: here are the holes with the maximal diameter, as in region 3.

In **Figure 6.** we can see a microscopic picture of a hole close to the laser head. Here the nitrogen process gas was at the highest pressure, it dispersed the molten material around the hole. Because of this, in this region it is not easy to measure the diameter of the holes, the holes are like craters having conical surface with smaller diameter at the bottom.

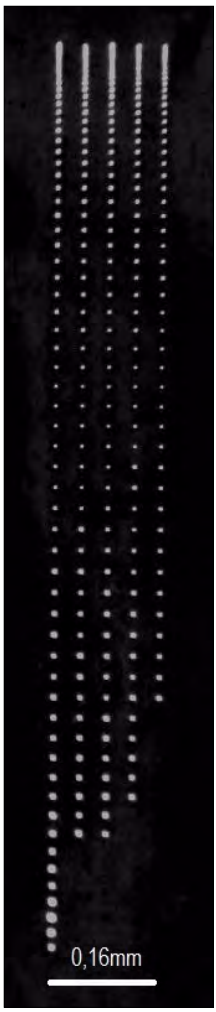

Figure 3. *Laser drilled holes on copper foil under the stereo microscope with backlight illumination*

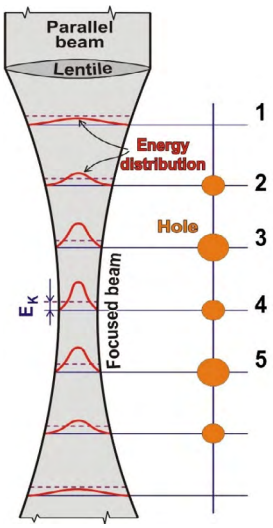

Figure 4. *Interactions of melting threshold energy and the focused beam* **[4]**

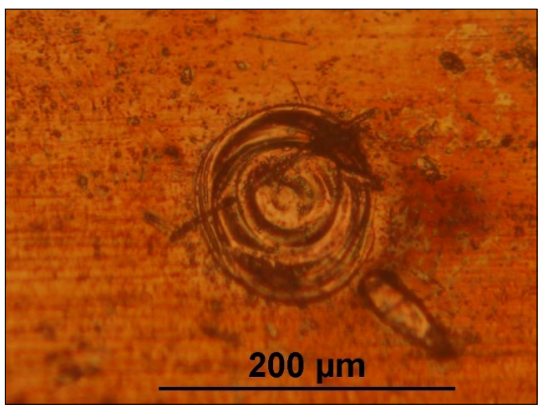

Figure 5. *Below the melting threshold energy there is no hole*

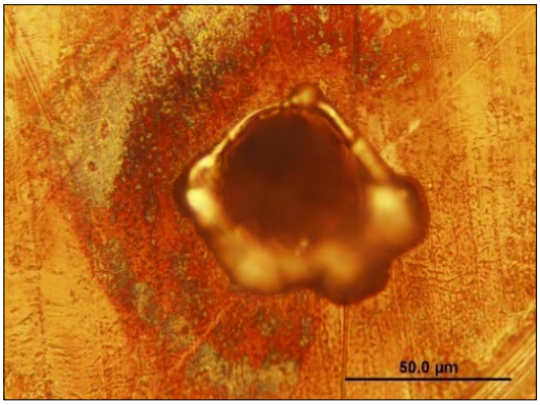

Figure 6. *Microscopic picture of a hole made in copper foil near to the laser head*

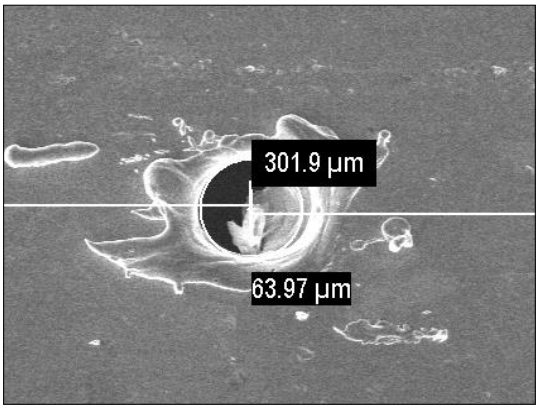

Figure 7. *Microscopic picture of a hole near to the laser head with dross adherence. The 301.9 microns are the distance from the neighbouring hole, the 63.97 microns are the three-point measured diameter of the hole*

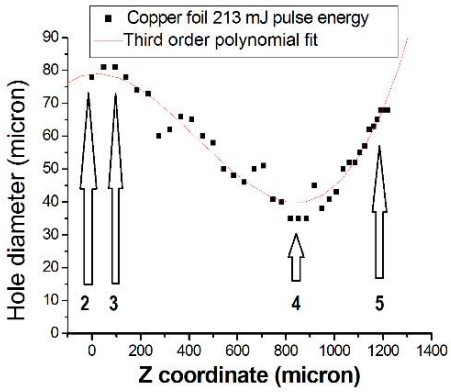

Figure 8. *Hole diameter – Z-coordinate function of copper foil made with 213 mJ pulses, and its regions; Z=0 coordinate is closest to the laser head*

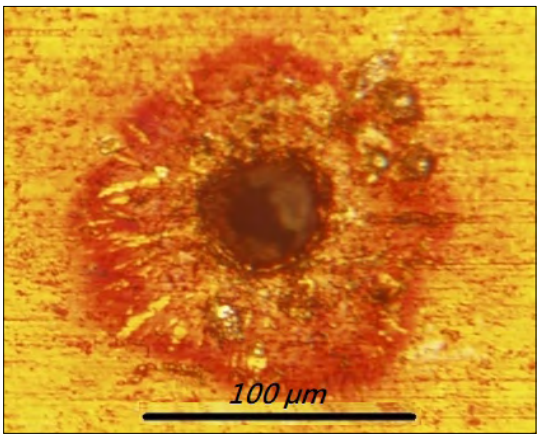

Figure 9. *Microscopic picture of a hole near to the laser head*

We can distinguish four zones in these holes:

1. The biggest zone is heat affected zone.
2. Second is the ring of molten material
3. Third is the diameter of the holes at the top, we measured this diameter
4. The smallest is the diameter at the bottom, because of the dross adherence (**Figure 7.**).

In **Figure 9.** we can see a microscopic picture of a hole far from the laser head. This hole has a better contrast, easier to measure, it has an ellipsis-like form. Around the hole there is a bigger heat affected zone: here the energy of the laser pulse is not enough to melt the volume for drilling through material because of the high reflection. The 5 hole diameter – Z-coordinate (distance towards laser propagation axis) functions were almost the same independent of the laser pulse data in **Table 3.** because the pulse energy change was only 25 %, and the deviation of the hole diameters was large (see the explanation of **Figure 6.**). One of these hole diameters – Z-coordinate function made with 213 mJ pulses can be seen on **Figure 8.**

6. Drilling performed on silver foil

We drilled 150 micron thin silver foil with different laser pulse lengths. We set the pulse length from 0, 1 ms to 0, 5 ms. We set the output power to 100 %, this predicted the pulse power, it was roughly 1600 W. The silver foil was three times the thickness of the copper, which required higher output power. We calculated the pulse energy by multiplying the pulse power by the pulse length. The laser pulse parameters can be seen in **Table 4.**

Table 4. *Laser pulse data of silver foil drilling, one row represents setting for a set of holes on Figure 10*

Pulse duration (ms)	Pulse energy (mJ)	Pulse power (W)
0,1	148	1481
0,2	317	1583
0,3	475	1584
0,4	636	1589
0,5	792	1583

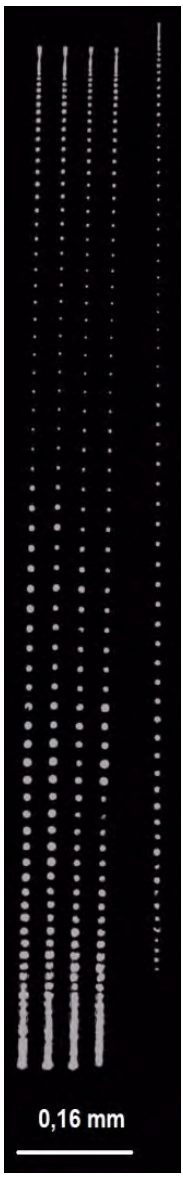

Figure 10. *Laser drilled holes on silver foil under the stereo microscope with backlight illumination*

In **Figure 10.** the laser drilled set of holes can be seen under the stereo microscope with backlight illumination.

The bottom of the picture was close to the laser head. The pulse energy grows from right side to the left. At the left side of the picture there are holes with 7 % less pulse power, because of this some holes are missing at the bottom of this set of holes. The other four set of holes are similar because the pulse power is constant.

The holes on the top and the bottom of **Figure 10.** Are continuous with each other, while the velocity was low, and the pulse frequency was constant. The workpiece positioning acceleration and the maximal velocity was the same as listed for the copper foil.

In **Figure 4.** and **11.** we can identify the same regions of drilled holes, but we can see only region 3. 4. and 5. because of the higher power level.

In **Figure 12.** we can see a microscopic picture of a hole close to the laser head. Here the nitrogen process dispersed the molten material around the hole, but this amount of the molten material was not as big as it was for the copper foil. (**Figure 6.**).

In **Figure 13.** we can see microscopic pictures of two holes far from the laser head. Around the holes there is a smaller heat affected zone than for the copper drilling.

Figure 11. shows hole diameter – Z-coordinate functions at 636 mJ pulse energy. The deviation of the hole diameters was large, because the solid-state laser's output pulse energy was fluctuating slightly. While they are operating in a nonstationery mode **[12]**.

Since the focal spot diameter was extremely small; the other source of the hole diameter's deviation can be plasma formation. The 5 hole diameter – Z-coordinate functions were almost the same independent of the laser pulse data in **Table 3.**

For single pulsed laser drilling not only the pulse energy counts, but also the pulse length in other words, the given energy at the period that is active. From these two factors we can calculate the pulse power $P_p = E_p / t_p$. The pulse power was constant for silver drilling. In laser machining literature the W/cm2 power density is the most important factor in deciding what kind laser machining can be performed.

We can conclude that the stronger factor on the drilled holes diameter is the Z coordinate.

The pulse energy fluctuations do have a significant effect on laser micro-machining, because the use of smaller laser pulses in higher pulse frequency compensate for the fluctuations.

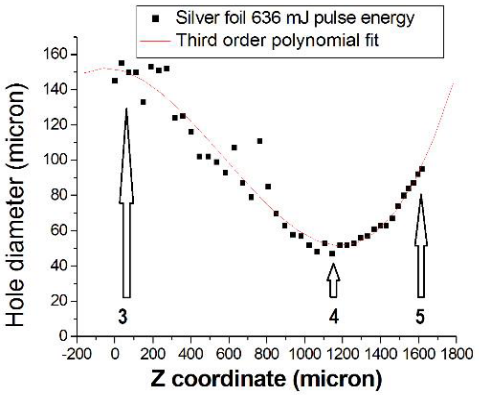

Figure 11. *Hole diameter – Z-coordinate function of silver foil made with 636 mJ pulses, and its regions; Z=0 coordinate is closest to the laser head*

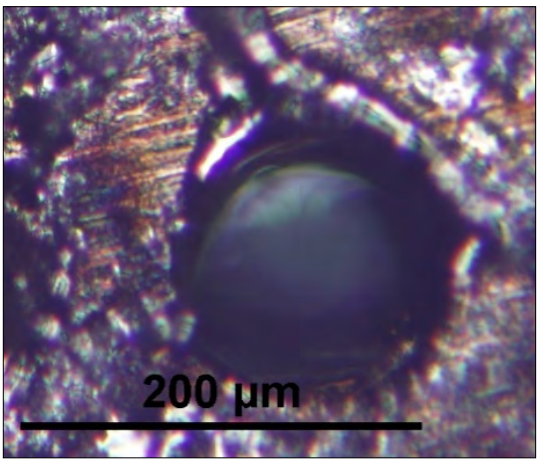

Figure 12. *Microscopic picture of a hole made in silver foil near to the laser head*

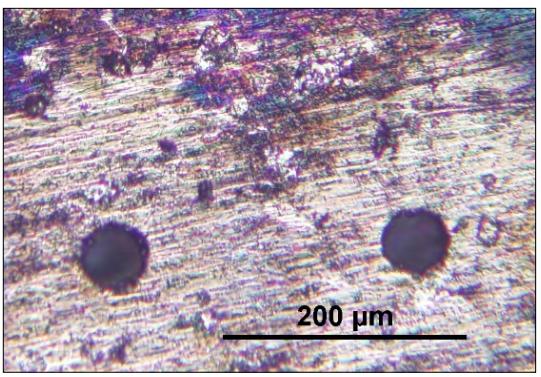

Figure 13. *Microscopic pictures of two holes in silver far from the laser head. Around the holes there is smaller heat affected zone than for the copper drilling*

7. Conclusions

In the laser processing of materials which are highly reflecting at laser wavelength we must take into account that only a small part of the energy is absorbed; the main part is reflected.

It turned out that the stronger effect on drilled hole diameter was the focal position. The hole diameter – Z-coordinate functions show fluctuations; the possible reasons are:

– nonlinear effects of plasma formation and evaporated material pressure,
– solid-state laser's output pulse energy is fluctuating slightly, because they are operating in a non-stationery mode,
– small irregularities of the surface on the material (50 microns) can cause 10 % change in the drilled hole diameter **[13]**

The 14 micron focal spot diameter is an extremely small value, we can concentrate the power of the laser pulse in a small area. This high power density compensates the losses caused by reflection of the material.

The good beam quality and the high pulse power of this fiber laser allows the laser drilling of highly reflective, otherwise challenging materials.

Acknowlwdgement

We kindly thank the support of Zsolt Puskás, director of Pulzor Művek, and the production engineer Dávid Vincze in the implementing of the experiments.

References

[1] Buza G.: *Lézersugaras technológiák II*. Edutus Főiskola, Budapest, 2012. 79.
[2] Kurosawa M.: *Laser drilling high-density printed circuit boards*. (accessed on: 2019. 05. 28.) https://www.industrial-lasers.com/drilling/article/16485325/laser-drilling-highdensity-printed-circuit-boards
[3] Xiaodong N.: *Laser Welding*. Published by Sciyo Janeza Trdine 9, 51000 Rijeka, Croatia, 2010. 54.
[4] Meszlényi Gy., Bitay E.: *Az egyimpulzusos lézersugaras fúrás folyamatának elemzése*. Bányászati és kohászati lapok, Kohászat, 151/5–6. (2018) 40–44.
[5] Paripás B., Szabó Sz., Kocsisné Baán M., Tolvaj Béláné, Bencs P.: *Lézeres mérési- és megmunkálási eljárások a gépészetben*. Miskolci Egyetem, Miskolc, 2009. 66.
[6] Alexander F. H. K.: T*heoretical analysis of laser beam cutting*. Shaker Verlag, Aachen, 2002. 14.
[7] Puskás Zs.: Lézeres mikromegmunkálás szállézerel. (accessed on: 2019. 04. 17.) http://docplayer.hu/720391-Lezeres-mikromegmunkalas-szallezerrel.html

[8] Kreisz I.: *Lézersugár-vezetés*. Edutus Főiskola, Budapest, 2011. 82.
[9] Duley W.: *Laser welding*, 1. edition. Wiley-Interscience, 1998. 69.
[10] Ready J. F., Farson D.: *LIA Handbook of Laser Materials Processing*. Laser Institute of America Magnolia Publishing Inc., 2001. 182.
[11] Naeem M.: *Laser processing of reflective materials*. (accessed: 2019. 05. 28.) https://onlinelibrary.wiley.com/doi/epdf/10.1002/latj.201390001
[12] Tradowsky K.: *A LASER ABC-je*. Műszaki Könyvkiadó, Budapest, 1971. 99–100.
[13] Stephen A.: *Laser micro drilling methods for perforation of aircraft suction surfaces*. Elsevier Science Direct Procedia CIRP 74, 2018. 404. https://doi.org/10.1016/j.procir.2018.08.157